

# Model predictive control of battery systems in a microgrid

---

Car, Mateja

Doctoral thesis / Disertacija

2023

*Degree Grantor / Ustanova koja je dodijelila akademski / stručni stupanj:* **University of Zagreb, Faculty of Electrical Engineering and Computing / Sveučilište u Zagrebu, Fakultet elektrotehnike i računarstva**

*Permanent link / Trajna poveznica:* <https://urn.nsk.hr/urn:nbn:hr:168:508141>

*Rights / Prava:* [In copyright](#) / [Zaštićeno autorskim pravom.](#)

*Download date / Datum preuzimanja:* **2024-05-13**



*Repository / Repozitorij:*

[FER Repository - University of Zagreb Faculty of Electrical Engineering and Computing repository](#)





University of Zagreb

FACULTY OF ELECTRICAL ENGINEERING AND COMPUTING

Mateja Car

# **MODEL PREDICTIVE CONTROL OF BATTERY SYSTEMS IN A MICROGRID**

DOCTORAL THESIS

Zagreb, 2023





University of Zagreb

FACULTY OF ELECTRICAL ENGINEERING AND COMPUTING

Mateja Car

# **MODEL PREDICTIVE CONTROL OF BATTERY SYSTEMS IN A MICROGRID**

DOCTORAL THESIS

Supervisor: Associate Professor Vinko Lešić, PhD

Zagreb, 2023







Sveučilište u Zagrebu  
FAKULTET ELEKTROTEHNIKE I RAČUNARSTVA

Mateja Car

# **MODELSKO PREDIKTIVNO UPRAVLJANJE BATERIJSKIM SUSTAVIMA U MIKROMREŽI**

DOKTORSKI RAD

Mentor: Izv. prof. dr. sc. Vinko Lešić

Zagreb, 2023.



Doctoral thesis is made at the University of Zagreb Faculty of Electrical Engineering and Computing, Department of Control and Computer Engineering

Mentor: Associate Professor Vinko Lešić, PhD

Doctoral thesis contains 119 pages

Thesis no.:



*Ovaj rad posvećujem svojoj obitelji.*



## ABOUT THE SUPERVISOR

---

**Vinko Lešić** received his PhD degree in 2014 from University of Zagreb Faculty of Electrical Engineering and Computing, Zagreb, Croatia (UNIZG-FER), under the supervision of Prof. Mario Vašak. Today, he is an Associate Professor within Laboratory for Renewable Energy Systems at the Department of Control and Computer Engineering of UNIZG-FER. His patented PhD research he shaped into the technology transfer project with a multinational aerospace R&D company. Since then, he has been leading 8 research and 4 technology transfer projects, and a spin-off company. He has participated as an associated researcher on over 20 projects, supervised 11 PhD students, and co-authored over 60 journal and conference papers and 5 patents. He is a member of Scientific and Professional Council of Innovation Centre Nikola Tesla. His research focus is on control algorithms, prediction and optimisation in renewable energy and sustainability topics, ranging from control of electrical machines and power electronics as part of his PhD, over optimal microgrid control and building energy management during his postdoctoral research, towards optimisation of various climate-driven processes such as city lighting, urban transport, supply chain and delivery logistics, and even agriculture, all with methods of machine learning, convex optimisation and combinatorial metaheuristics in modular and distributed topologies. He spent three months with Prof. Eduardo F. Camacho and has attended the winter and summer schools of Prof. Manfred Morari and Prof. Moritz Diehl. His research career was accompanied with highlighted community focus through organization of numerous programs and events such as creation of start-ups design thinking program “Imagine, Create, Innovate”, industry lecturers program “Technical Opportunities Week”, industry specialization course “AI bootcamp” and many STEM education and popularization activities. He is a distinguished volunteer in IEEE association, currently serving the role of Member Activities Vice-Chair of IEEE Region 8, a geographic area covering Europe, Middle East and Africa, where he is leading 13 teams of over 100 volunteers who tailor and supervise scientific, professional, educational and networking programs for 85,000 scientists and engineers. He is also the Vice Chair of IEEE Croatia Section and a member of KoREMA – Croatian Society for Communication,



Computing, Electronics, Measurement and Control. He has contributed to the creation of three national strategies in topics of alternative fuels, “green” jobs, and widespread digitalisation. He took part in forming the European Digital Infrastructure Consortium (EDIC) on AgriFood in Croatia.

## O MENTORU

---

**Vinko Lešić** je doktorirao 2014. godine na Fakultetu Elektrotehnike i računarstva, Sveučilišta u Zagrebu (UNIZG-FER) pod mentorstvom prof.dr.sc. Marija Vašaka. Izvanredni je profesor te član Laboratorija za sustave obnovljivih izvora energije (LARES) na UNIZG-FER. Svoje patentirano doktorsko istraživanje uobličio je u projekt prijenosa tehnologije s multinacionalnom tvrtkom za istraživanje i razvoj iz područja zrakoplovstva. Do sada je vodio 8 istraživačkih i 4 projekta transfera tehnologije, te spin-off tvrtku. Sudjelovao je kao suradnik na više od 20 projekata, bio mentor 11 doktoranada, te je koautor više od 60 konferencijskih i časopisnih radova te 5 patenata. Član je Znanstveno-stručnog vijeća Inovacijskog centra Nikola Tesla. Njegov istraživački fokus je na upravljačkim algoritmima, predviđanju i optimizaciji u temama obnovljivih izvora energije i održivosti, u rasponu od upravljanja električnim strojevima i energetsom elektronikom u sklopu njegovog doktorata, preko optimalnog upravljanja mikromrežama i upravljanja energijom zgrada tijekom njegovog poslijedoktorskog istraživanja, do optimizacije raznih klimatski vođenih procesa kao što su gradska rasvjeta, gradski prijevoz, opskrbeni lanac i logistika isporuke, pa čak i poljoprivrede, sve s metodama strojnog učenja, konveksne optimizacije i kombinatorne metaheuristike u modularnim i distribuiranim topologijama. Proveo je tri mjeseca kod prof. Eduarda F. Camacha te je pohađao zimske i ljetne škole prof. Manfreda Morarija i prof. Moritza Diehla. Njegova istraživačka karijera bila je popraćena naglašenim fokusom na zajednicu kroz organizaciju brojnih programa i događanja kao što su kreiranje start-up programa dizajnerskog razmišljanja “Imagine, Create, Innovate”, programa industrijskih predavača “Technical Opportunities Week”, tečaja industrijske specijalizacije “AI bootcamp” te mnogih STEM obrazovnih i popularizacijskih aktivnosti. Istaknuti je volonter u udruzi IEEE, te trenutno obnaša ulogu potpredsjednika za aktivnosti članova IEEE regije 8, geografskog područja koje pokriva Europu, Bliski istok i Afriku, gdje vodi 13 timova od preko 100 volontera koji kroje i nadziru znanstvene, stručne, obrazovne i programe umrežavanja za 85.000 znanstvenika i inženjera. Također je dopredsjednik Hrvatske sekcije IEEE i član KoREMA-e - Hrvatskog društva za komunikaciju, računarstvo, elektroniku, mjerenje i upravljanje. Pridonio je izradi triju

nacionalnih strategija u području alternativnih goriva, “zelenih” poslova i raširene digitalizacije. Sudjelovao je u formiranju European Digital Infrastructure Consortium (EDIC) on AgriFood u Hrvatskoj.

## ZAHVALA

---

Uspješna obrana teza u ovom doktorskom radu priznanje je svim ljudima koji su moj akademski put učinili vrijednim.

Na prvom mjestu želim zahvaliti svom mentoru Vinku Lešiću za stručnu i prijateljsku potporu u svojstvu neposrednog voditelja za vrijeme studentskih dana, a zatim i u svojstvu mentora na doktorskom studiju. Hvala mu na izdvojenom vremenu za jednadžbe i kodove, brojne diskusije, a najviše za strpljenje i razumijevanje kroz deset godina poznavanja (i zajedničkog rada).

Posebna zahvala i profesoru Mariju Vašku, mom prvom mentoru, za svaku minutu koju ste izdvojili za raspirivanje jednadžbi i dodatna objašnjenja. Hvala Vam na strpljenju, na savjetima i pomoći od početka studija na FER-u do zadnjih dana rada na disertaciji.

Nadalje, izražavam svoju iskrenu zahvalnost svima koji su me pratili na ovom izazovnom ali ispunjavajućem putu. Zahvaljujem akademskom osoblju koje mi je pružilo ogromnu pomoć i stručno vodstvo.

Uspješni završetak ovog dokorskog rada ne bi bio moguć bez beskrajne pomoći i podrške mojih kolega i prijatelja.

Hvala Aniti i Hrvoju, na svim stručnim savjetima i prijateljskoj potpori. Hvala vam što ste me saslušali kada bih negdje zapela i uvijek pronašli neku riječ ili gestu da me oraspoložite. Hvala i ostatku mog "13-og kata" – Danku, Dorijanu i Filipu – za pozitivan stav i bodrenje do zadnjeg dana pisanja disertacije. Zahvaljujem i ostalim kolegama iz LARES-a te zavodskim kolegama za pomoć i razumijevanje.

Hvala mojim prijateljima, Mirni i Ivanu, Ameliji i Vedranu, Pauli, Tajani, Ani, Kristini i Antoniji što su me bodrili i nasmijavali i olakšali mi ovaj proces.

Hvala mojoj obitelji i brojnoj rodbini; Carima, Rađenovićima i Topalovićima za ljubav i podršku od najranijih dana. Posebno hvala teti Zdenki i tečetu Janku, što ste vjerovali u mene i uljepšali mi brojne dane tijekom ljetnih praznika. Mnoge stranice ovog rada nastale su pod vašim krovom.

I na kraju, najveća hvala mami Mileni, tati Ivanu i bratu Mariju, za bezuvjetnu ljubav i pažnju, za podršku u trenucima tuge i radosti. Hvala što ste me hrabрили, poticali,

punili samopouzdanjem i pomagali da ustrajem na ovom putovanju. Odradili smo ovo kao pobjednički tim.

### **Model predictive control of battery systems in a microgrid**

The research is focused on the control of heterogeneous battery storage systems by taking into account the chemical processes inside a battery which are reflected in variable battery efficiency and consequently, battery longevity. This is motivated by economic benefits that stem from more efficient control of microgrid components in microgrid optimal power flow problems. The control objective is formulated as a model predictive control problem and the control structure is decomposed into two levels. The higher level is in charge of microgrid optimal power flows and is based on a high level of abstraction model of storage system. The lower level is based on a detailed storage system model and is in charge of delivering the demanded power profiles in the most efficient way. The battery converter model includes power-dependent efficiency in the form of look-up-tables and the internal resistor of the battery model is a function of battery states. The parameters are obtained by model-based identification techniques.

**Keywords:** battery storage system, microgrid, two level control problem, optimal power flow, efficient battery charging and discharging, microgrid components, grid converter control, variable efficiency models, parameter identification, model predictive control



## **Modelsko prediktivno upravljanje baterijskim sustavima u mikromreži**

U današnje vrijeme, mnogo se pažnje pridaje mikromrežama. Integracija obnovljivih izvora energije, koja se u zadnjem desetljeću potiče kroz različite energetske i ekološke politike, olakšana je uključivanjem spremnika energije u mikromreže. Time se omogućava vremenski pomak između proizvodnje i potrošnje električne energije što doprinosi energetske i cjenovnoj efikasnosti. Ideja mikromreže također omogućava napajanje lokalnih tereta, čime se smanjuju gubitci energije u prijenosu, te povećava pouzdanost i stabilnost (otočni rad tijekom poremećaja u glavnoj mreži). Ravnoteža između proizvodnje i potrošnje u svakom vremenskom trenutku omogućena je proračunom optimalnih tokova snaga uz minimalne operativne troškove. Zbog ekološke i ekonomske koristi mikromreža, odnosno optimalnih tokova snaga u mikromrežama, javlja se potreba za razvojem različitih optimizacijskih algoritama i efikasnim upravljanjem komponentama mikromreže.

Uzimajući u obzir cijenu i vijek trajanja, baterije se trenutno smatraju najprikladnijim sustavom skladištenja energije u mikromrežama iz tehno-ekonomske perspektive. Matematički modeli baterija preduvjet su za napredne upravljačke algoritme kojima se postiže visoka efikasnost sustava. Jednostavnim modelima ne može se precizno obuhvatiti dinamika baterije, a precizni modeli su računalno zahtjevni što ograničava primjenu istih u upravljanju u stvarnom vremenu.

Najjednostavniji model promatra samo energiju razmijenjenu između mikromreže i spremnika energije. Ovaj pristup zanemaruje unutarnje procese baterije te rezultira sub-optimalnim ponašanjem sustava koji upravlja baterijama (engl. battery management systems, BMS). Detaljniji modeli dijele se u dvije kategorije: elektrokemijski i električni modeli. Elektrokemijski modeli pomoću parcijalnih diferencijalnih jednadžbi opisuju elektrokemijske reakcije u baterijama tijekom punjenja/pražnjenja. Iako su to najprecizniji modeli, njihova kompleksnost uzrokuje visoke računalne troškove. Električni modeli (engl. electrical circuit models, ECMs) sastoje se od nadomjesnih naponskih/strujnih izvora, otpornika, kondenzatora i zavojnica kako bi se opisalo ponašanje baterije.



Najčešće korišteni ECM je Theveninov model. Osnovni Theveninov model sastoji se od konstantnog napona otvorenog kruga te serijskog otpornika. Serijski otpornik predstavlja unutarnji otpor elektrolita propagaciji iona. Prijelazni odziv napona na stezaljkama baterije modelira se dodavanjem paralelnih RC krugova osnovnom krugu. Iako model postaje precizniji dodavanjem većeg broja RC krugova sa različitim vremenskim konstantama, za većinu primjena, dovoljna su dva RC kruga. Nedostatak Theveninovog modela je što se ne može odrediti vrijeme trajanja baterije.

Hibridni model je još jedna popularna vrsta ECM-a. Hibridnim modelom modelira se i vrijeme trajanja baterije i naponski odzivi. Model se smatra vrlo preciznim, a istovremeno jednostavnijim u usporedbi s elektrokemijskim modelima. Sastoji se od dva kruga. Prvi se krug sastoji od kondenzatora, koji predstavlja naboj baterije, i strujno-upravljanog strujnog izvora te se njime modelira baterijsko stanje napunjenosti (engl. state of charge, SOC). Drugi je krug sličan Theveninovom modelu. Najčešće se sastoji od serijskog otpornika i dva RC kruga koji modeliraju prijelazni odziv napona baterije. Naponski izvor nije konstantan, već ovisan o SOC-u, a budući da se radi o nelinearnoj ovisnosti, model postaje nelinearan.

Jedan od obećavajućih modela, iz perspektive jednostavnosti i povećane preciznosti, je model s dva kondenzatora tzv. double-capacitor model (DCM). Sastoji se od dva kondenzatora različitih kapaciteta, čime se imitira dinamika površine elektrode (koja se puni brže) i unutrašnjosti elektrode (koja se puni sporije). Ovim modelom oponaša se efekt oporavka napona (engl. charge recovery effect). Kako bi se postigao precizniji prijelazni odziv napona baterije može se dodati RC krug kao i kod Theveninovog modela.

Nakon odabira prigodnog modela, potrebno je identificirati parametre modela baterije. Identifikacija se najčešće provodi korištenjem velike količine eksperimentalno dobivenih podataka te izvođenjem zaključaka ili na temelju nekog prethodnog empirijskog znanja ili temeljeno fizikalnim pretpostavkama o sustavu. Metode temeljene na mjerenim podacima dijelimo na aproksimacijske metode i metode estimacije pomoću Kalmanovog filtra. Aproksimacijski problemi većinom se rješavaju pomoću različitih metoda najmanjih kvadrata (engl. least-square, LS), poput LS sa regijama povjerenja ili rekurzivni LS, genetskih algoritama, neuronskih mreža i metoda potpornih vektora. Različiti Kalmanovi filtri (KF) koriste se za online identifikaciju, uključujući prošireni KF i različite tipove KF sa sigma točkama.

Metode upravljanja postupkom punjenja baterija također možemo podijeliti u skupine ovisno o tome temelje li se na modelu baterije ili ne. Profili punjenja, metoda kod kojih se ne koriste modeli baterija, unaprijed su definirani koristeći heuristiku i empiričko znanje. Ovakav način upravljanja jednostavan je za implementaciju, međutim ne uzima u obzir unutarnje procese u baterijama. U takve metode ubrajamo: punjenje konstantnom strujom (CC), punjenje konstantnim naponom (CV) i pulsno punjenje. Metode temeljene na modelima uključuju različite elektrokemijske i električne modele, te estimatore stanja. U takve metode ubrajamo neizrazito upravljanje, više-kriterijsko upravljanje, linearno

kvadratno upravljanje i modelsko prediktivno upravljanje (MPC). MPC je najpopularniji pristup, međutim primijenjuje se većinski na linearnim sustavima. Navedeni pristupi su većinom usmjereni na očuvanje integriteta (SOH) baterije. Modeli baterija na kojima se temelje upravljački algoritmi često su pojednostavljeni i linearizirani.

Baterije su, kao dio sustava skladištenja energije, često dio optimizacije tokova snaga s ciljem minimizacije troškova rada u mikromrežama. Strategije usmjerene na optimizaciju uključuju dinamičko programiranje, genetske algoritme, neuronske mreže te modelsko prediktivno upravljanje. Kod definicije optimizacijskog problema na razini mikromreže, mogu se primijeniti različiti ciljevi poput: i) uključivanja u tržište "dan unaprijed" ili u "stvarnom vremenu", s ciljem minimizacije troškova rada, ii) korištenje spremnika energije za rezanje vrhova potrošnje (engl. peak-shaving), iii) degradacija baterije.

Međutim, mnogi pristupi koriste jednostavne "modele energija" ili pojednostavljene i linearizirane Theveninov model sa konstantnim efikasnostima. U ovoj disertaciji, istraživanje se fokusira na upravljanje heterogenim baterijskim sustavima za pohranu, uzimajući u obzir kemijske procese unutar baterija koji se odražavaju u obliku promjenive učinkovitosti, a posljedično i dugotrajnosti sustava. Istraživanje je motivirano ekonomskom korišću koja proizlazi iz efikasnijeg upravljanja mikromrežnim komponentama prilikom rješavanja problema optimalnih tokova snaga u mikromreži. Upravljački problem rastavljen je na dvije razine. Viša razina upravlja tokovima snaga u mikromreži, a temelji se na pojednostavljenom modelu baterijskog sustava. Niža razina temelji se na detaljnom modelu, a zadužena je za ostvarivanje traženih profila snaga na najefikasniji način. Model baterijskog pretvarača uključuje promjenjivu efikasnost ovisnu o snazi, a unutarnji otpor modela baterije funkcija je trenutnog stanja baterije. Vrijednosti parametara dobivaju se metodama identifikacije temeljenim na metodama najmanjih kvadrata.

Doktorska disertacija podijeljena je u 6 poglavlja. Uvodno, *Poglavlje 1*, donosi pregled trenutnog stanja te motivaciju za provedeno istraživanje.

*Poglavlje 2* opisuje različite vrste baterija i osnovne pojmove vezane uz baterijske sustave pohrane energije. Budući da se rezultati disertacije temelje na litij-ionskim baterijama, iste su detaljnije opisane u poglavlju.

*Poglavlje 3* opisuje identifikaciju parametara ovisnih o stanju napunjenosti litij-ionske ćelije. Odabran je Theveninov nadomjesni model kao temelj identifikacije, a identifikacija se temelji na metodi najmanjih kvadrata. Uspoređeni su rezultati identifikacije za tri modela različite složenosti: i) model s unutarnjim otporom (R0 model), ii) model s jednim paralelnim RC krugom (1RC model), te iii) model s dva RC kruga (2RC model). Na temelju rezultata, 2RC model je odabran za izradu modela efikasnosti. Na kraju poglavlja, definiran je model efikasnosti baterije ovisan o stanju napunjenosti te struji punjenja/pražnjenja.

*Poglavlje 4* fokusirano je na upravljanje strujom punjenja/pražnjenja baterijskog sustava pohrane, temeljeno na prethodno razvijenom nelinearnom modelu. Baterijski sustav pohrane obuhvaća bateriju te pripadajući energetski pretvarač. Opisane su

tipične konfiguracije baterijskih pretvarača i učestale upravljačke strukture. Algoritam upravljanja koristi nelinearno modelno prediktivno upravljanje za izračun sekvence struja punjenja ili pražnjenja, koja će rezultirati razmjenom energije između baterije i ostatka mikromreže u traženom iznosu. Algoritam proširuje prethodni postupak primijenjen na olovne baterije s konstantnim parametrima, korištenjem varijabilnog modela. Dobiveni algoritam, temeljen na varijabilnom modelu, rezultira efikasnijim radom u vidu višeg rezidualnog stanja napunjenosti te nižim amplitudama punjenja/pražnjenja koje pozitivno utječu na životni vijek baterijskog sustava.

*Poglavlje 5* daje pregled rada različitih komponenti mikromreže. Razumijevanje pojedinačnih algoritama svake komponente mikromreže bitno je zbog koordinacije svih komponenata te implementacije optimalnih tokova snaga, proračunatih optimizacijskim problemom. Ovisno o vrsti komponente i tipu mikromreže, različiti DC/DC i/ili DC/AC pretvarači koriste se pri povezivanju jedinica na zajedničku sabirnicu te zatim na glavnu energetska mrežu. Pretvarači snage predstavljaju kontrolne točke sustava koje osiguravaju stabilnost i kvalitetnu opskrbu energijom, budući da se željeni tokovi snaga, proračunati nekim optimizacijskim algoritmom, postižu upravljanjem strujama/naponima pretvarača. Upravljive komponente mikromreže obuhvaćaju obnovljive izvore (fotonaponske panele i vjetroturbine) te pripadajuće pretvarače. Mrežni pretvarač zadužen je za održavanje napona DC sabirnice. U upravljačkom krugu DC napona invertera primijećeni su problemi s nestabilnošću uzrokovani parametarskom nesigurnošću te odstupanjem od radne točke. Prikazan je sistematični pristup pri sintetiziranju upravljačkog algoritma DC napona, gdje su u obzir uzete i promjenjivost mrežne impedancije i nelinearnosti DC kruga. Mrežna impedancija uzeta je u obzir dodavanjem dodatnog seta strujnih senzora na mjesto spajanja s mrežom. Upravljački algoritam sintetiziran je korištenjem modelskog pristupa - Truxal-Guillemine, uzimajući na taj način u obzir i nelinearnosti i nestabilnosti. Provedena je i analiza stabilnosti i robusnosti na promjene parametara te se model pokazao stabilnim. Model je također uspoređen s konvencionalnim metodama upravljanja koje mogu izazvati nestabilnost prilikom većeg udaljavanja od radne točke. Dobiveni regulator je eksperimentalno verificiran. U ovom poglavlju, definiran je i nelinearni problem optimalnih tokova snaga u mikromreži temeljen na MPC-u. Upravljački algoritam koristi pojednostavljeni, energetski, model baterijskog sustava pohrane te proračunava optimalnu razmjenu energije baterijskog sustava i mikromreže. Implementiran je model baterijskog sustava pohrane s promjenjivom efikasnošću. Prediktivni algoritam nastoji slijediti točku maksimalne efikasnosti s ciljem minimiziranja troška razmjene energije. Provedene su provjere algoritma za jednodnevno i sedmodnevno vrijeme rada, koje rezultiraju dodatnim uštedama u odnosu na konvencionalno upravljanje. Nadalje, dobiveni algoritam je proširen na heterogeni sustav pohrane, pri čemu je svaki sustav definiran svojim promjenjivim modelom.

Disertacija završava zaključkom u *Poglavlju 6*, gdje je dan osvrt na rezultate te su predložene daljne mogućnosti predložene metodologije.

Istaknut je sljedeći znanstveni doprinos disertacije:

- Metoda identifikacije modela litij-ionskih baterijskih sustava pohrana s promjenjivom učinkovitosti pretvarača i baterije, pogodna za primjenu u modelskom prediktivnom upravljanju
- Modelsko prediktivno upravljanje strujom punjenja i pražnjenja baterije uzimajući u obzir identificirani nelinearni matematički model baterijskog sustava pohrane s ciljem postizanja njegove maksimalne učinkovitosti
- Modelsko prediktivno upravljanje mikromrežom koja sadrži heterogene baterijske sustave pohrane s ciljem njenog cjenovno optimalnog rada

**Ključne riječi:** baterijski spremnici nenerije, mikromreža, upravljački problem na dvije razine, optimalni tokovi snaga, efikasno punjenje i pražnjenje baterija, komponente mikromreže, upravljanje mrežnim pretvaračem, modeli s promjenjivom efikasnošću, identifikacija parametara, modelsko prediktivno upravljanje



# CONTENTS

---

<b>1</b>	<b>Introduction</b>	<b>1</b>
<b>2</b>	<b>Electrochemical batteries and equivalent models</b>	<b>5</b>
2.1	Lithium-ion battery chemistry and characteristics. . . . .	7
2.1.1	Li-ion battery parameters. . . . .	8
2.2	Battery equivalent models. . . . .	10
2.2.1	Equivalent circuit models. . . . .	11
<b>3</b>	<b>Identification of a nonlinear battery model</b>	<b>15</b>
3.1	Battery model parameter identification methods. . . . .	15
3.2	Battery model identification procedure using Linear least-squares (LLS) method. . . . .	16
3.3	Constrained combined least-square parameter identification. . . . .	26
3.3.1	Constrained least-square parameter identification with a known OCV curve. . . . .	30
3.4	Variable battery efficiency model. . . . .	35
3.4.1	Efficiency of the second order ECM. . . . .	37
<b>4</b>	<b>Model predictive control of battery charging and discharging current</b>	<b>41</b>
4.1	Storage system converter model and efficiency. . . . .	42
4.2	Battery charging and discharging approaches. . . . .	45
4.3	Variable battery storage system model control. . . . .	46
4.3.1	Open-loop simulation of a variable BSS control. . . . .	51
<b>5</b>	<b>Model predictive control of a microgrid with heterogeneous battery storage systems</b>	<b>55</b>
5.1	Photovoltaics and wind turbine control. . . . .	55
5.1.1	Wind turbine model. . . . .	57
5.1.2	Wind turbine generator converter model. . . . .	58

5.2	Photovoltaic array. . . . .	.59
5.3	Grid converter control. . . . .	.60
5.4	Current control. . . . .	.62
5.4.1	Converter current control. . . . .	.63
5.4.2	Grid current control. . . . .	.64
5.5	Voltage control loop. . . . .	.68
5.6	Robustness analysis. . . . .	.71
5.7	Experimental results. . . . .	.76
5.8	Control of a battery system with variable efficiency. . . . .	.81
5.8.1	Linearization. . . . .	.82
5.8.2	Problem formulation. . . . .	.85
5.8.3	Simulation results. . . . .	.87
5.9	MPC of a microgrid with $n$ battery storage systems. . . . .	.93

## **6 Conclusion101**

## **Bibliography103**

## **Curriculum Vitae115**

## **List of publications117**

## **Životopis119**

---

# Introduction

Nowadays, a lot of attention is given to the concept of microgrids. One of the main advantages of microgrids is enhanced renewables integration. By introducing energy storages, time shifts between production and consumption towards energy and cost efficiency, are enabled. Other advantages of microgrids include decreased transmission losses by powering local loads and increased reliability and stability (islanded mode during disturbances in the main grid). The operating levels of different microgrid components are often determined as part of the optimal power flow problem. The objective is to preserve the balance between power production and consumption, while minimizing operating costs. Because of overall economic and environmental benefits of microgrids and optimal power flow, the need for development of different optimization strategies and efficient control of microgrid components is recognized [1], [2].

Considering price and service life, battery storages are currently the most suitable system for the microgrids from the techno-economical perspective. Mathematical models of batteries are pre-requisite for advanced model-based control algorithms that achieve high efficiency of the system. While simple models fail to capture battery dynamics accurately, and accurate models are computationally too complex which limits their application in real-time control. For identification of model parameters, data-based models are validated. These methods include extensive experiments and the parameters are extracted from measurement results. The most commonly used methods are data fitting and Kalman filters (KF). Data fitting problems are solved using different least-squares (LS) methods, such as trust region nonlinear LS or recursive LS [3], genetic algorithms, neural networks and support vector machines [4]. A variety of KF solutions are presented in the literature including extended KF and different types of sigma-point KF [5]. Although most authors, for simplicity reasons, consider parameters constant, in the proposed research parameters related to the current battery state are considered. This is similar to the approaches described in [6] and [3] where LS problem formulations with state of charge (SOC) dependent internal resistance are introduced.

Microgrid optimal power flow problems (OPF) aiming to minimize the operational



costs mostly include and utilize batteries, as storage systems [7]. Optimization-based strategies include dynamic programming, genetic algorithms, neural networks, and model predictive control [8]. Different optimization goals for microgrid operation are described in literature such as: i) participating in day-ahead and real-time markets (energy trading) to minimize operating costs [9], [10], ii) addressing renewable energy sources uncertainty [11] using a mixed-integer problem formulation, and iii) energy storage scheduling for peak-shaving applications [12], [13]. In [13] and [14], battery degradation is added to the cost function. Many approaches use simple battery energy models or simplified or linearized Thevenin models with constant efficiencies. In [14] both the converter and the battery variable efficiencies are mentioned. For problem formulation, the converter efficiency is averaged, and the battery efficiency is approximated with two affine functions over the whole operating range. The battery storage system model considered in the thesis includes both the battery and converter energy losses models. Converter losses are modelled using efficiency curves, variable against charging and discharging energies. The battery model is based on variable parameters which affect battery efficiency depending on its (SOC) and the applied charging/discharging current.

The second objective of the thesis is to develop model predictive control (MPC) for battery storage system charging/discharging based on a battery with variable efficiency over the prediction horizon. To validate the approach its performance is compared with the already established MPC with a constant-efficiency model. The MPC approach is utilized because of its ability to efficiently handle constrained problems and suitability for real-time applications. Through the performed analysis it is showed that the variable-efficiency model with the corresponding MPC algorithm achieved additional energy savings and increased cost efficiency of the battery and microgrid systems and expanded the lifespan of the battery storage system components.

The thesis is organized in 6 chapters as follows:

- Chapter 2 describes battery fundamental terms and gives an overview of battery equivalent models.
- In Chapter 3, identification methods for a variable parameter battery model are described. The methods are compared and the best model is further used for battery charging and discharging control. Based on this model, battery efficiency curves are obtained and used in microgrid power flow optimization problems.
- Battery charging and discharging control algorithm based on MPC formulation is presented in Chapter 4. An existing control algorithm for adherence to energy exchange commands is supplemented with the variable battery model obtained in Chapter 3 in order to remove model errors and increase the accuracy and efficiency of the charging/discharging processes.
- An overview of microgrid components and their optimal control strategies is given in Chapter 5. After describing each component, a microgrid power flow optimization

problem is formulated. Several simulation scenarios are described. The optimization problem contains variable battery system efficiency over the prediction horizon and a sequential-linear-programming (SLP) based microgrid control algorithm is developed. The developed algorithm is also verified by including heterogeneous storage systems.

- The thesis is concluded in Chapter 6 by an overview of the results and with final remarks.



---

# Electrochemical batteries and equivalent models

Energy storages have an important role in modern power systems. Some applications include energy management, ancillary services, and integration of renewables. The storage systems are classified into mechanical, electrical, and electrochemical. The oldest types are mechanical storages. Pumped hydro and compressed air storages are suitable for large scale applications because of their large capacity, low operational costs, and long lifetimes. However, they are limited to appropriate geographic locations. Flywheels are advantageous in ancillary services because of their quick response times. They have long life and operational costs. On the other side, it has high self-discharge and low energy density. Electrical storage systems include super-capacitors and superconducting energy storages, which store energy in electrical or electromagnetic form. As no additional energy transformations are needed, they are characterized with high efficiency. Electric storages have short response times and high-power density, however they also have high self-discharge. Electrochemical storages include different types of batteries offering modularity [15,16].

Batteries are energy storages that convert chemical energy into electrical and vice-versa. They consist of one or more electrochemical cells (connected in series or in parallel) with external connections. Each cell consists of two electrodes and an electrolyte which serves as a buffer for internal ion flow between the electrodes (lithium-ion, nickel-cadmium) or is an active participant in electrochemical reactions as for example in lead-acid batteries.

Batteries are divided into two categories: primary and secondary batteries. Primary cells are used until all the chemicals that generate power are depleted and then are discarded. Secondary batteries are rechargeable and are therefore suitable for a variety of applications including electric vehicles (EVs) and battery storage systems. Specific power (loading capability, [W/kg]) is the ability to deliver high current. Energy density (specific energy) is the amount of energy stored in a given system per unit volume. The higher energy density, the more energy may be stored for the same amount of volume. Depending

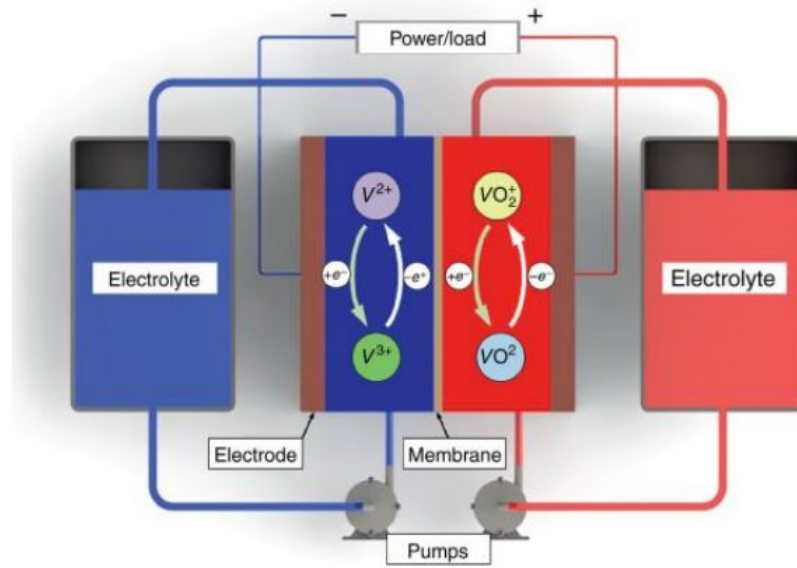


**Figure 2.1.** Vanadium flow battery [17].

on the materials used for electrodes and electrolyte there are different battery types: lead-acid, nickel-cadmium, lithium-ion, sodium-ion, redox-flow etc. Lead-acid and nickel-cadmium batteries are used since the 19th century and are well researched technologies which contributes to their low costs. Lead-acid batteries have a high cell voltage and have a good power density, however they have limited energy density and short lifetimes. Nickel-cadmium batteries can be charged with high current rates and have a long lifetime. Their disadvantages are the memory effect which causes loss of capacity if it is not fully discharged periodically and the construction with toxic materials. Flow batteries are unconventional electrochemical batteries. They consist of two external tanks filled with electrolytes that contain redox pairs as shown in Fig.2.1. The electrolytes are pumped to a compartment with electrodes where oxidation and reduction occur. The power depends on the number and size of the cells and the energy depends on the tank size. Its advantages are operating safety, long lifetime and deep discharging capability. Its disadvantage is low energy density [17].

A promising new battery technology is the sodium-ion battery which was originally developed in 1970s. However, the interest for this technology declined due to lithium-ion technology which was being developed at the same time. In the last decade its popularity increased because it operates similar to lithium-ion batteries, replacing the costly lithium with sodium. This technology is environmentally friendly, has a long lifetime, and can operate in cold temperatures but has lower cell voltages and energy density, compared to lithium-ion batteries [15,18].

Lithium-ion batteries are currently mostly used types in electronics, transportation and power grid applications due to their high charge density, long lifetime and high cell voltages. On the other hand, their disadvantages are high costs and sensitivity to high

temperatures and consequently the need for protective circuits [19].

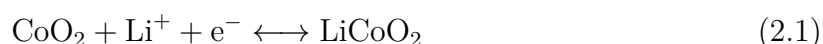
The comparison of the different types of storages, their advantages, and disadvantages, show the dominance of the pumped hydro storages (PHS) and the lithium-ion batteries. PHS is the oldest and more mature technology and the best solution for large energy storage applications storing over 95% of energy storage capacity worldwide, however the battery storages technologies are developing rapidly. Battery storages, specifically lithium-ion batteries, are mostly used in ancillary services. However, their utilization in energy management applications is growing nowadays. This is the result of the decreasing costs because of the availability of materials and their improving characteristics [16].

The thesis research is focused on lithium-ion batteries, therefore its characteristics are described in more detail in subsequent sections.

## 2.1 Lithium-ion battery chemistry and characteristics

Lithium-ion batteries (Li-ion) are lightweight, have high energy density, high efficiency, rather long life cycle and low self-discharge, compared to other battery types. The negative electrode is made of carbon (often graphite) and the positive electrode is made of a metal oxide, such as cobalt oxide (LCO), iron phosphate (LFP) or manganese oxide (LMO). The electrolyte is non-aqueous because lithium is highly reactive with water. The electrolyte should have high ionic conductivity, allowing the ions to flow and be resistant to the flow of electrons. Lithium has the tendency to give up the outer electron. The migration of ions in the Li-ion battery is depicted in Fig.2.2. During discharge, at the anode, oxidation reaction produces positively charged lithium ions and negatively charged electrons. The lithium ions are transported through the electrolyte. The electrons are transported through an external circuit and recombined at the cathode with the cathode material in a reduction reaction. During charging, lithium ions combine with the external electrons and are deposited as atoms between carbon layers. Copper and aluminum collectors on the anode and the cathode collect and distribute electrons. Both electrodes allow lithium ions to move in and out of their structure (insertion-intercalation and extraction-deintercalation) [20,21].

In a typical LCO battery, the anode is graphite (where Lithium is intercalated), and the cathode is cobalt oxide,  $Co^{4+}O_2^{2-}$ , where the cobalt wants to gain back an electron by lithium intercalation. The lithium balances the charge build up:



During charging/discharging, the voltage at the terminals is not equal to the open-circuit battery voltage (OCV). The OCV is the terminal potential difference when no current flows and is caused by chemical forces in the battery. The maximal potential

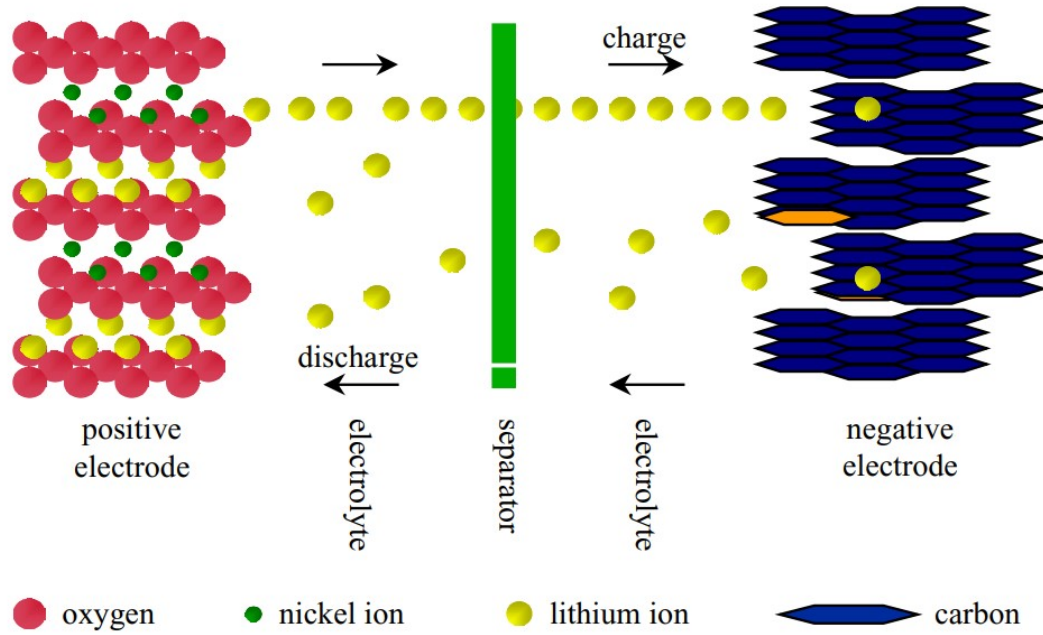


**Figure 2.2.** Lithium ion migration during charge or discharge [20].

difference is called electromotive force (EMF) and its value for Li-ion batteries ranges from 2.4 V to 3.8 V, depending on the electrode types. The dynamics of a Li-ion battery contains multiple timescales. During charging/discharging the voltage at the terminals has an instant drop, due to the electrode material resistance and the electrolyte resistance, and a transient behavior caused by polarization.

### 2.1.1 Li-ion battery parameters

A battery's capacity is the amount of electric charge it can deliver at the rated voltage. The more electrode material contained in the cell, the greater its capacity. The capacity is usually expressed in Ampere-hours (Ah). For example, the capacity of 1 Ah equals to 1A of current flowing for an hour and is equal to 3600 Coulombs. In energy optimization problems the capacity is expressed in Watt-hours, defining the amount of energy a battery can provide. The performance of the battery and the achievable capacity depends on the operating conditions. The internal processes of the Li-ion battery depend on the current rate, the state of charge and temperature of the battery.

Current rate (C-rate) is the rate at which a battery is being charged/discharged. It compares the current through the battery to the theoretical current draw under which the battery would deliver its nominal rated capacity in one hour. For example, for 500 mAh, discharge rate of 5000 mA corresponds to a C-rate of 10 ( $\text{C-rate} = 5000 \text{ mA} / 500 \text{ mA} = 10$ ).

The lithium intercalation and deintercalation are not uniform in the electrode. An ion concentration gradient is formed within the electrodes which causes the diffusion of ions

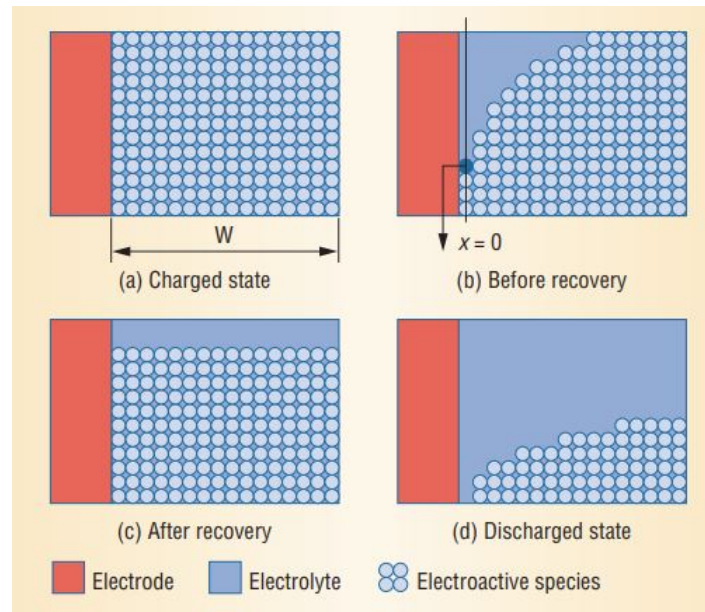


**Figure 2.3.** Lithium ion rate capacity effect [22].

within the electrodes (solid phase diffusion). The transport of lithium ions to the active material surface through the electrolyte is called liquid phase diffusion and is quicker than the solid phase diffusion [21]. At higher C-rates, the active material at the electrode surface is depleted much quicker resulting in lower usable battery capacity. During relaxation periods, when no current is applied, the ion concentration reaches equilibrium and capacity recovery effect occurs due to the diffusion processes in the battery.

The broad usage of batteries nowadays caused the need for battery management systems which are in charge of monitoring the battery states, such as state of charge (SOC) and state of health (SOH) and different charging/discharging algorithms. State of charge is the level of charge of an electric battery relative to its capacity (0% - empty battery, 100% full battery). Depth of discharge (DOD) is the complement of SOC. However, in energy management systems (EMS), the traditional SOC is replaced with the state of energy index (SOE), since it incorporates the battery's internal losses and the effects of the variable OCV. The SOE is defined as the ratio between the consumed energy during a time interval and the total available energy and it offers useful information about the available discharging/charging energy [23].

At lower temperatures, the battery internal resistance increases because of decreased chemical activity, resulting in a reduced battery capacity. The internal resistance represents the electrode material and electrolyte resistance which hinder the current flow. At higher temperatures due to improved electrochemical reactions battery performance is improved however prolonged exposure shortens the battery life [24]. The internal resistance is also affected by the battery SOC, increasing at high and low states with a lower, less variable value in the middle ranges [25].

Battery state of health is the ratio between the current battery capacity and the



battery nominal capacity. The battery capacity fades with cycling and calendar aging as a consequence of electrolyte decomposition, active material dissolution and the solid electrolyte interface (SEI) growth [22]. The SEI is a semi-porous protective layer generated by the manufacturer to prevent the overexposure of the anode to the electrolyte. High temperatures and charging currents cause degradation [26,25]. The heat energy causes more lithium ions to react with the electrolyte leading to SEI growth which increases the battery internal resistance inhibiting the free flow of electrons. Also, at high temperatures, side reactions occur, resulting in the evolution of highly flammable gases [27]. Charging at low temperatures slows down the reaction rate depositing Lithium ions on the surface of the anode, without intercalation [24].

## 2.2 Battery equivalent models

Depending on the application, different battery models are consequently developed in order to simulate battery dynamics. A state-of-energy (SOE) model, described in [28], observes the energy exchanged with the microgrid and storage but omits internal battery processes and results in sub-optimal management systems. More detailed models mainly fall into three categories: mathematical models, electrochemical models, and equivalent circuit models.

Mathematical models are mostly analytical or data fitting black-box models that rely on high amount of input/output data to model battery dynamics. These models are not reliable at different operating conditions and often cannot capture the battery current-voltage (I-V) characteristics. Peukert's law is an empirical expression for determining battery runtime as a function of the discharge rate [29]. Another popular analytical model is the Kinetic Battery Model (KiBaMo) (Fig.2.4) which describes the chemical processes by a kinetic process. The charge distribution is modelled via two connected tanks. The outgoing flow, regulated with a valve, simulates battery discharging and the height of the fluid inside the corresponding tank represents the available charge. The second tank represents the charge inside the electrode and the flow between them simulates the diffusion process inside the electrode, thus imitating current rate effect as well as capacity recovery [30].

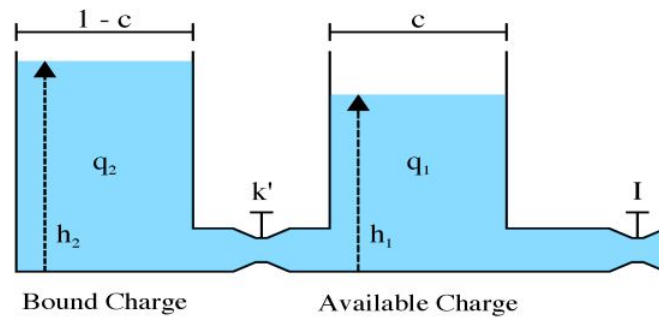


**Figure 2.4.** Kinetic Battery Model [30].

Electrochemical models, for example single particle models (SPMs) (Fig.2.5), involve partial differential equations which describe electrochemical reactions in a battery during charging/discharging [31]. Although these models accurately simulate battery behavior, they require physical and chemical characteristics of the batteries and their complexity induces high computational costs.

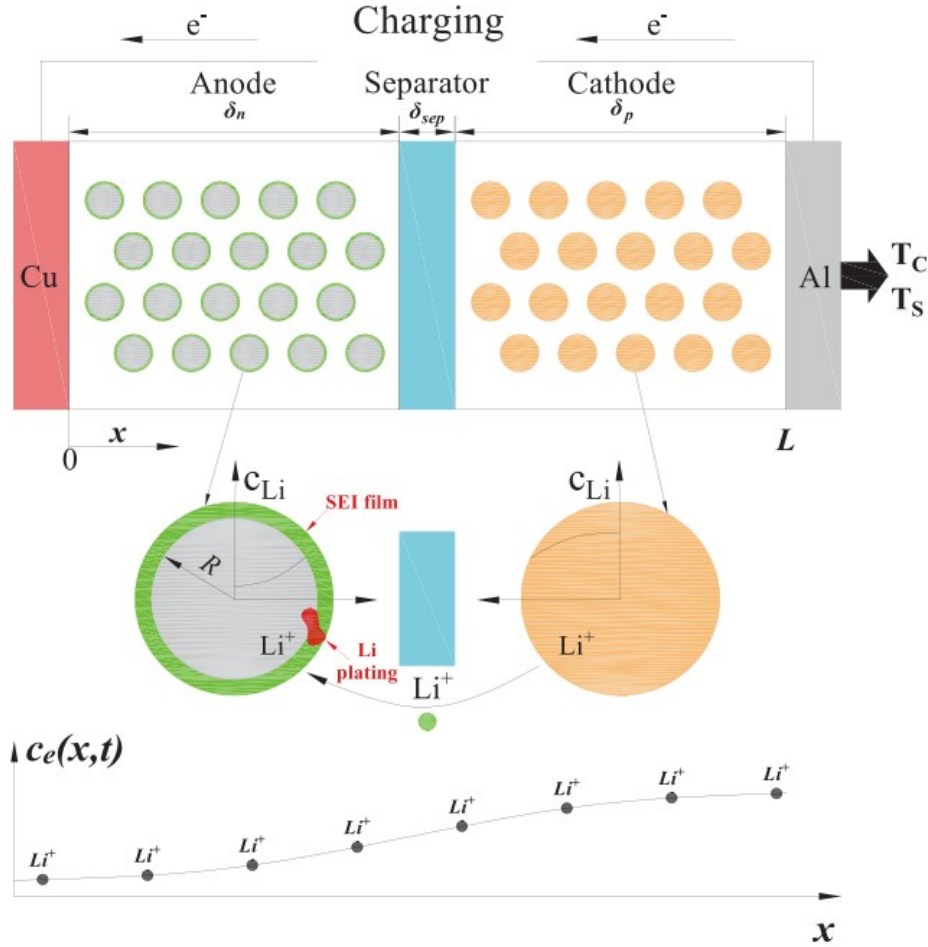
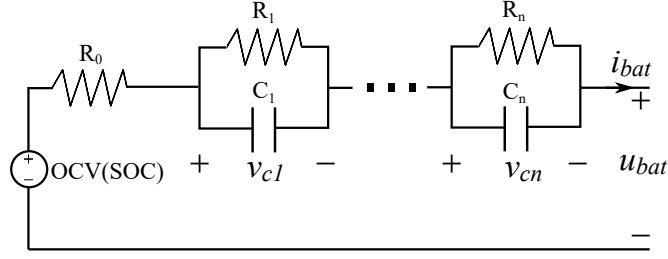


Figure 2.5. Single particle model [31].

### 2.2.1 Equivalent circuit models

Equivalent circuit models (ECMs) use electric circuits consisting of voltage/current sources, resistors, capacitances, and inductances in order to replicate the battery behavior [32]. Impedance based models use ac-equivalent impedance to fit the impedance spectra. They work for a fixed SOC and are not able to predict battery runtime. Runtime based models predict battery runtime however, have limited transient behavior accuracy.

Most commonly used model is the Thevenin model. The basic Thevenin's model consists of a constant open-circuit voltage and a series resistor. The series resistor represents the internal resistance of the electrolyte to the propagation of the ions. The battery terminal voltage transient response is modeled by adding parallel RC circuits



**Figure 2.6.** Thevenin equivalent circuit model.

to the basic model. The model becomes more accurate by adding several RC circuits with different time constants (Figure 2.6). However, for most applications one or two RC circuits are proven to be accurate enough. Thevenin-based models however, fail to capture battery voltage steady-state variations and runtime information [32], [4]. Another

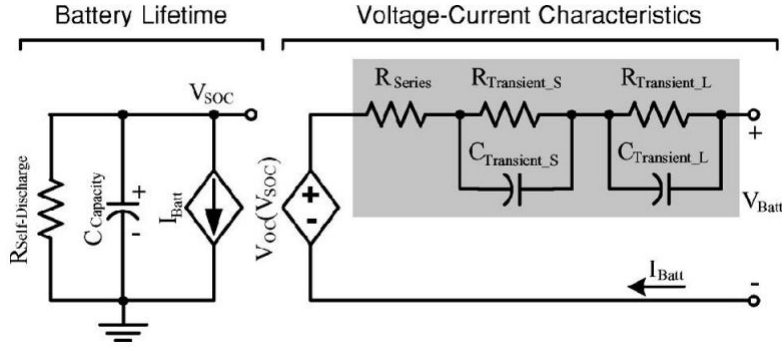


**Figure 2.7.** Hybrid electrical circuit model [32].

popular ECM is the hybrid model which is capable of predicting the battery runtime and voltage responses. The hybrid model is considered the most precise of the four while it is still simple in comparison with electrochemical models. It consists of two parts (Fig. 2.7). The first part consists of a capacitor, which represents the batteries charge, and a current-controlled current source. This part models the battery's state of charge (SOC). The second part is similar to a Thevenin-based model. It typically consists of a series resistor and two RC circuits which capture the transient response. The voltage source is SOC-dependent and since this dependency is nonlinear, the model becomes nonlinear [32].

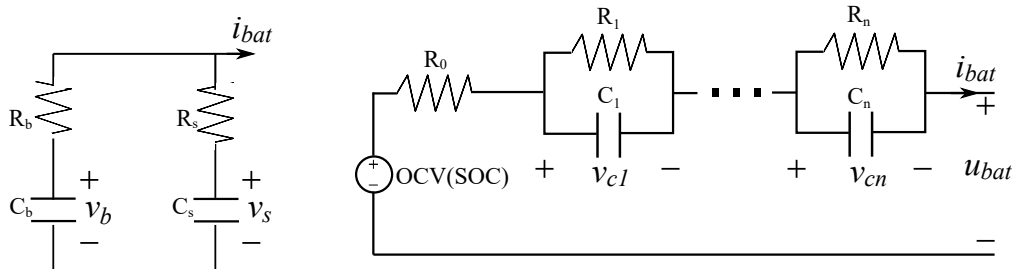


**Figure 2.8.** Nonlinear double-capacitor equivalent circuit model.

The double-capacitor model is recently proved as a promising approach from the perspective of model simplicity and increased accuracy [33]. The capacitors differ in capacitance thus imitating the electrode surface (which charges more quickly) and its bulk inner part (charging slowly). The surface capacitor voltage rises/declines more quickly at high currents thus simulating the current rate effect. The capacitor recovery is the result of the charge migration from one capacitor to the other, during relaxation period. However, this model cannot describe the battery's nonlinear behaviour. This is improved in [6] where a nonlinear double-capacitor model (NDC) is presented. This model consists of two parts as depicted in Fig.2.8. The first part models the electrode behaviour, simulating the distribution and migration of the charge and the second part models the voltage transients. The choice of the model for control application is a trade-off between accuracy and complexity.

Although all the described models have their advantages and disadvantages, the Thevenin model is chosen for control algorithm design, as a good trade off between model complexity and accuracy.



---

# Identification of a nonlinear battery model

## 3.1 Battery model parameter identification methods

Different battery states and parameters identification methods are found in literature. The common methods of estimating the battery state of charge (SOC) include coulomb counting, open-circuit voltage (OCV) method and different Kalman filters (KFs). The coulomb counting method measures the battery current and integrates over time. This is the simplest method for SOC estimation, but its accuracy highly depends on the sensor accuracy and accurate initial SOC. The OCV method consists of measuring the battery voltage in steady-state and reading the SOC from the OCV-SOC curve. This method isn't applicable in online estimation because it's accuracy depends on the battery relaxation time which is several hours. The most popular method are different Kalman filters such as extended KF and sigma-point KF [5,34,35]. The state of energy (SOE) estimation is similarly categorized into three methods: direct methods, model-based methods and data-driven methods. The power integration method is the simplest. However, like the coulomb counting method it is prone to error accumulation due to sensor accuracy. Model based approaches consist of different Kalman filters while data-driven methods rely on artificial intelligence [23,36,37]. Parameter estimation is divided into online and offline estimation. Offline estimation is based on already collected data. The parameters can be read off the voltage curves obtained from pulse tests [38,39]. Also, different artificial intelligence and standard least square (LS) are common examples of offline identification. The drawback of these methods is its inability to adapt to different operating conditions. Joint and dual KFs are often used with SOC estimation [40,41]. Another widely used method is the LS method and variations for online identification. In [42] moving horizon LS is presented, where during a time interval the SOC is presumed to be constant, parameter identification is performed. Then, after a new measurement is available, the first data sample is replaced with it and identification is performed again. This procedure is repeated

every time instant. Recursive LS with forgetting factor is described in [34,43] where a more weight is put on new incoming data in order to avoid data saturation. A LS and extended Kalman filter (EKF) combination is used in [44], where temperature and SOC dependencies are observed. Repeated tests are performed to obtain data sets for different SOC and temperatures and identification is performed for each data set to obtain an accurate model which is then used for SOC estimation with EKF. The obtained LS problem for parameter estimation is solved using *Simulink Design Optimization toolbox*.

In the following sections, parameter identification method based on LS is presented. Different complexity Thevenin models are used for the identification: i) internal resistance model (R0 model), ii) one RC circuit model (1RC model), and iii) two RC circuit model (2RC model). The results are compared and advantages and disadvantages of each model are discussed. The 2RC model showed best results and is the base for the battery efficiency model developed at the end of this chapter.

### 3.2 Battery model identification procedure using Linear least-squares (LLS) method

The battery and microgrid control algorithms require a known variable battery model. Therefore, offline identification is preferred for this work. The goal is to obtain parameters that depend on SOC. The environment temperature is assumed constant and current rate effects are incorporated via power losses over the identified parameters. A 2RC Thevenin model, depicted in Fig.3.1 is chosen for the battery equivalent model because it models the fast and the slow transients. The state space model is given with following equations:

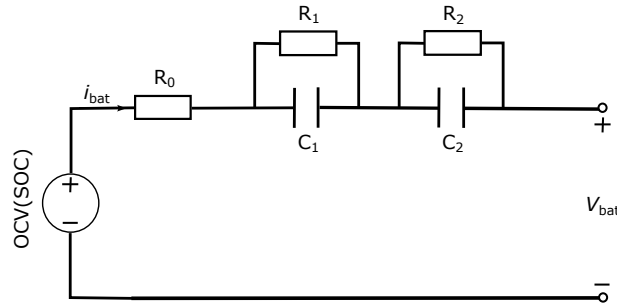


**Figure 3.1.** Two RC circuit Thevenin model.

$$\dot{x} = \begin{bmatrix} \dot{v}_{c1} \\ \dot{v}_{c2} \\ \dot{\text{SOC}} \end{bmatrix} = \begin{bmatrix} -\frac{1}{R_1 C_1} & 0 & 0 \\ 0 & -\frac{1}{R_2 C_2} & 0 \\ 0 & 0 & 0 \end{bmatrix} \begin{bmatrix} v_{c1} \\ v_{c2} \\ \text{SOC} \end{bmatrix} + \begin{bmatrix} \frac{1}{C_1} \\ \frac{1}{C_2} \\ -\frac{1}{C_{\text{bat}}} \end{bmatrix} i_{\text{bat}} \quad (3.1)$$

$$\text{OCV}(t) = f(\text{SOC}(t)), \quad (3.2)$$

$$u_{\text{bat}}(t) = \text{OCV}(t) - u_{\text{RC}}(t), \quad (3.3)$$

where  $u_{\text{bat}}$  and  $i_{\text{bat}}$  are the battery terminal voltage and current,  $u_{\text{RC}}(t)$  is the voltage drop over the internal resistance  $R_0$  and the two RC circuits, and  $x$  encompasses model states: fast transient RC circuit voltage  $v_{c1}$ , slow transient RC circuit voltage  $v_{c2}$ , and battery state of charge SOC. The discharging current in this model is positive. The LS methods are the most common offline solution in literature for the parameter identification process, however all the aforementioned methods neglect battery hysteresis in order to simplify the model. In order to increase the accuracy of the model, which is further used in control algorithms, a LS method described in [45] is chosen for identification. The method is based on the detrended battery voltage and standard LS method. The parameters are divided into several SOC intervals and considered constant within each interval. In [45], both the OCV curve and the SOC dependent parameters are determined using one set of measurements - one full charging/discharging cycle is performed with a noisy current profile, removing the need for separate identification procedure for the OCV-SOC curve identification. The measured voltage is into intervals and detrended. Detrending removes polynomial trends from data. An example of removing a linear trend from a dataset is shown in Fig.3.2. The blue line represents the original data and the orange line is the data obtained by removing the linear trend (yellow line) from the original data. The same procedure is applied to voltage measurements assuming a linear OCV trend in smaller time intervals.

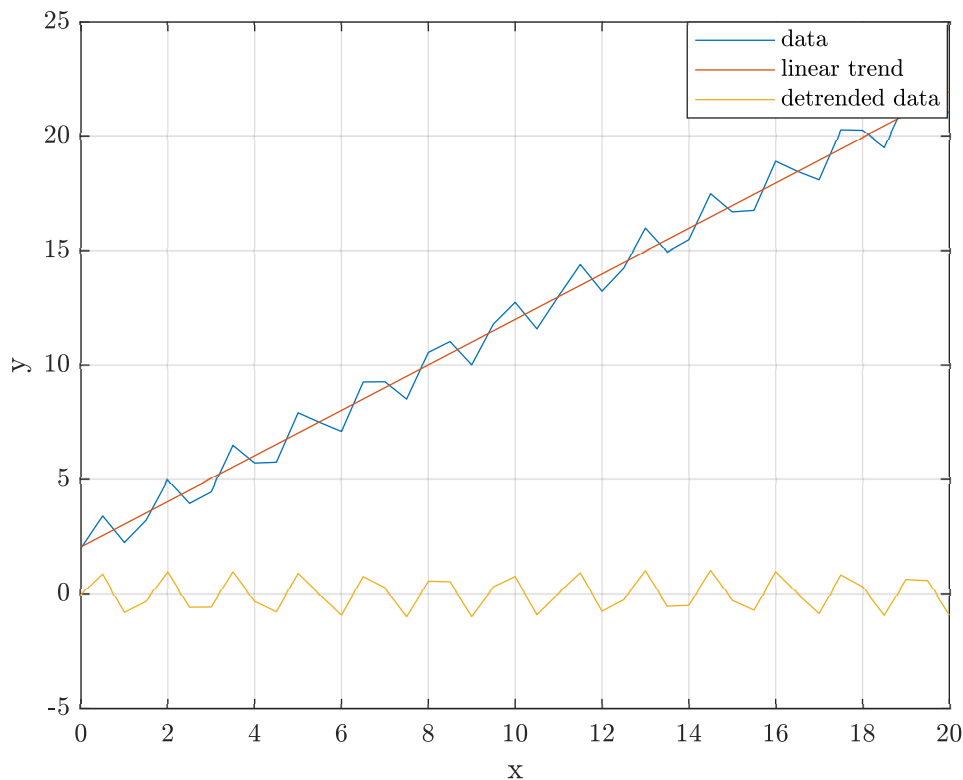


**Figure 3.2.** Example of removing a linear trend from a dataset.

In this way the OCV curve and the contribution of the gain of the model are removed. The accuracy of the detrending increases by increasing the number of intervals, however, in



this way the complexity of the model is also increased. The data obtained after detrending,  $\Delta u_{\text{bat}}(t)$ , is:

$$u_{\text{bat}}(t) = \text{OCV}(t) - K\bar{i}_{\text{bat}}(t) - \Delta u_{\text{RC}}(t) \rightarrow \Delta u_{\text{bat}} = \Delta u_{\text{RC}}(t) = G(s)\Delta i_{\text{bat}}(t), \quad (3.4)$$

$$G(s) = \frac{u_{\text{RC}}(t)}{i_{\text{bat}}(t)} = \frac{R_0 T_1 s^2 + (R_0 T_1 + R_0 T_2 + R_2 T_1 + R_1 T_2)s + K}{T_1 T_2 s^2 + (T_1 + T_2)s + 1}, \quad (3.5)$$

where  $K = R_0 + R_1 + R_2$  is the model gain and  $T_1 = R_1 C_1$ ,  $T_2 = R_2 C_2$  are the RC circuits time constants. The identification procedure is performed on a 4.8 Ah Li-ion battery with a 0.2C current. The sample time is set to  $T_s = 1$  s, an order of magnitude smaller than the expected time constant of the fast RC circle  $T_1$ . However, the identification of the time constant of the slower RC circuit, which is several magnitudes higher than the chosen sample time, was not successful in every time interval because its effect is less visible in the data in small time intervals and with such a small sampling time. The problem can be solved by using a different current profile, higher sampling time and bigger time intervals, however without any knowledge about the magnitude of the considered battery parameters the identification procedure becomes less general. Also, by reducing the number of intervals, the accuracy of the model is also reduced, which affects the control algorithm. Therefore, the order of the ECM is reduced, and previous data is resampled to  $T_s = 10$  s which is deemed big enough to capture the slow RC circuit effect and still small enough to capture the fast voltage transients. The previous model then becomes:

$$G(s) = \frac{U_{\text{RC}}(s)}{I_{\text{bat}}(s)} = \frac{R_0 T_1 s + K}{T_1 s + 1}, \quad (3.6)$$

$$K = R_0 + R_1, \quad T_1 = C_1 R_1. \quad (3.7)$$

The first order continuous transfer function in the discrete domain is:

$$G(z) = \frac{\Delta U_{\text{bat}}(z)}{\Delta I_{\text{bat}}(z)} = \frac{b_1 z + b_0}{z + a_0} = \frac{b_1 + b_0 z^{-1}}{1 + z^{-1}}. \quad (3.8)$$

The discrete transfer function (3.8) can be written in form of difference equations:

$$\Delta U_{\text{bat}}(k) = -a_0 \Delta U_{\text{bat}}(k-1) + b_1 \Delta I_{\text{bat}}(k) + b_0 \Delta I_{\text{bat}}(k-1), \quad (3.9)$$

where  $U_{\text{bat}}(k)$  is the detrended measurement data at the  $k$ -th time instant and  $I_{\text{bat}}(k)$  is the detrended current at the  $k$ -th time instant. The model written in vector form is:

$$\Phi \mathbf{x} = \mathbf{U}, \quad \mathbf{x} = [a_0 \quad b_1 \quad b_0]^\top \quad (3.10)$$

$$\Phi = [-\mathbf{U}_{k-1} \quad \mathbf{I}_k \quad \mathbf{I}_{k-1}], \quad (3.11)$$

$$\mathbf{U} = [\Delta U_{\text{bat}}(2) \cdots \Delta U_{\text{bat}}(n)]^\top, \quad (3.12)$$

$$\mathbf{U}_{k-1} = [\Delta U_{\text{bat}}(1) \cdots \Delta U_{\text{bat}}(n-1)]^\top, \quad (3.13)$$

$$\mathbf{I}_k = [\Delta I_{\text{bat}}(2) \cdots \Delta I_{\text{bat}}(n)]^\top, \quad (3.14)$$

$$\mathbf{I}_{k-1} = [\Delta I_{\text{bat}}(1) \cdots \Delta I_{\text{bat}}(n-1)]^\top, \quad (3.15)$$

where  $n$  is the number of samples in one SOC interval. The coefficients are then calculated using the expression:

$$\Phi \mathbf{x} = \mathbf{U} \quad \rightarrow \quad \mathbf{x}^\top = (\Phi^\top \Phi) \backslash \Phi^\top \mathbf{U}. \quad (3.16)$$

After calculating the coefficients of the discrete function, inverse zero-order-hold (ZOH) method is used in order to obtain the parameters  $R_0$ ,  $R_1$  and  $T_1$  of the continuous transfer function from (3.6). The parameters with respect to SOC are shown in Fig.3.3, where the battery SOC is divided into 10 intervals, resulting in a 10%  $\Delta\text{SOC}$  between each interval. The parameters are a combination of the slow and fast dynamics which is visible in the  $T_1$  fluctuations. The OCV curves are obtained from (3.4) by calculating the charging/discharging gain in each SOC interval and then fitting the curve to a 5th order polynomial as suggested in [45]. The hysteresis is observed in all results, however a more distinct difference in OCV curves was expected, especially in the lower SOC ranges. Simulation of the identified model is shown in Fig.3.4. The model is simulated with the same current with which the identification is performed and the comparison of the initial voltages and the voltages obtained from the model is shown in the second subfigure. The error between the voltages is shown in the third subfigure. The error is more prominent at lower SOC values, which is expected since the parameters are higher in this interval, resulting in higher errors from the simplified model.

The same identification procedure is performed with 20 and 40 SOC intervals which correspond to 5%  $\Delta\text{SOC}$  and 2.5%  $\Delta\text{SOC}$  (Figs.3.5-3.7). The accuracy of the model is improved with more SOC intervals which is observed from the voltage comparison subfigure for every case. The models, obtained with more SOC intervals, show the hysteresis effect in the OCV-SOC curves as well as the parameters. A comparison of the mean-square errors (MSE) for all three identified models and the algorithm execution times are presented in Table3.1. The best result is, as expected, obtained with 40 SOC intervals. The execution time is the longest in this case, however, the calculation is under one 1 s for all the three identification models.

**Table 3.1.** Comparison of the MSE and execution times for the LLS algorithm of the 1RC model.

$\Delta\text{SOC}$	10%	5%	2.5%
MSE	0.0051	0.0024	6.4205e-4
$t_{\text{ex}}$	0.06 s	0.11 s	0.22 s

Using the same procedure, a simple model with only the internal resistance is also identified and compared to the 1RC model in order to see how the model accuracy is affected by this model simplification. The results are shown in Figs.3.9and3.10. The internal resistance values are similar in both models, for all SOC intervals.

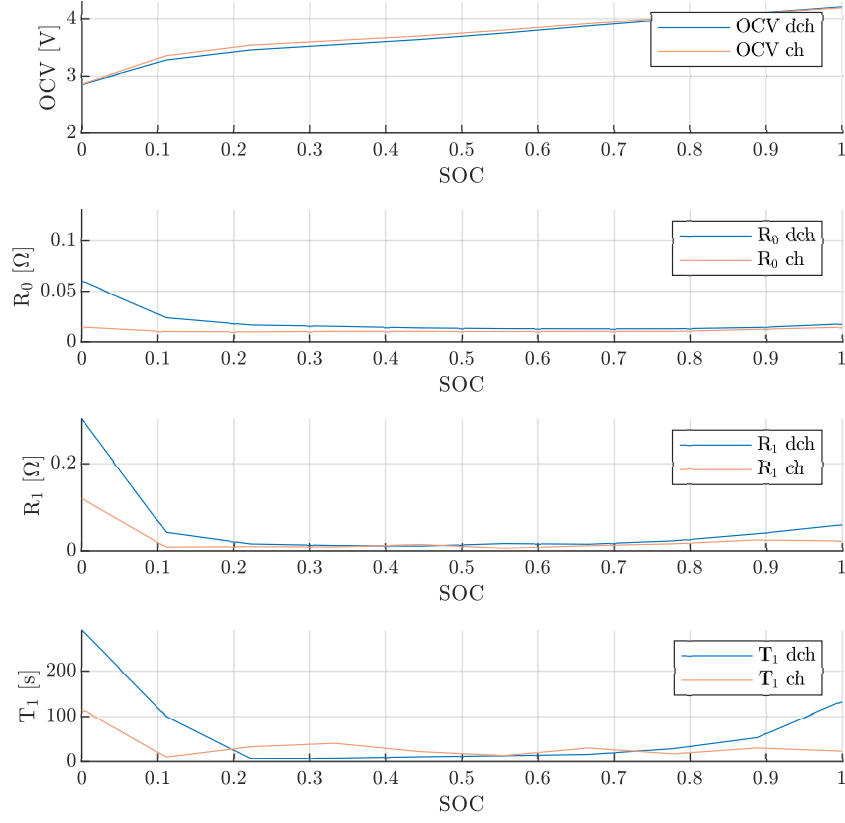


**Figure 3.3.** Parameters of the battery 1RC model dependent on the SOC,  $\Delta\text{SOC} = 10\%$ .

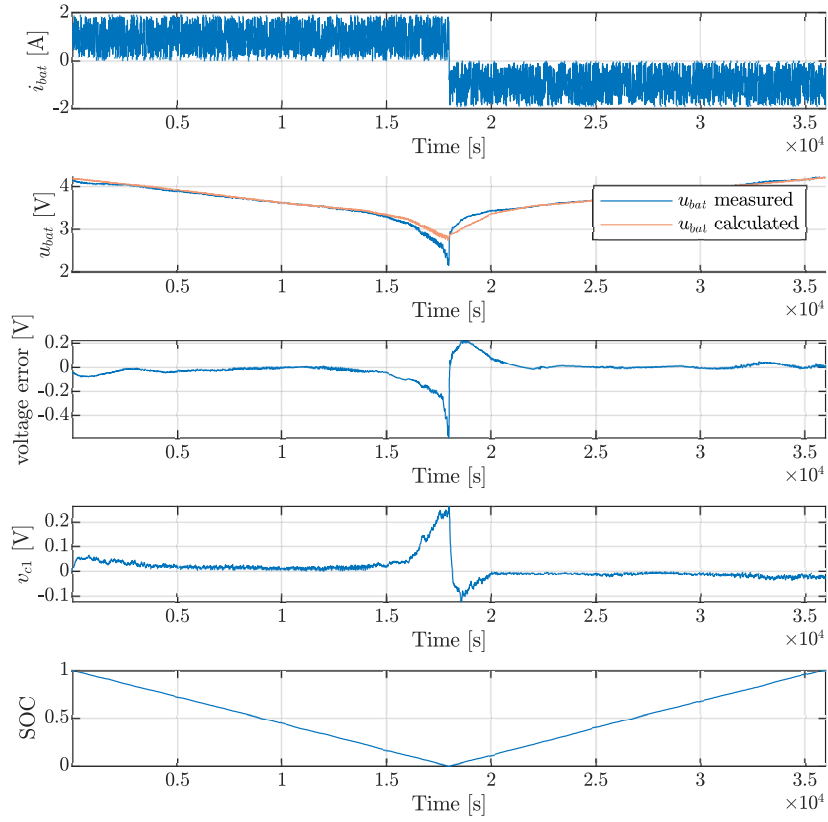


**Figure 3.4.** Simulation of the identified 1RC battery model,  $\Delta\text{SOC} = 10\%$ .

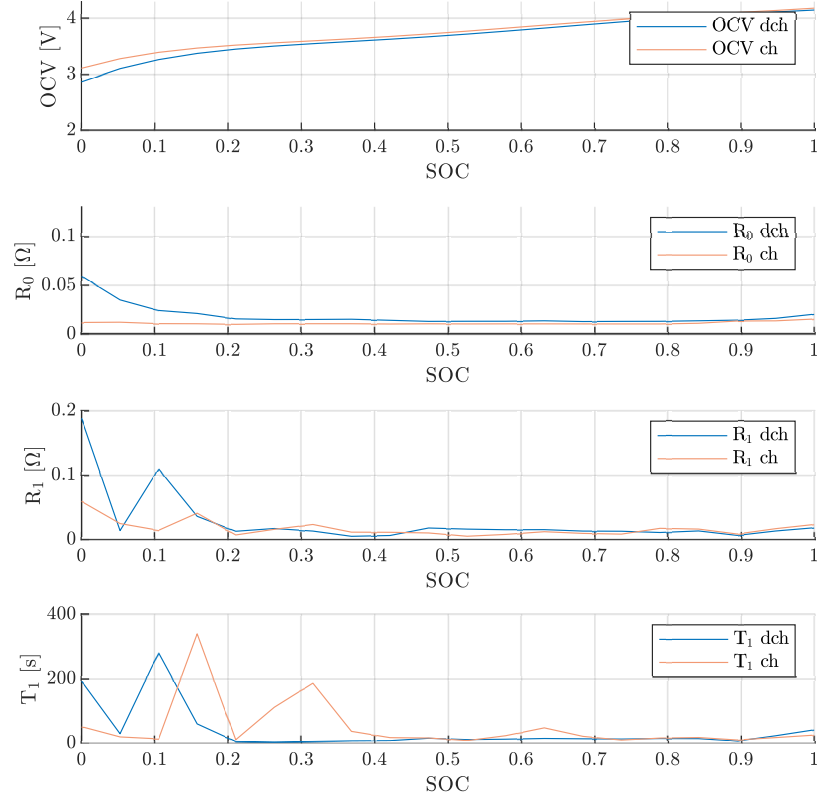


**Figure 3.5.** Parameters of the battery 1RC model dependent on the SOC,  $\Delta\text{SOC} = 5\%$ .

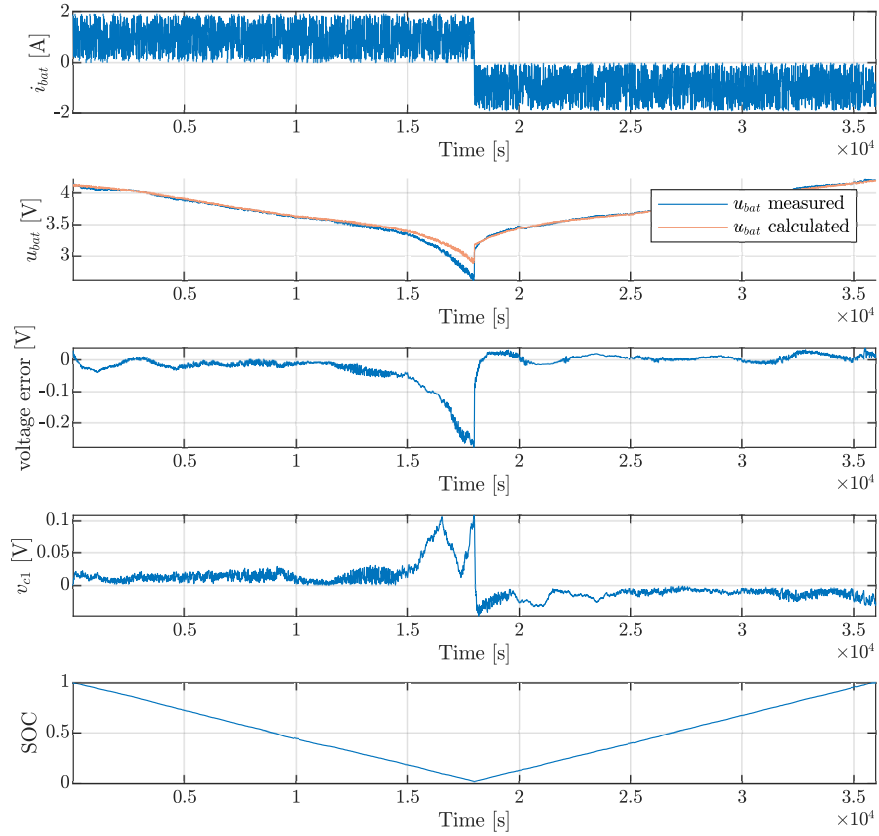


**Figure 3.6.** Simulation of the identified 1RC battery model,  $\Delta\text{SOC} = 5\%$ .

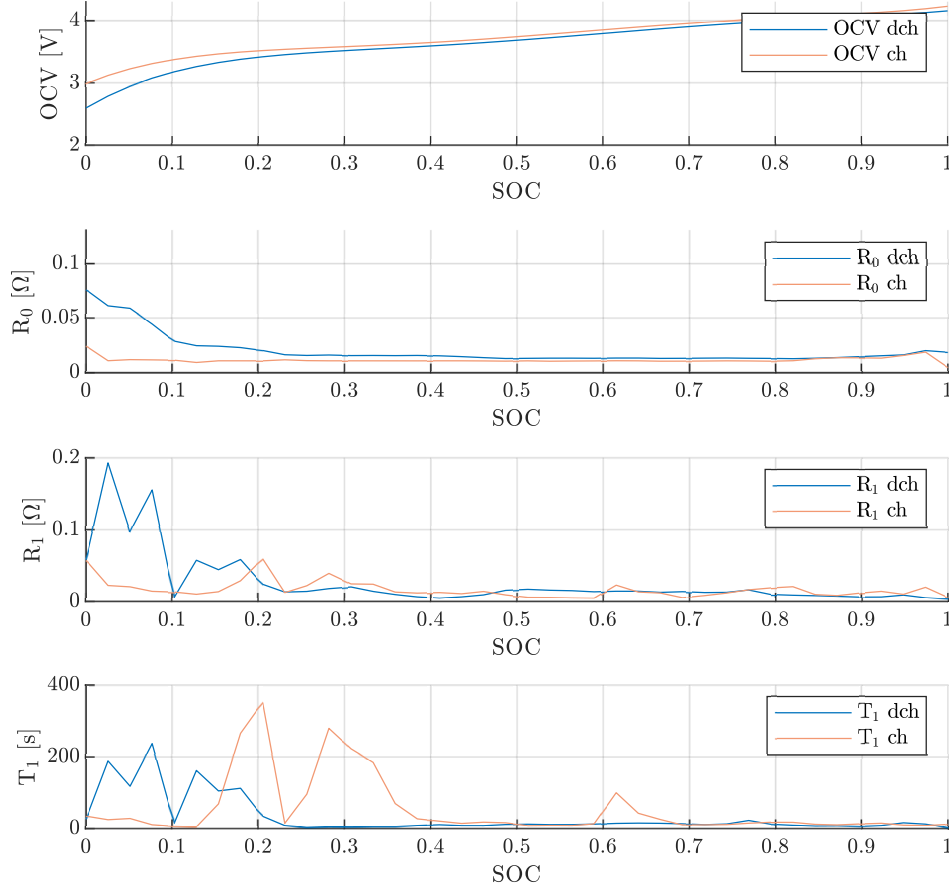


**Figure 3.7.** Parameters of the battery 1RC model dependent on the SOC,  $\Delta\text{SOC} = 2.5\%$ .

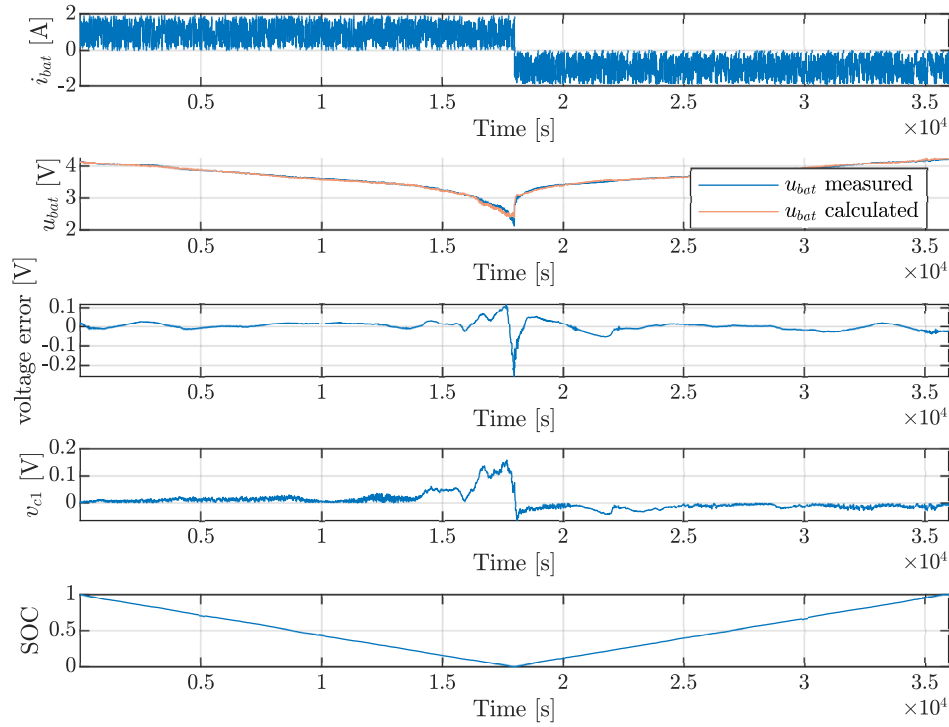


**Figure 3.8.** Simulation of the identified 1RC battery model,  $\Delta\text{SOC} = 2.5\%$ .

However, the OCV charging and discharging curves are different than the previous model. The algorithm achieved a good model accuracy by adjusting these curves, resulting in  $MSE = 5.3455e-4$ . Since this is a better result than the model with the RC circuit, both models are validated on a different current profile (Figs.3.11and3.12). The 1RC model matches better with the validation dataset<sup>1</sup>, especially during periods with transients as shown in Fig.3.13. The MSE of the R0 model is 0.0017 while the MSE of the 1RC circuit model is  $6.8217e-4$ , showing that the added RC circuit is more accurate.

The described algorithm successfully identifies the basic and the first order Thevenin model and offers insight into how model simplification deteriorates the remaining parameters in order to achieve a good fit to the measurement data. Since the slow time constant cannot be successfully identified with this algorithm, another identification procedure is proposed in the subsequent section.

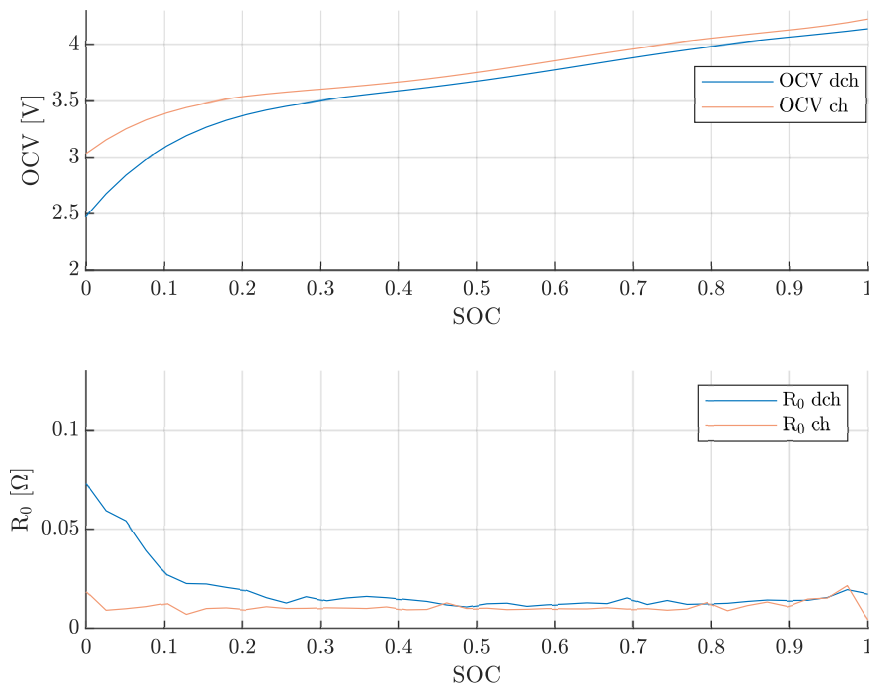


**Figure 3.9.** Parameters of the R0 model dependent on the SOC,  $\Delta SOC = 2.5\%$ .

<sup>1</sup>Experimental data from the battery cell are obtained from the company Rimac Technology d.o.o. as part of cooperation of FER with the company Rimac Technology d.o.o. on the project EVBattPredtect – Dynamic Predictive Health Protection of an Electric Vehicle Battery, co-financed from the European Regional Development Fund via Operative Programme Competence and Cohesion 2014-2020 (project no. KK.01.1.1.07.0029).

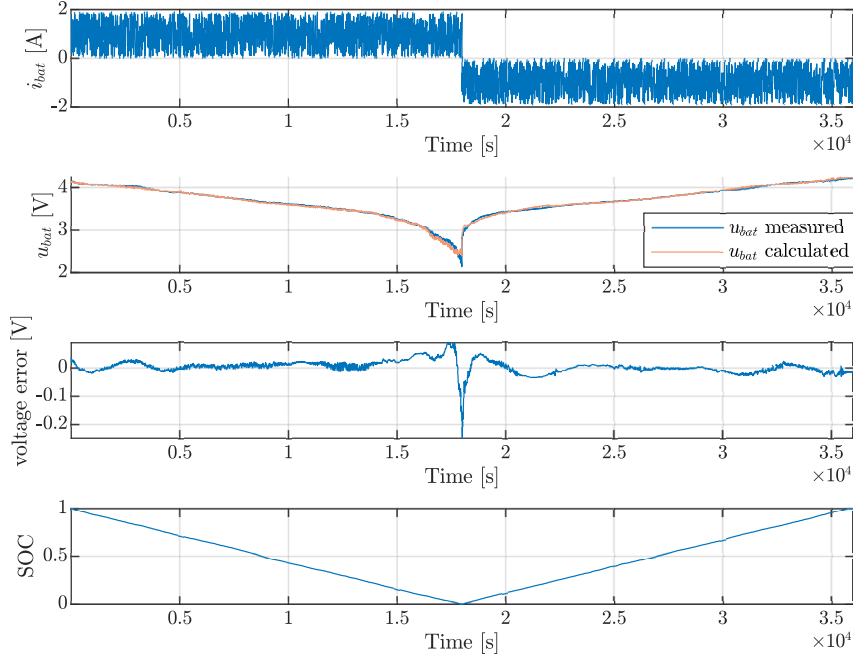


**Figure 3.10.** Simulation of the identified R0 model,  $\Delta\text{SOC} = 2.5\%$ .

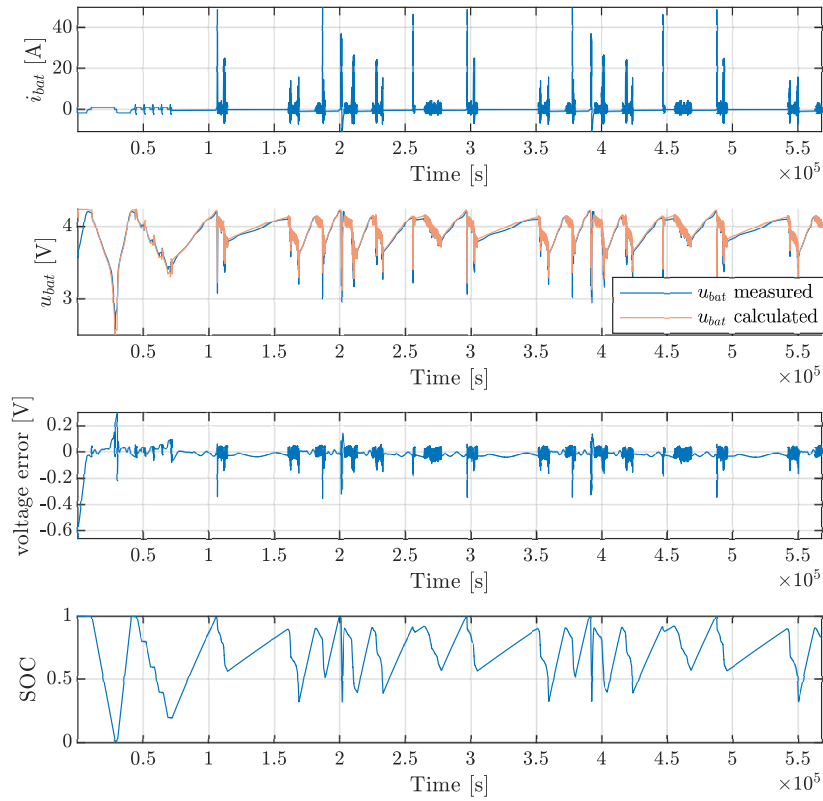


**Figure 3.11.** Simulation of the identified R0 model based on a new dataset<sup>1</sup>.

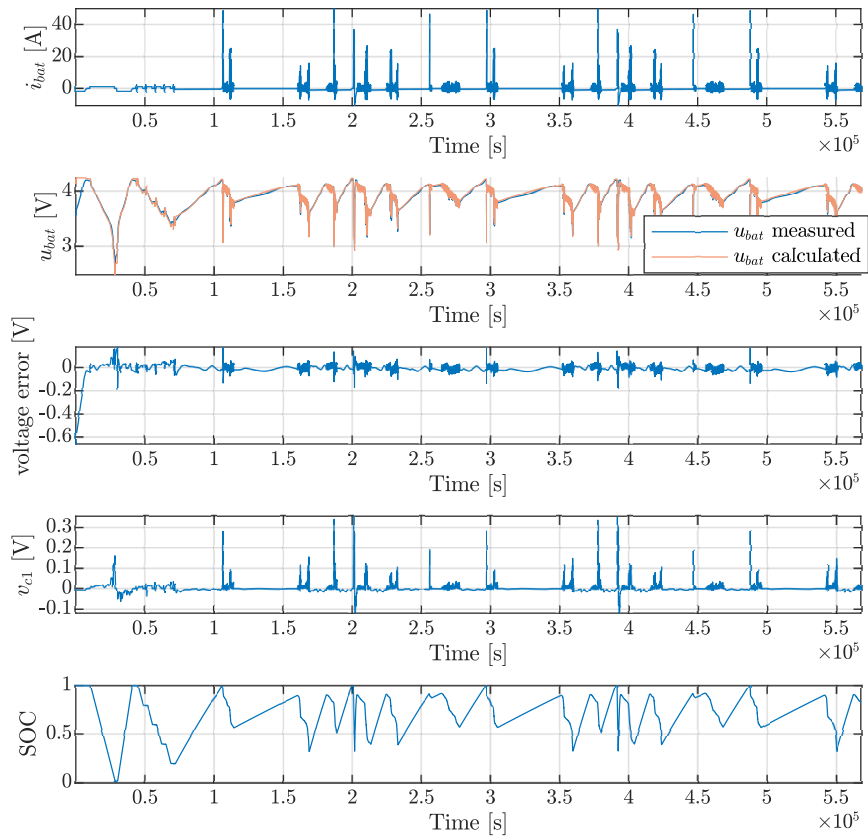


**Figure 3.12.** Simulation of the identified 1RC battery model on a new dataset<sup>1</sup>.

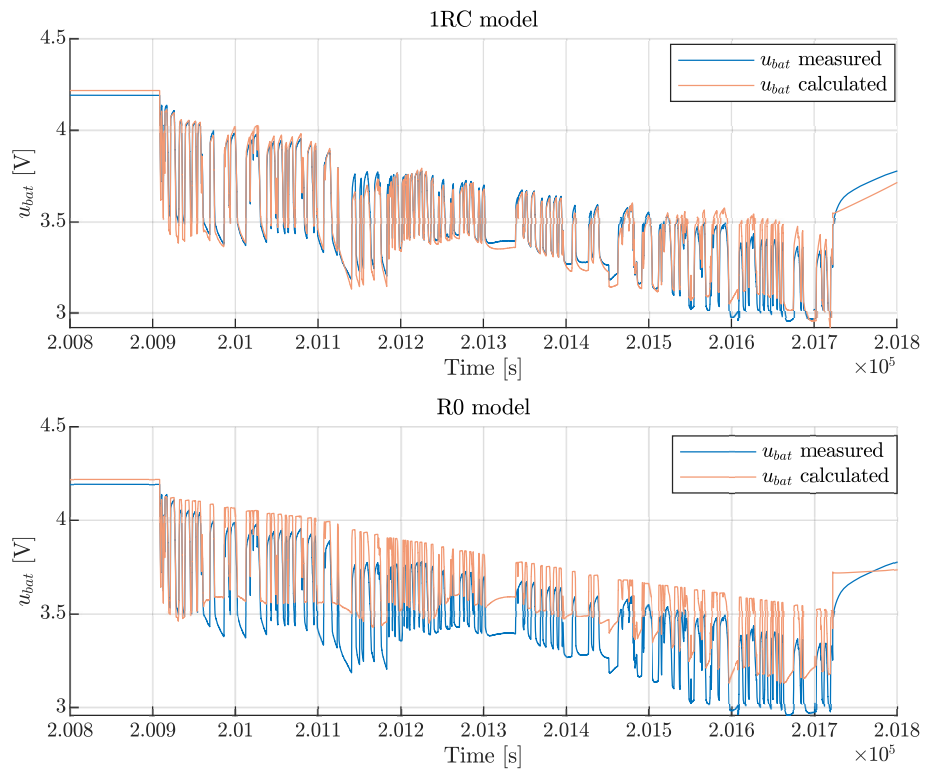


**Figure 3.13.** Comparison of the 1RC model with the R0 model during transients on a new dataset<sup>1</sup>.



### 3.3 Constrained combined least-square parameter identification

In this section, the identification is performed on the 2RC model, using a constrained least-square optimization formulation as follows:

$$\min_{\mathbf{x}} \|\mathbf{U}_{\text{bat}} - \mathbf{U}_{\text{bat,mj}}\|_2, \quad (3.17)$$

$$\mathbf{x} = [C \quad \text{OCV} \quad \mathbf{R}_0 \quad \mathbf{R}_1 \quad \mathbf{T}_1 \quad \mathbf{R}_2 \quad \mathbf{T}_2 \quad u_{c1}(0) \quad u_{c2}(0) \quad \text{SOC}(0)]^\top, \quad (3.18)$$

$$\text{OCV} = [\text{OCV}_{\text{dch}} \quad \text{OCV}_{\text{ch}}]^\top, \quad (3.19)$$

$$\mathbf{R}_0 = [\mathbf{R}_{0,\text{dch}} \quad \mathbf{R}_{0,\text{ch}}]^\top, \quad (3.20)$$

$$\mathbf{R}_1 = [\mathbf{R}_{1,\text{dch}} \quad \mathbf{R}_{1,\text{ch}}]^\top, \quad (3.21)$$

$$\mathbf{T}_1 = [\mathbf{T}_{1,\text{dch}} \quad \mathbf{T}_{1,\text{ch}}]^\top, \quad (3.22)$$

$$\mathbf{R}_2 = [\mathbf{R}_{2,\text{dch}} \quad \mathbf{R}_{2,\text{ch}}]^\top, \quad (3.23)$$

$$\mathbf{T}_2 = [\mathbf{T}_{2,\text{dch}} \quad \mathbf{T}_{2,\text{ch}}]^\top. \quad (3.24)$$

Several constraints are added to assure an applicable solution:

$$\text{OCV}_{\text{dch}}(k) \leq \text{OCV}_{\text{dch}}(k+1), \quad k = 1 \cdots n, \quad (3.25)$$

$$\text{OCV}_{\text{ch}}(k) \leq \text{OCV}_{\text{ch}}(k+1), \quad k = 1 \cdots n, \quad (3.26)$$

$$\text{OCV}_{\text{dch}}(k) \leq \text{OCV}_{\text{ch}}(k), \quad k = 1 \cdots n, \quad (3.27)$$

$$R_1(k) \leq R_0(k), \quad k = 1 \cdots 2n, \quad (3.28)$$

$$R_2(k) \leq R_0(k), \quad k = 1 \cdots 2n, \quad (3.29)$$

$$2T_2(k) \leq T_1(k), \quad k = 1 \cdots 2n, \quad (3.30)$$

$$T_1(k) \leq T_{\text{max}}, \quad k = 1 \cdots 2n. \quad (3.31)$$

The problem is solved using a MATLAB built-in function which uses an interior-point algorithm. The model parameters are divided into 40 intervals with  $\Delta\text{SOC} = 2.5\%$ , and bounded from below to zero. The OCV is added to the problem as an additional parameter in every time instant. The initial point is set randomly to a feasible value:  $R_0 = R_1 = R_2 = 10 \text{ m}\Omega$ ,  $T_1 = 150 \text{ s}$ ,  $T_2 = T_1/2$ . The initial parameters are constant over the whole SOC range and the initial OCV curve is linear  $\text{OCV} = (\text{OCV}_{\text{max}} - \text{OCV}_{\text{min}})\text{SOC} + \text{OCV}_{\text{min}}$ .

The parameters are identified using one week voltage measurement data with no specific charging/discharging scenario. Since the data contains over 6 000 000 data samples, two training sets are extracted<sup>1</sup> - one consisting of approximately 40 hours of data (where two deepest discharging/charging cycles are included) and the other consisting of 80 hours of data (Figs.3.14-3.17). The obtained model is then simulated using the whole 1-week current profile consisting of the training data and the validation data. The accuracy of the model on only the training data and on the whole data set as well as execution

times of the algorithm are summarized in Table 3.2. Both models show high accuracy at the expense of execution times which increased significantly. Also, the shape of the OCV-SOC curve in both cases is less accurate since the hysteresis effect should be expressed, especially at low SOC. An advantage of this method is that no specific experiment scenario needs to be performed. However, the data must contain enough samples from every SOC interval in order to identify the model accurately.

**Table 3.2.** Comparison of the MSE and execution times for the LLS algorithm based on the 2RC model.

No. samples	2RC 0.5e6	2RC 1e6
MSE train	4.5497e-5	1.502e-4
MSE all	3.708e-4	2.0266e-4
$t_{ex}$	1.4011e4 s $\approx$ 3.89 h	2.88e4 s $\approx$ 8 h

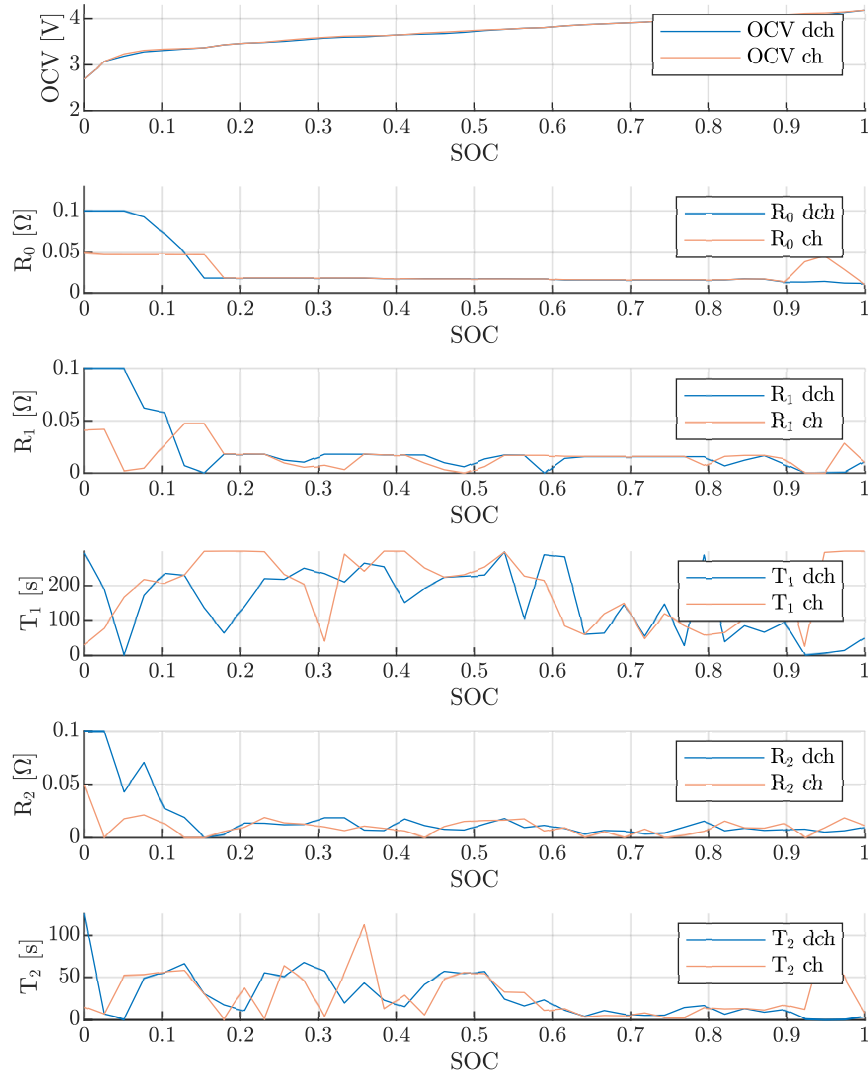


**Figure 3.14.** Parameters of the battery 2RC model dependent on the SOC, based on the constrained LS optimization problem.

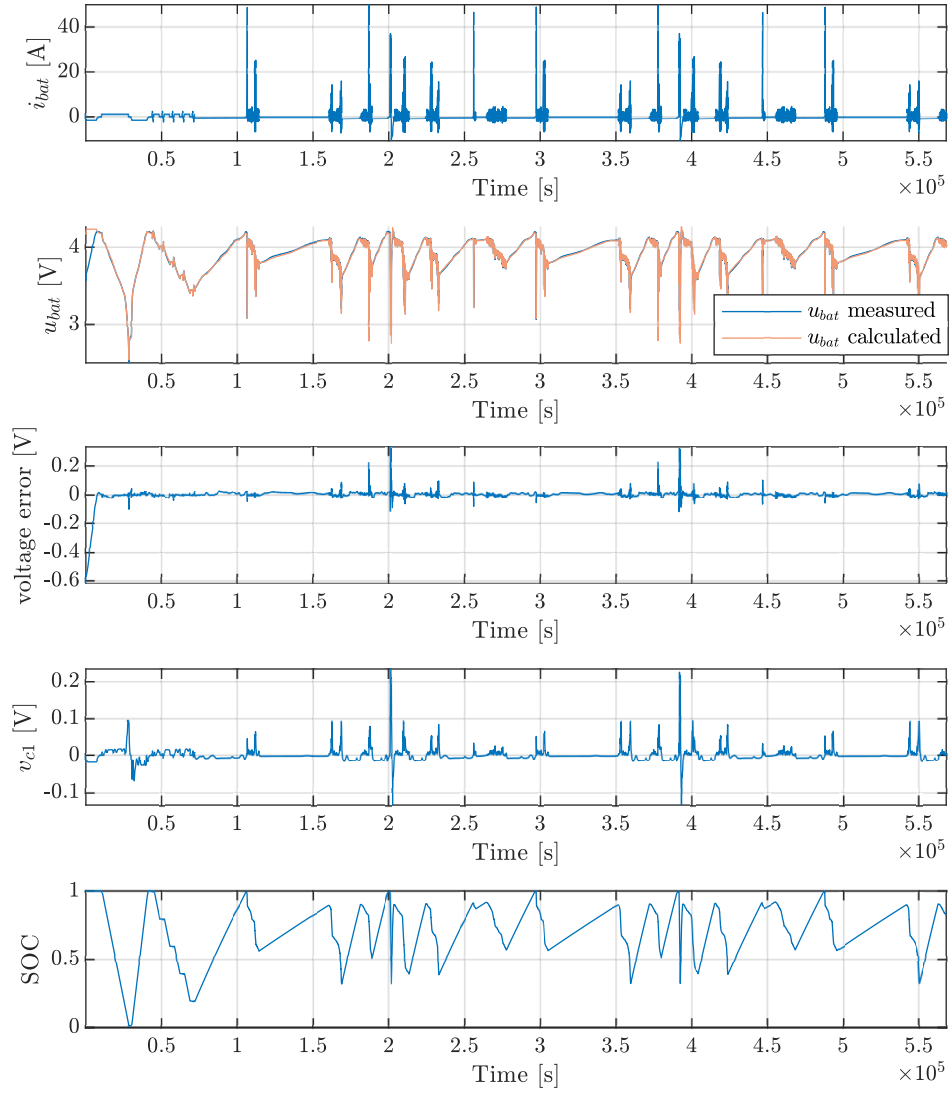


**Figure 3.15.** Simulation of the identified 2RC model, based on the constrained LS optimization problem<sup>1</sup>.

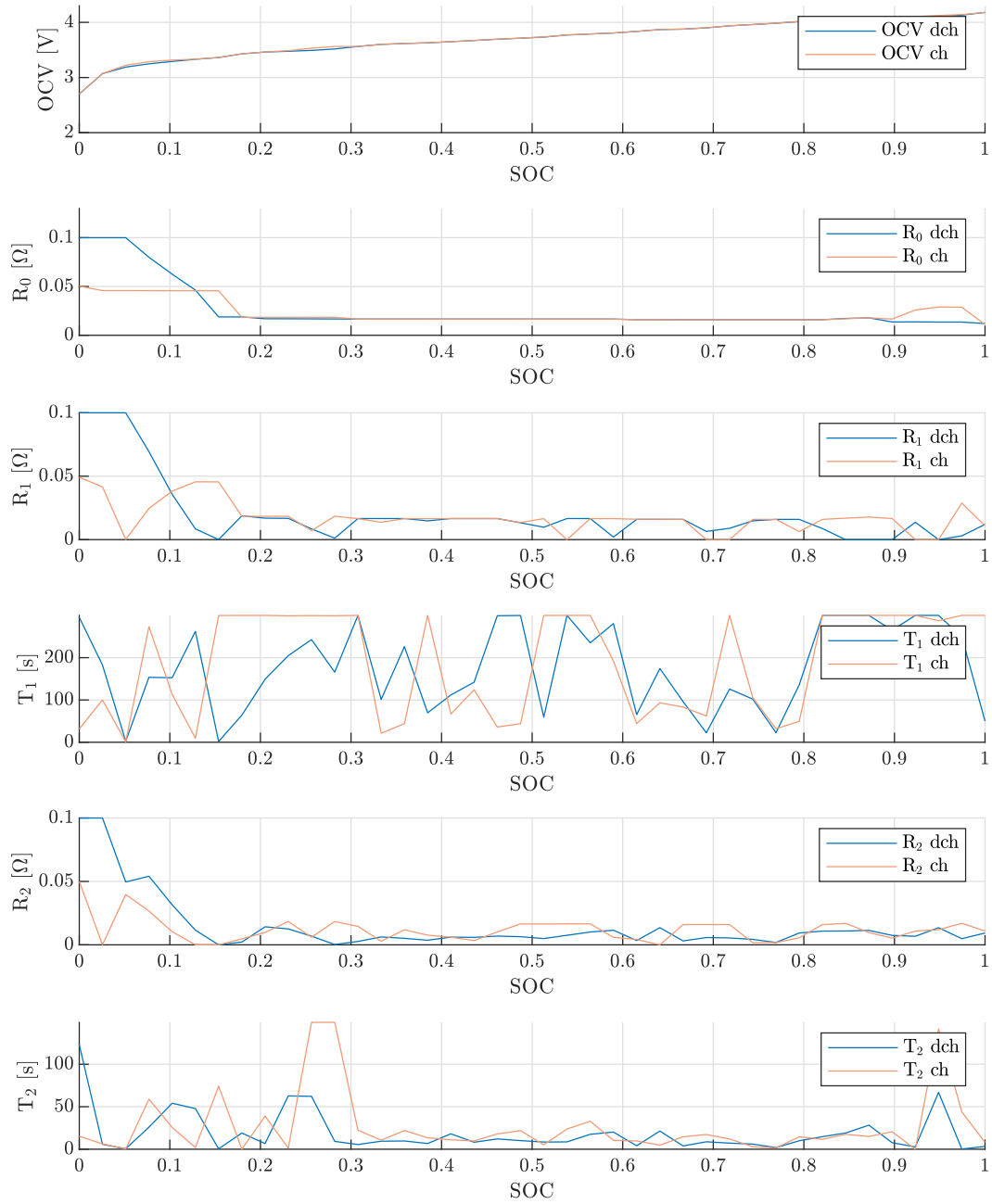


**Figure 3.16.** Parameters of the battery 2RC model dependent on the SOC, based on the constrained LS optimization problem and a bigger training dataset.

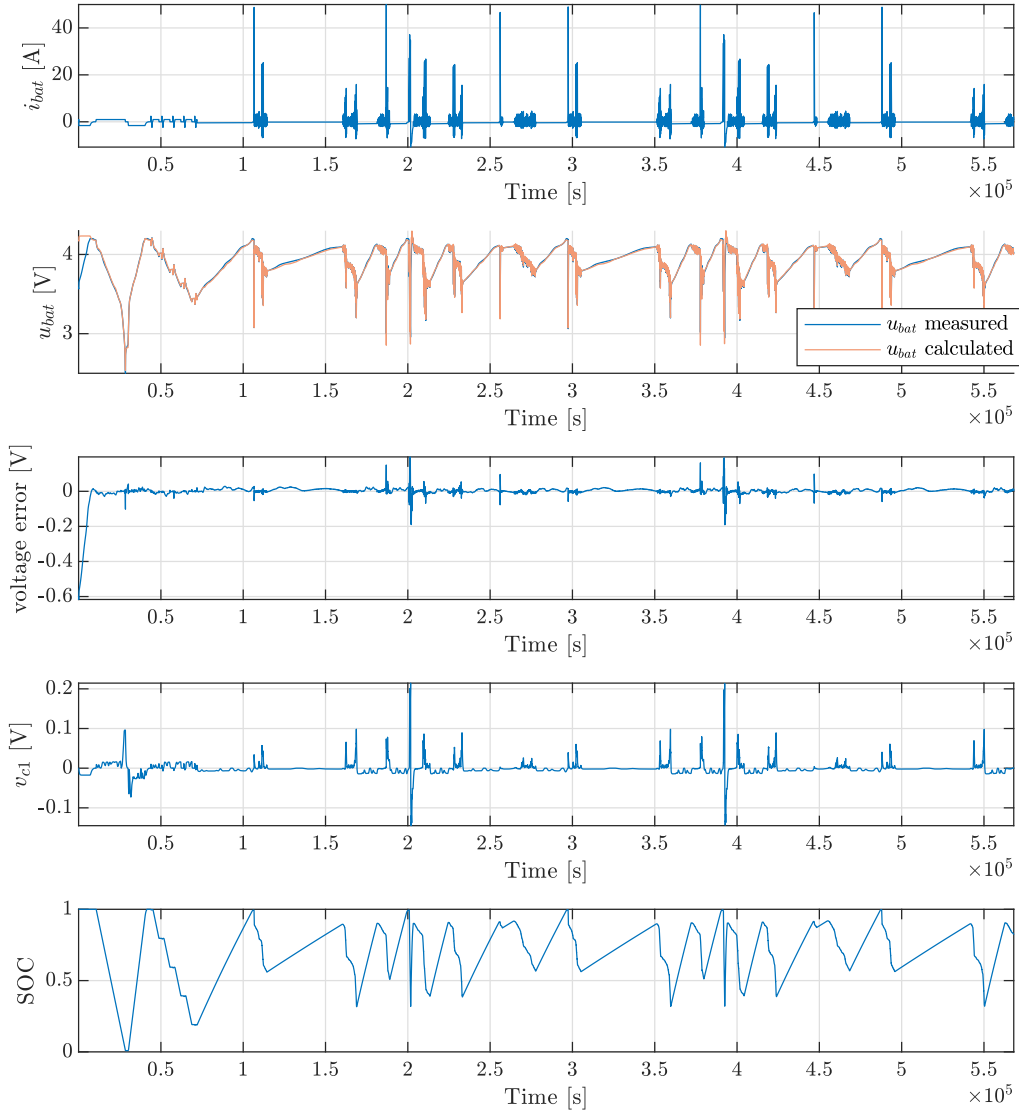


**Figure 3.17.** Simulation of the identified 2RC battery model, based on the constrained LS optimization problem and a bigger training dataset<sup>1</sup>.

### 3.3.1 Constrained least-square parameter identification with a known OCV curve

The results shown in Fig.3.17 show high accuracy, however we observe that the parameters (except the internal resistance) do not show a falling or rising trend with respect to SOC. Also, the charging and discharging OCV curves should be noticeably different at lower SOC, which is not obtained with this optimization procedure. In order to obtain more realistic results, some adjustments were made. First, the OCV curve is determined

separately, using measurements while charging and discharging with a small current, thus ensuring the approximation  $u_{\text{bat}} \approx \text{OCV}$  (Fig.3.18). Second, the parameters are expected to have a convex-like shape which is obtained by adding additional constraints. In order to ensure the desired shape the second derivation of the parameters as functions of SOC is constrained to non-negative values:

$$f(x) = k_2x^2 + k_1x + k_0 \Rightarrow \frac{\partial^2 f(x)}{\partial x^2} = 2k_2 \Rightarrow -k_2 \leq 0. \quad (3.32)$$

The coefficient  $k_2$  can be expressed for each interval using three adjacent parameter values:

$$-\frac{1}{\Delta\text{SOC}(k)}R_0(k) + \left(\frac{1}{\Delta\text{SOC}(k)} + \frac{1}{\Delta\text{SOC}(k+1)}\right)R_0(k+1) - \frac{1}{\Delta\text{SOC}(k+2)}R_0(k+2) \leq 0, \quad (3.33)$$

$$-\frac{1}{\Delta\text{SOC}(k)}R_1(k) + \left(\frac{1}{\Delta\text{SOC}(k)} + \frac{1}{\Delta\text{SOC}(k+1)}\right)R_1(k+1) - \frac{1}{\Delta\text{SOC}(k+2)}R_1(k+2) \leq 0, \quad (3.34)$$

$$-\frac{1}{\Delta\text{SOC}(k)}T_1(k) + \left(\frac{1}{\Delta\text{SOC}(k)} + \frac{1}{\Delta\text{SOC}(k+1)}\right)T_1(k+1) - \frac{1}{\Delta\text{SOC}(k+2)}T_1(k+2) \leq 0, \quad (3.35)$$

$$-\frac{1}{\Delta\text{SOC}(k)}R_2(k) + \left(\frac{1}{\Delta\text{SOC}(k)} + \frac{1}{\Delta\text{SOC}(k+1)}\right)R_2(k+1) - \frac{1}{\Delta\text{SOC}(k+2)}R_2(k+2) \leq 0, \quad (3.36)$$

$$-\frac{1}{\Delta\text{SOC}(k)}T_2(k) + \left(\frac{1}{\Delta\text{SOC}(k)} + \frac{1}{\Delta\text{SOC}(k+1)}\right)T_2(k+1) - \frac{1}{\Delta\text{SOC}(k+2)}T_2(k+2) \leq 0, \quad (3.37)$$

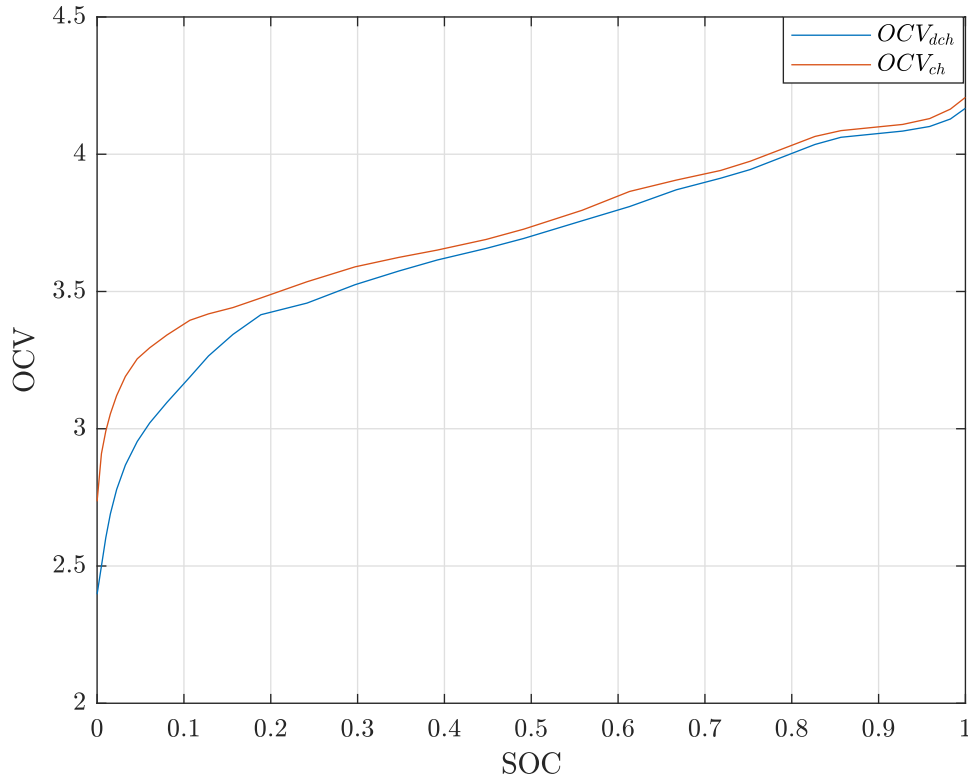


**Figure 3.18.** OCV-SOC curves for the 4.8 Ah battery.

where  $k = 1, \dots, n-2$ . The identification is performed on 1 week measurement data obtained with high current charging/discharging profiles<sup>1</sup>. The identification is performed

for different number of intervals and the model accuracy comparison is summarized in Table 3.3 and depicted in Fig. 3.19. The accuracy of the model increases until 20 intervals. After that, the accuracy does not improve significantly with additional intervals resulting in the choice of the 20 SOC interval model as the best solution.

**Table 3.3.** Comparison of the MSE and execution times for the LLS algorithm based on the 2RC circuit model with different number of SOC intervals.

No. intervals	12	16	20	24	28
MSE all	$3.104 \cdot 10^{-4}$	$3.005 \cdot 10^{-4}$	$2.957 \cdot 10^{-4}$	$2.980 \cdot 10^{-4}$	$2.982 \cdot 10^{-4}$
$t_{ex}$	7.96	11.52	17.06	19.28	23.77

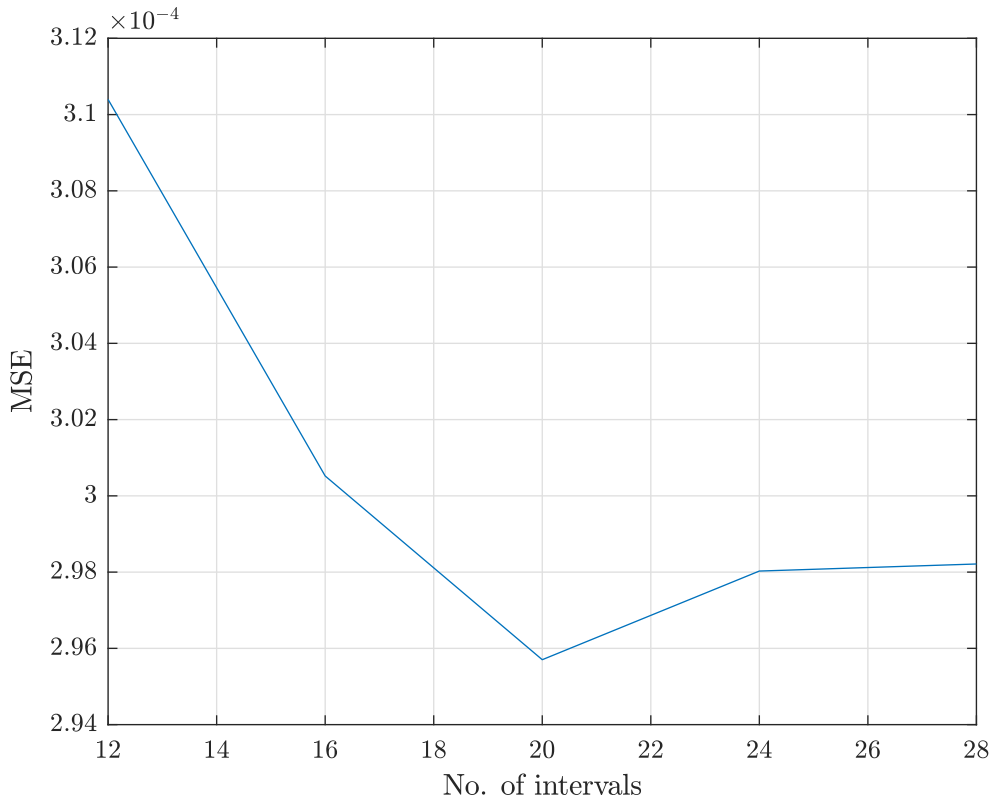


**Figure 3.19.** Comparison of MSE and execution times for different SOC intervals.

In Figs. 3.20 and 3.21 the obtained model parameters, for 20 SOC intervals, and the system simulation are shown. We observe that the ohmic resistances have much higher values at low SOC, while they are mostly flat in the middle range. The time constants, however, show a higher dependency on the SOC, ranging from 300 s to around 20 s (fast response) and from 150 s to around 1 s (slower time constant). The results show expected results, respecting the second derivation constraint, and are considered the closest to the expected real parameter behavior. Figure 3.21 shows a comparison of the measured voltage, training and validation data, and the data obtained with the obtained battery model. The voltage error is shown in the third subplot. The error noticeably increases in

two time intervals. When comparing these time intervals with the SOC values shown in the last plot, it is observed that they coincide with lower SOC values. This is expected since there is only one deep discharge in the training data. The accuracy of the model at lower SOC values is affected by the lack of training data leading to the conclusion that the data for the identification should contain a more uniform charging/discharging pattern.

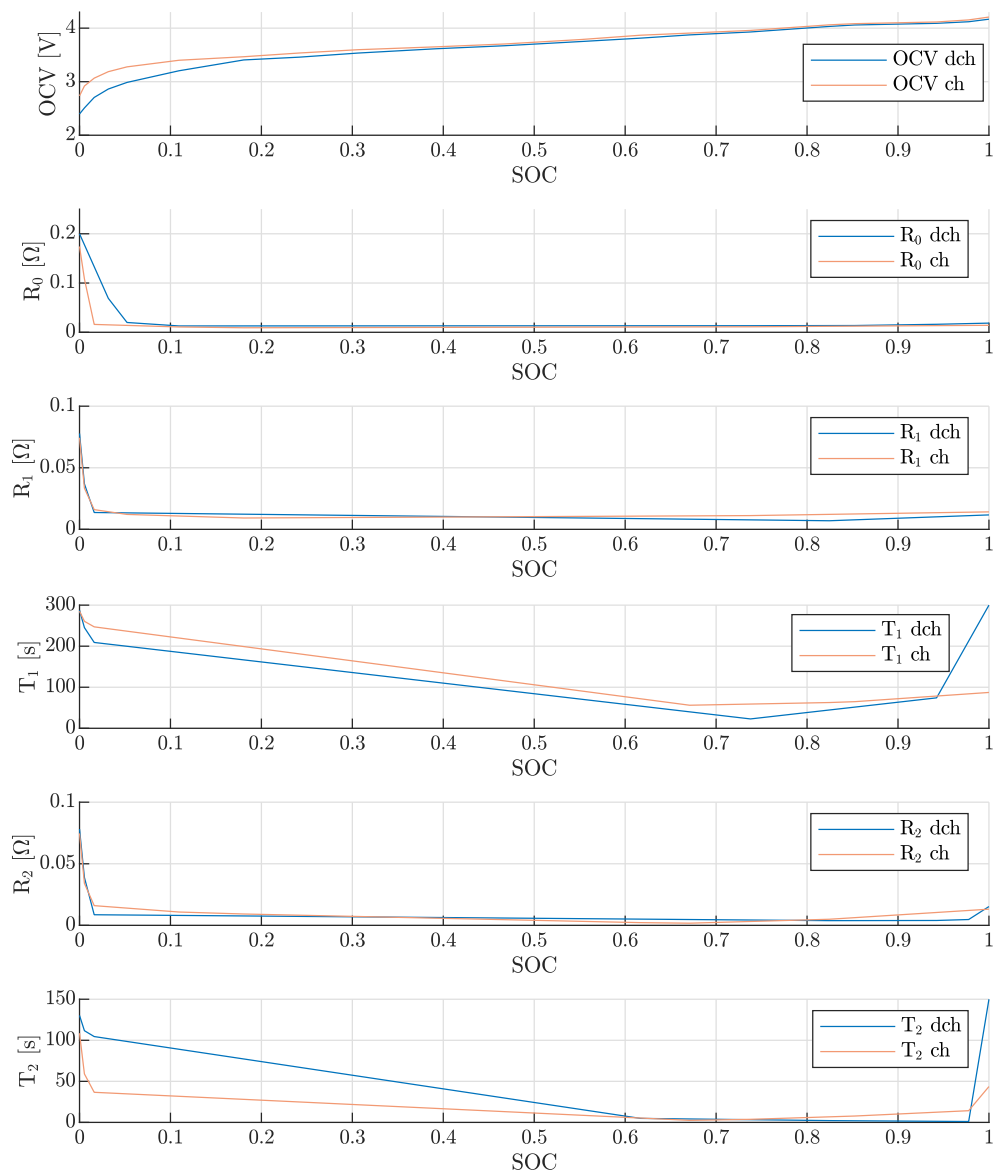


**Figure 3.20.** Obtained battery 2RC model parameters for 20 SOC intervals.



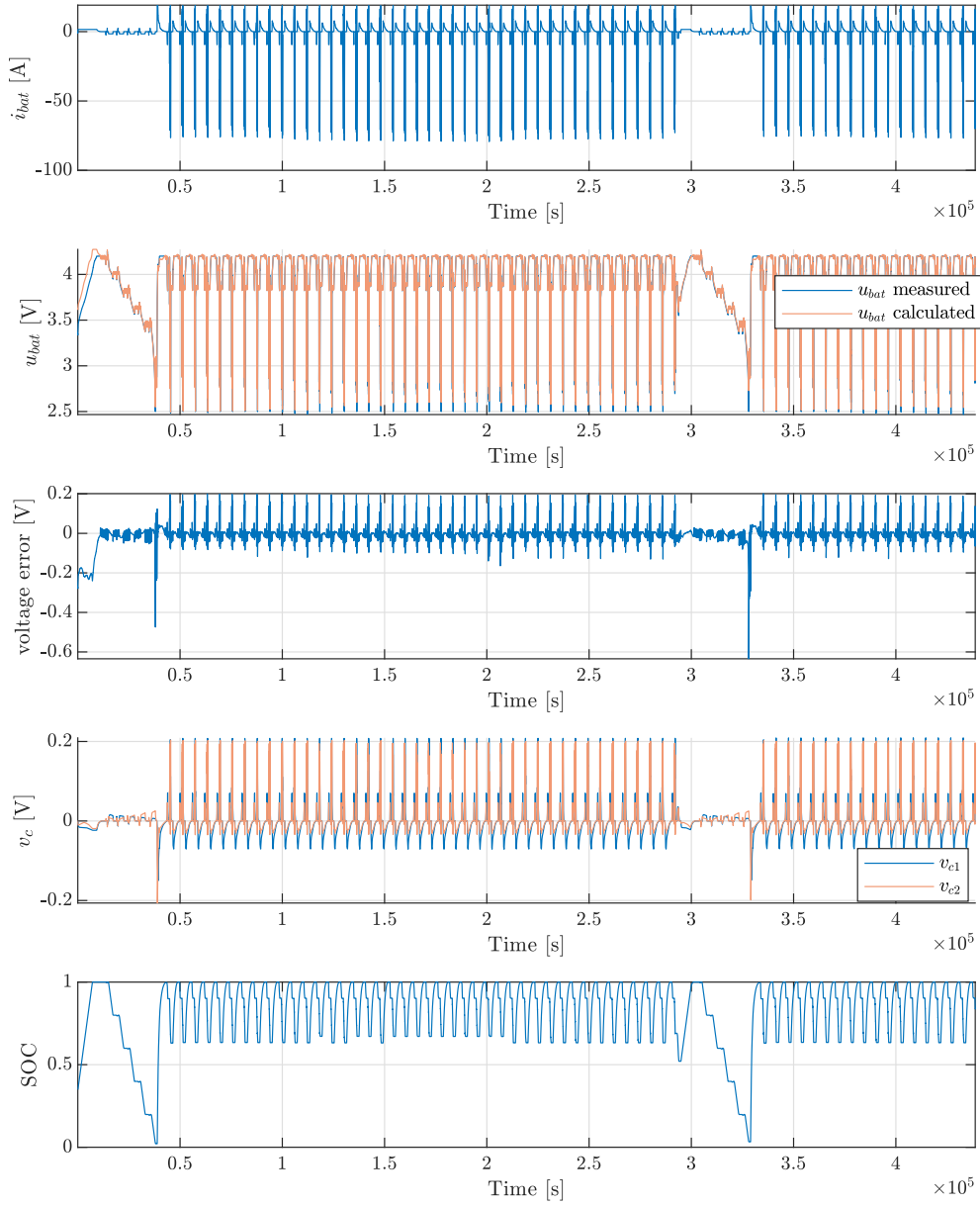


**Figure 3.21.** Comparison of simulated voltage response with the measured voltage, training and validation data<sup>1</sup>.

The first presented identification method is the simplest of the three and with the shortest execution times. Its accuracy greatly depends on the number of SOC intervals resulting in a more complex model. Also, the inability to obtain a higher order model affects the overall accuracy. However, this algorithm is suitable for online identification because there is an explicit solution. The second method successfully identifies the second order parameters and the OCV-SOC curve, but the resulting parameter variations do not correspond to expected trends. This is fixed by adding additional constraints, however

this does not solve the problem with the OCV curve. Finally, identification of parameters with a known OCV curve, which is obtained from separate measurements and then used in the LS optimization problem, is presented. The results obtained with this method (Fig. 3.20) are the closest to the expected and used in the battery model.

### 3.4 Variable battery efficiency model

Since the identification is performed on a 4.8 Ah battery cell, in order to obtain the capacity and voltage levels appropriate for the microgrid topology, the final model is scaled by connecting the cell in several parallel and series connections. Battery parallel connection, shown in Fig.3.22 increases battery capacity while conserving the voltage levels:

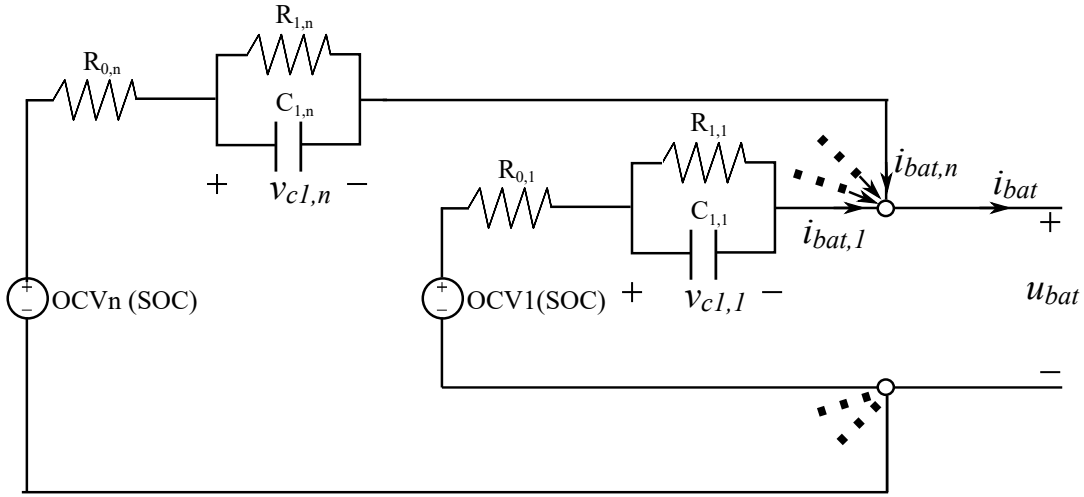


**Figure 3.22.** Battery cells parallel connection.

$$i_{\text{bat}} = i_{\text{bat},1} + \dots + i_{\text{bat},n} = \sum_{i=1}^n i_{\text{bat},i}, \quad (3.38)$$

$$u_{\text{bat}} = u_{\text{bat},1} = \dots = u_{\text{bat},n} \quad (3.39)$$

$$\begin{aligned} u_{\text{bat}} &= \text{OCV}_1 - R_{0,1}i_{\text{bat},1} - v_{c1,1} \\ &\vdots \\ &= \text{OCV}_n - R_{0,n}i_{\text{bat},n} - v_{c1,n} \end{aligned} \quad (3.40)$$

$$u_{\text{bat}} = \frac{\sum_{i=1}^n \text{OCV}_i}{n} - \frac{R_0}{n} \sum_{i=1}^n i_{\text{bat},i} - \frac{\sum_{i=1}^n v_{c1,i}}{n}. \quad (3.41)$$

In Eq (3.41) we assumed  $R_0 = R_{0,1} = \dots = R_{0,n}$  because cells of the same type are being connected. Also,  $\sum_{i=1}^n \text{OCV}_i/n = \text{OCV}_i$ , again, under assumption that the cells have the same OCV-SOC curves. The total internal resistance of the module can be deduced from

(3.41) as:

$$R_{0,tot} = \frac{R_0}{n}, \quad (3.42)$$

and the remaining parameters are extracted from the RC circuit voltage expressions. The RC circuit voltage of the module is equal to:

$$\frac{\sum_{i=1}^n \dot{v}_{c1,i}}{n} = \dot{v}_{c,tot} = -\frac{1}{T_{1,tot}} v_{c,tot} + \frac{R_{1,tot}}{T_{1,tot}} i_{bat}. \quad (3.43)$$

The left side of Eq. (3.43) is substituted with:

$$\begin{aligned} \frac{\sum_{i=1}^n \dot{v}_{c1,i}}{n} &= \frac{1}{n} (\dot{v}_{c1,1} + \dots + \dot{v}_{c1,n}) = \\ &= -\frac{1}{n} \left( \frac{1}{T_1} v_{c1,1} + \dots + \frac{1}{T_1} v_{c1,n} \right) + -\frac{1}{n} \left( \frac{R_1}{T_1} i_{bat,1} + \dots + \frac{R_1}{T_1} i_{bat,n} \right) = \\ &= -\frac{1}{T_1} \underbrace{\frac{\sum_{i=1}^n v_{c1,i}}{n}}_{v_{c,tot}} + \frac{R_1}{n} \frac{1}{T_1} \underbrace{\sum_{i=1}^n i_{bat,i}}_{i_{bat}}. \end{aligned} \quad (3.44)$$

Then, by combining (3.44) with (3.43) we obtain:

$$T_{1,tot} = T_1, \quad R_{1,tot} = \frac{R_1}{n}. \quad (3.45)$$

The total capacity of the parallel connection is calculated from:

$$\text{SOC}_{tot} = \text{SOC}_1 = \dots = \text{SOC}_n, \quad (3.46)$$

$$\text{SOC}_i = -\frac{1}{C_{cap}} i_{bat,i}, \quad (3.47)$$

$$\sum_{i=1}^n \text{SOC}_i = -\frac{1}{C_{cap}} \sum_{i=1}^n i_{bat,i} \rightarrow \text{SOC}_{tot} = -\frac{1}{nC_{cap}} i_{bat}. \quad (3.48)$$

The total capacity is then  $C_{cap,tot} = nC_{cap}$  and  $n$  is the number of parallel connections needed to obtain the desired capacity. The series connection of battery cells is depicted

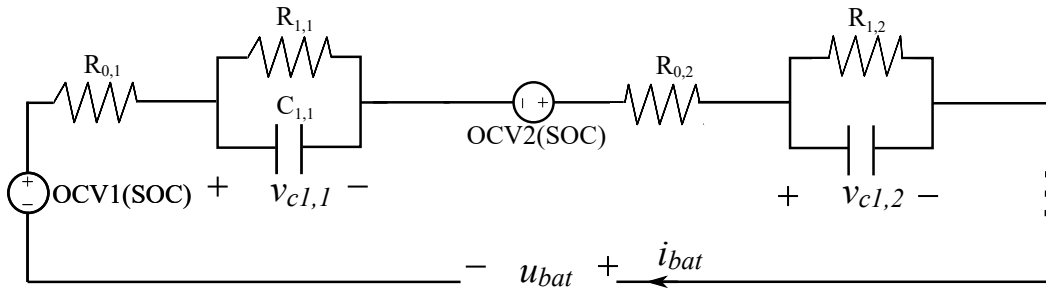


**Figure 3.23.** Battery cells series connection.

in Fig.3.23. With this connection the terminal voltage is increased while the battery

capacity is not affected:

$$\begin{aligned} u_{\text{bat}} &= OCV_1 + R_{0,1}i_{\text{bat}} + v_{c1,1} + \dots + OCV_n + R_{0,n}i_{\text{bat}} + v_{c1,n} = \\ &= nOCV + nR_0i_{\text{bat}} + \sum_{i=1}^n v_{c1,i}, \end{aligned} \quad (3.49)$$

$$\dot{v}_{c1,\text{tot}} = \sum_{i=1}^n \dot{v}_{c1,i} = -\frac{1}{T_1} \sum_{i=1}^n v_{c1,i} + \frac{R_1}{T_1} ni_{\text{bat}}, \quad (3.50)$$

where it is assumed, as in the parallel connection example, that all cells are equal. From (3.49) and (3.50) the expressions for the scaled parameters are determined:

$$R_{0,\text{tot}} = nR_0, \quad R_{1,\text{tot}} = nR_1, \quad T_{1,\text{tot}} = T_1. \quad (3.51)$$

The combined expressions for series and parallel connections are then:

$$C_{\text{cap,tot}} = n_p C_{\text{cap}}, \quad (3.52)$$

$$OCV_{\text{tot}} = n_s OCV, \quad (3.53)$$

$$R_{0,\text{tot}} = n_s \frac{R_0}{n_p}, \quad (3.54)$$

$$R_{1,\text{tot}} = n_s \frac{R_1}{n_p}, \quad (3.55)$$

$$T_{1,\text{tot}} = T_1, \quad (3.56)$$

where  $n_s$  and  $n_p$  are the number of series and parallel connections. In order to obtain a 100 Ah battery with approximately 12 V terminal voltage, 3 series and 20 parallel connections are necessary and the parameters are scaled using (3.52)-(3.56).

### 3.4.1 Efficiency of the second order ECM

The efficiency of the battery depends on the SOC and on the discharging/charging battery current. The efficiency is calculated with:

$$u_{\text{bat}}(\text{SOC}_i) = OCV(\text{SOC}_i) - (R_0(\text{SOC}_i) + R_1(\text{SOC}_i) + R_2(\text{SOC}_i))i_{\text{bat}}. \quad (3.57)$$

$$\eta_{\text{ch}} = \frac{P_{\text{ch}} - P_{\text{loss}}}{P_{\text{ch}}}, \quad P_{\text{ch}} = u_{\text{bat}}(\text{SOC}_i)i_{\text{bat}}, \quad P_{\text{loss}} = -(R_0(\text{SOC}_i) + R_1(\text{SOC}_i) + R_2(\text{SOC}_i))i_{\text{bat}}^2, \quad (3.58)$$

$$\eta_{\text{dch}} = \frac{P_{\text{dch}} - P_{\text{loss}}}{P_{\text{dch}}}, \quad P_{\text{dch}} = OCV(\text{SOC}_i)i_{\text{bat}}, \quad P_{\text{loss}} = (R_0(\text{SOC}_i) + R_1(\text{SOC}_i) + R_2(\text{SOC}_i))i_{\text{bat}}^2. \quad (3.59)$$

The parameters obtained in Section 3.2 (Fig. 3.20) are scaled and the resulting battery model is depicted in Fig. 3.24.

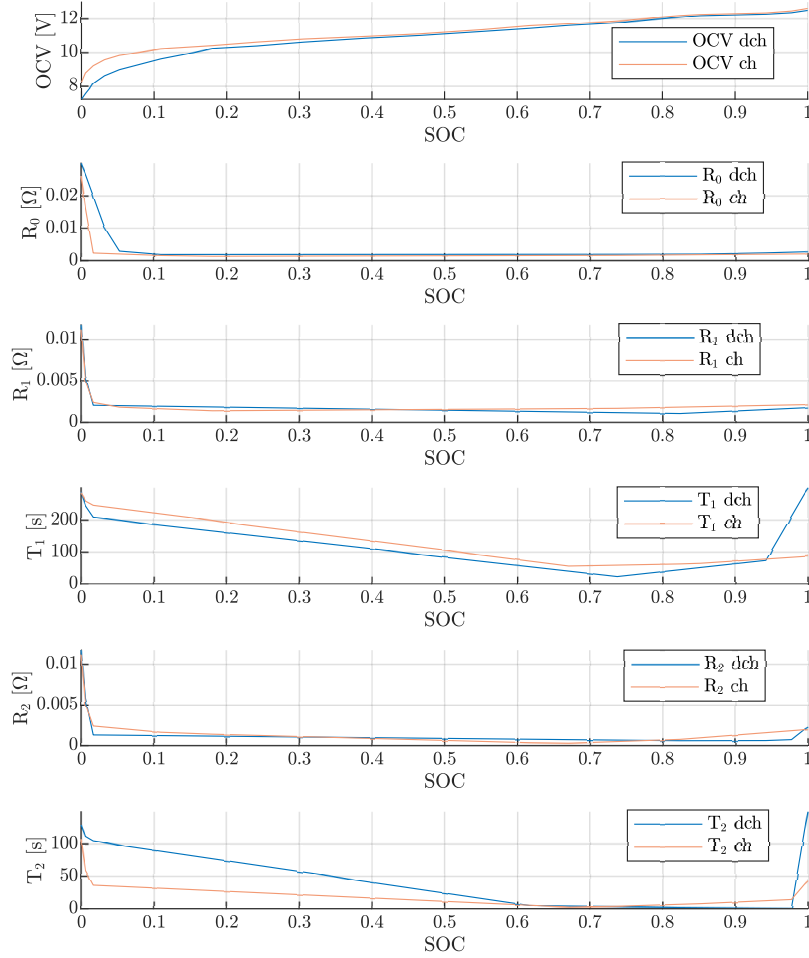


**Figure 3.24.** Scaled parameters of the 2RC battery model.

The efficiency depending on SOC and the charging/discharging power is shown in Fig. 3.25. We can see that for increasing power and decreasing SOC the efficiency has a falling trend. Since the parameters, while discharging, are mostly higher than while charging, especially at low SOC, the discharging efficiency graph is deeper than the charging efficiency graph. The voltage at battery terminals depends on the current and the SOC, therefore a graph of achievable charging and discharging powers for different combinations of currents and corresponding battery voltages is shown in Fig. 3.26. The graph shows that the maximal battery power changes with the battery SOC.

The efficiency curves for a given SOC, over a power span from zero to nominal power, are shown in Fig. 3.27. The discharging efficiency is higher than the charging efficiency for 20% and 90% SOC and vice versa for 50% SOC which is the result of higher charging resistances than discharging, in the first case and higher discharging resistances than the charging, in the second case.

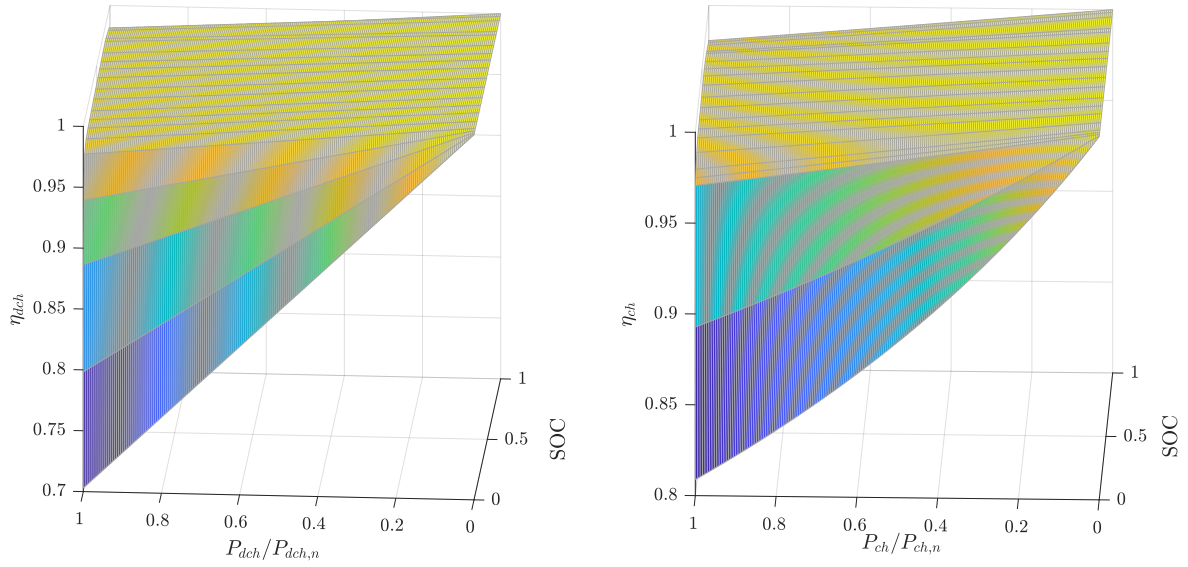


**Figure 3.25.** Discharging and charging efficiencies of the 2RC model, depending on the SOC and the normalized discharging/charging power.

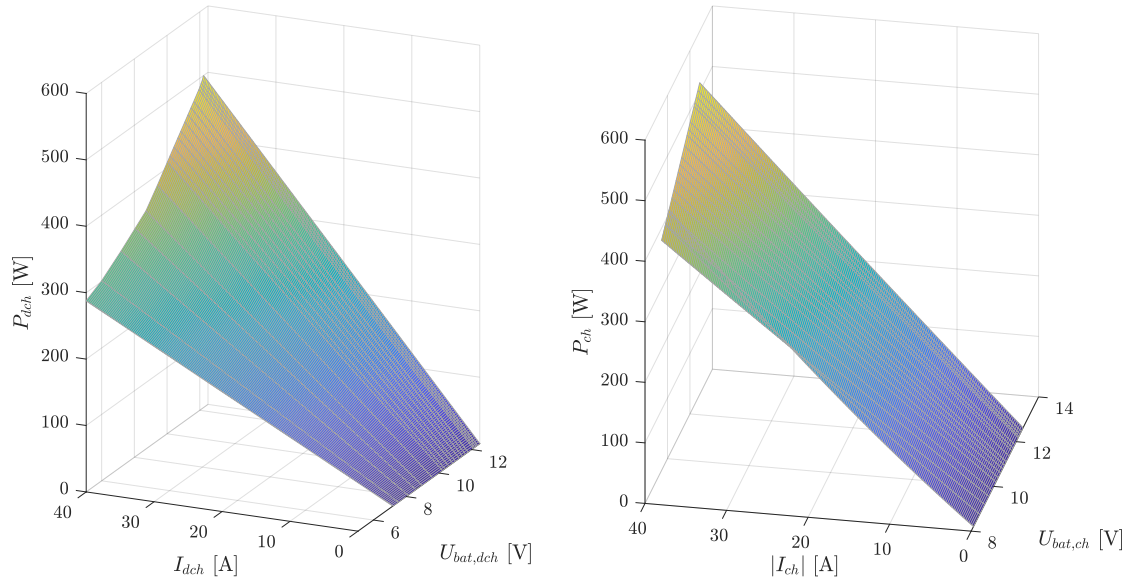


**Figure 3.26.** Discharging and charging powers of the 2RC model, depending on the battery voltage and the discharging/charging current.

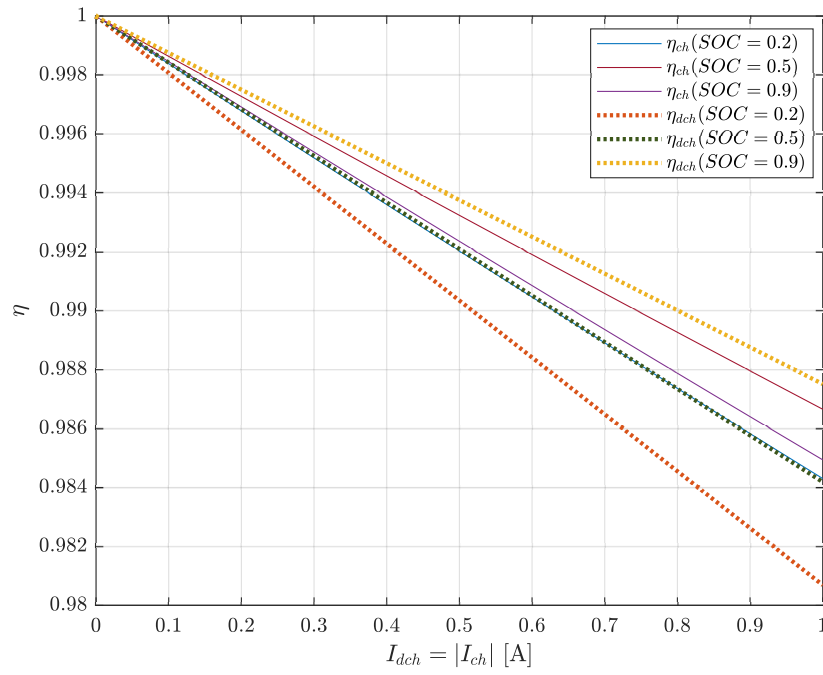


**Figure 3.27.** Discharging and charging efficiencies of the 2RC model for  $SOC=20\%$ ,  $SOC=50\%$  and  $SOC=90\%$ .

## Model predictive control of battery charging and discharging current

The battery storage system consists of a battery and a power converter as depicted in Figure 4.1. The power converter enables connection to the microgrid bus by adjusting its voltage. Depending on the type of the microgrid, the converters are either AC/DC or DC/DC, however they are always bidirectional to enable energy flow in both directions. Additionally, the configurations are divided into single-stage and double-stage conversions. Buck converters are used when the output voltage should be lower than the input voltage, Boost converters are used when the output voltage should be higher than the input voltage.

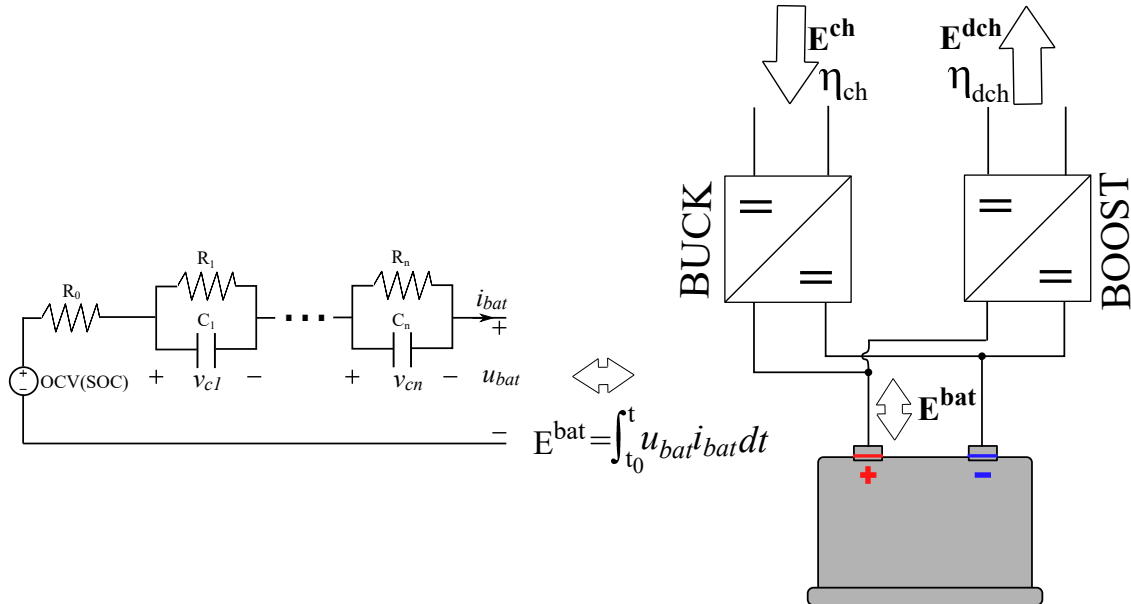


**Figure 4.1.** Battery storage system model and energy flow.

boost converters increase the output voltage. The third type, buck-boost converters, can adjust the output voltage to both higher and lower level than the input voltage [46].



Depending on the battery and microgrid possible voltage values, one of these three types of converters is used. The converter is also the control point of the system because it realizes the control actions demanded from a higher-level controller. And for that reason, it is important to understand how to control the converter and what control input it should receive.

## 4.1 Storage system converter model and efficiency

Modeling of the DC/DC converters includes switched models and averaged models. Averaged models omit high-frequency ripple in the current and voltage waveforms [47,48]. Some converters accept power as the control input however, conventional control mode of the DC/DC converters is voltage control mode [49] whereas current control mode introduces improvements such as inherent current limiting and easier control system design [50,51,52]. Some converters can operate in voltage and current control mode. In voltage control operation different scenarios of microgrid operation in terms of distributed and centralized voltage control configuration are possible which offers flexibility of system configuration and operation [53,54].

In [55], an averaged model of a double-half bridge buck-boost DC-DC converter for microgrid storages is shown. The converter is a bidirectional buck-boost type that consists of two mirrored bidirectional buck topology converters and a common higher voltage DC bus (Fig.4.2). This topology is popular because of its simplicity and superior fault isolation at the expense of an increased component count [46]. The converter from [55] can either control the storage side current or operate as master and control the microgrid voltage. Since both sides are bidirectional, they can operate in buck or boost mode, depending on the current flow. This way, both  $V_1$  and  $V_2$  are flexible and able to ensure the voltage of up to the value  $V_{bc}$ . In this topology,  $V_1$  is considered as a storage-side voltage for

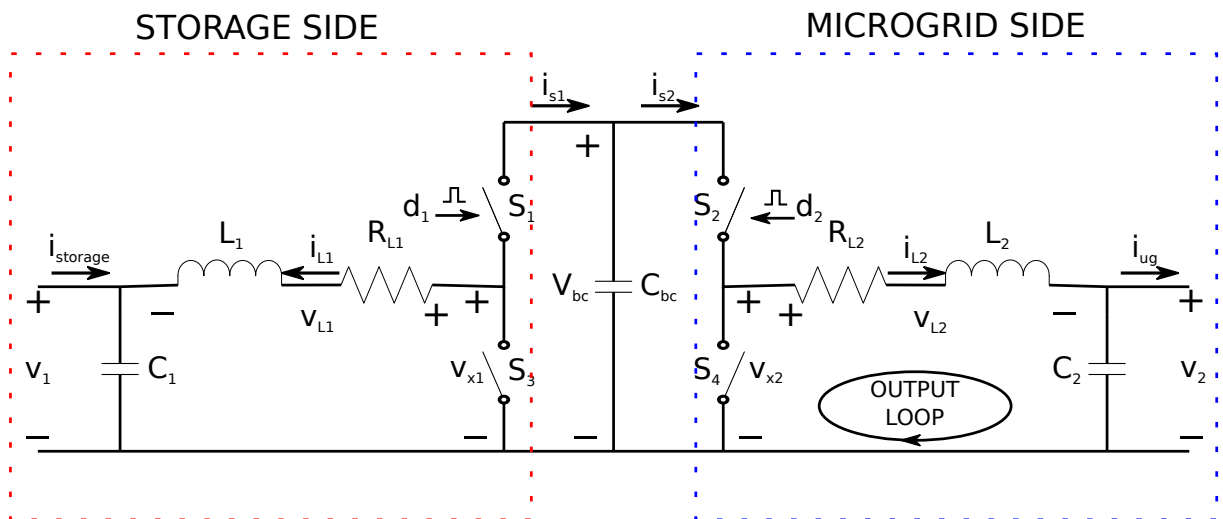


**Figure 4.2.** Bidirectional DC/DC converter topology.

controlling the charge/discharge process of a battery. Voltage  $V_2$  is the microgrid voltage rated value. If the reference current directions of both sides are defined as in Fig.4.2, both the microgrid-side and the storage side are modeled as buck converters. This model thereby offers understanding of the basic converter topology as well.

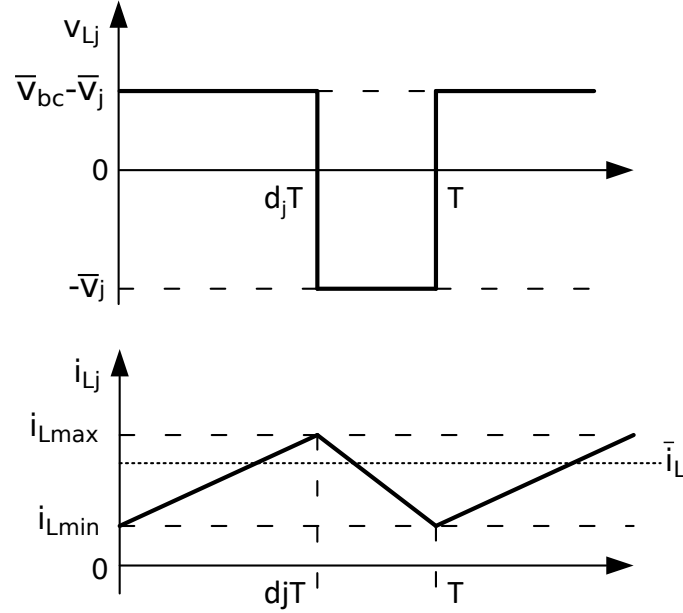


**Figure 4.3.** Inductor voltage and current.

In an ideal buck converter, the inductor voltage and current are represented as in Fig.4.3, where the voltage  $v_{Lj}$  represents the voltage drop on the inductor  $L_j$  and its corresponding resistance  $R_{Lj}$ . By controlling the average value of the inductor current the storage current is set to the requested value. Since the averaged values of the inductor voltage and current depend on the duty cycle the differential equation of the output loop of a buck converter is given by:

$$\bar{v}_{xj} = L_j \frac{d\bar{i}_{Lj}}{dt} + R_{Lj} \bar{i}_{Lj} + \bar{v}_j, \quad j = 1, 2, \quad (4.1)$$

where bar notation represents average values, and the index  $j$  indicates that the same expression is used for both the microgrid and the storage side of the converter (see Fig. 4.2). Since the converter is connected to a microgrid, no load is modelled in the output loop, but it is replaced with a constant voltage value (microgrid voltage). The same approach was used on the storage side. The average switch voltage,  $\bar{v}_{xj}$  is shown in Fig. 4.4 and its value is calculated by integrating over one period:

$$\bar{v}_{xj} = d_j \bar{v}_{bc}. \quad (4.2)$$

The voltage  $\bar{v}_{xj}$  from (4.1) is then substituted by (4.2):

$$\bar{v}_{bc} d_j = L_j \frac{d\bar{i}_{Lj}}{dt} + R_{Lj} \bar{i}_{Lj} + \bar{v}_j, \quad j = 1, 2. \quad (4.3)$$

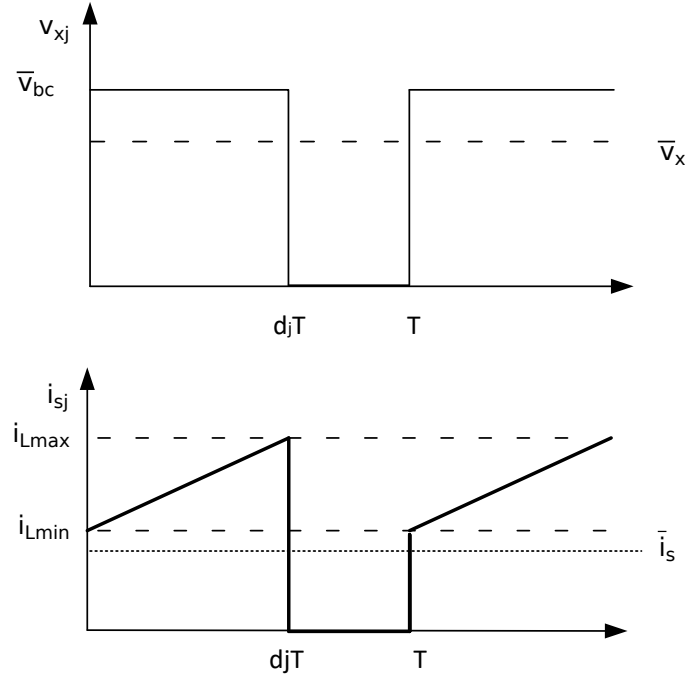


**Figure 4.4.** Switches  $S_3$  or  $S_4$  voltage and switches  $S_1$  or  $S_2$  current over one period.

Both the DC link voltage and the duty cycle are variable, which is denoted by lower-case letters. The equation (4.3) is linearized around the operating point value  $V_{bc0}$  and a transfer function between the duty cycle and the inductor current is:

$$G_{p,j} = \frac{\bar{I}_{Lj}(s)}{D_j(s)} = \frac{V_{bc0}}{sL_j + R_{Lj}}, \quad j = 1, 2. \quad (4.4)$$

where  $\bar{I}_{Lj}$  and  $D_j$  are Laplace transforms of small changes of the mean inductor current and the duty cycle, with respect to their values in the operating point. The transfer function from (4.4) is suitable for design of the current controller.

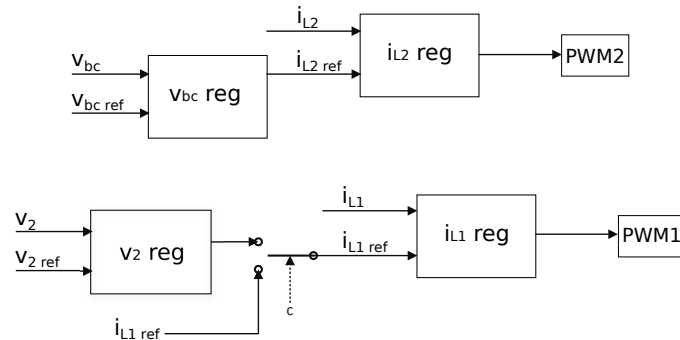


**Figure 4.5.** Converter control scheme. Variable  $c$  denotes the control signal that switches between the current control mode and microgrid voltage control mode.

The DC bus voltage control is then enforced through a cascade control form as an outer control loop (see Fig.4.5). In Fig.4.5, PWM1 denotes the driving block for generating

pulse width modulation (PWM) switching signals for switches  $S_1$  and  $S_3$ , while PWM2 generates signals for switches  $S_2$  and  $S_4$ . Signals with index 'ref' denote reference values for controllers of the respective variables. Following from this, a relation that connects the inductor current with DC bus voltage is required. The DC bus voltage dynamics is given below:

$$C_{bc} \frac{d\bar{v}_{bc}}{dt} = \bar{i}_{s1} - \bar{i}_{s2}. \quad (4.5)$$

The average switch current is shown in Fig.4.4 and equals to:

$$\bar{i}_{sj} = d_j \bar{i}_{Lj}, \quad j = 1, 2. \quad (4.6)$$

By substituting the currents in (4.5), a nonlinear model is obtained:

$$C_{bc} \frac{d\bar{v}_{bc}}{dt} = -d_1 \bar{i}_{L1} - d_2 \bar{i}_{L2}. \quad (4.7)$$

Negative sign in (4.7) is added to  $\bar{i}_{L1}$  because its reference direction is opposite to the reference direction of the switch current as in Fig.4.2. Since only the grid side inductor current  $\bar{i}_{L2}$  is included in the DC link control, a relation between this current and the DC voltage is derived, after linearization around a steady state duty cycle:

$$G_{p,dc} = \frac{\bar{V}_{bc}(s)}{\bar{I}_{L2}(s)} = -\frac{D_{20}}{sC_{bc}}, \quad (4.8)$$

where  $D_{20}$  is the value of  $d_2$  in the operating point. These equations describe the converter model in current control. The current reference  $\bar{i}_{L1ref}$  from Figure 4.5 is obtained from a battery control algorithm.

The model for the microgrid voltage control operation is of lesser importance for this work, but it is also derived in [55].

## 4.2 Battery charging and discharging approaches

Battery charging control approaches are divided into model-free and model-based approaches. The charging profiles of model-free strategies are predefined using heuristics and empirical knowledge. These models are easy to implement but are unable to reflect the battery's dynamics. Model-free approaches include constant-current (CC), constant-voltage (CV) and pulse charging. Model-based approaches use physics-based models, mostly different electrochemical and ECMs, state estimators and model-based controllers. These include fuzzy control, multi-objective optimization, linear quadratic control and model predictive control (MPC). MPC is the most popular strategy, however it is mostly applied to linear systems [56], [57]. Model-based approaches are mostly concerned with health-aware charging approaches. An MPC tracking problem is described in [56]. The battery models on which the control algorithms are based are often simplified

and linearized. Nonlinear multi-objective optimizations are described in [58], [31]. The proposed algorithms offer a trade off between battery degradation and charging times. In [59], an explicit-MPC real-time health-aware charging control is described based on the nonlinear double-capacitor model (NDC). The nonlinear problem is simplified by piecewise linear approximation.

In [60], a control algorithm for efficient adherence to energy exchange commands is presented. The authors proposed an algorithm which offers information about the available charging/discharging energies, while respecting the system constraints. The optimization problem is formulated aiming to maximize the residual SOC thus achieving maximal efficiency during demanded energy exchange. In this work, the energy exchange of the battery storage system (BSS) is defined at a higher stage, namely the microgrid energy flow optimization and the BSS control algorithm is in charge of achieving the demanded battery energy. The previously described algorithm offers valuable information about the system states and is therefore a starting point for the control of a variable battery storage system model.

### 4.3 Variable battery storage system model control

In this section, the 2RC model obtained in section 3.3, subsection 3.3.1. of the third chapter, is used. The charging and discharging energies obtained as solutions of the microgrid power flow optimization problem are transferred to the battery side by taking into account the converter efficiency:

$$E_{\text{bat}} = \begin{cases} \eta_{\text{ch}}(E^{\text{ch}})E^{\text{ch}} & \text{if } E^{\text{ch}} \neq 0 \\ \frac{1}{\eta_{\text{dch}}(E^{\text{dch}})}E^{\text{dch}} & \text{if } E^{\text{dch}} \neq 0 \end{cases} \quad (4.9)$$

The converter efficiency is variable and depends on the converter energy. The obtained energy at the battery side of the power converters is the input for the battery storage system control algorithm. The battery energy is defined as:

$$E_{\text{bat}} = \int_{t_0}^t u_{\text{bat}}(\tau) i_{\text{bat}}(\tau) d\tau. \quad (4.10)$$

The BSS control algorithm is in charge of injecting/extracting energy demanded from the microgrid MPC algorithm. In order to charge and discharge the battery in the most efficient way, while respecting the system constraints, the BSS MPC optimization is formulated as in [60]:

$$\max_{\mathbf{I}_{\text{bat}}} = \text{SOC}(N), \quad (4.11)$$

$$s.t. \quad \mathbf{I}_{\text{bat}}^T H \mathbf{I}_{\text{bat}} + x(0)^T F^T \mathbf{I}_{\text{bat}} = E_{\text{bat}}, \quad (4.12)$$

$$I_{\text{bat,max}} \geq I_{\text{bat}}(k) \geq -I_{\text{bat,max}}, \quad k = 0, \dots, N_{\text{bs}} - 1, \quad (4.13)$$

$$U_{\text{bat},\min} \leq U_{\text{bat}}(k) \leq U_{\text{bat},\max}, \quad k = 0, \dots, N_{bs} - 1, \quad (4.14)$$

$$U_{\text{bat},\min} \leq U_{\text{bat}}^-(k) \leq U_{\text{bat},\max}, \quad k = 1, \dots, N_{bs}, \quad (4.15)$$

$$\text{SOC}_{\min} \leq \text{SOC}(k) \leq \text{SOC}_{\max}, \quad k = 1, \dots, N_{bs}, \quad (4.16)$$

where  $N_{bs}$  is the prediction horizon of the BSS control,  $I_{\text{bat},\max}$  is the maximal allowed charging/discharging current,  $U_{\text{bat},\min}, U_{\text{bat},\max}$  are the battery voltage limits and  $\text{SOC}_{\min}, \text{SOC}_{\max}$  are the minimal and maximal allowed SOC. The voltage  $U_{\text{bat}}^-(k)$  is the voltage at time instant  $k$ , before the next current value is applied and is defined as:

$$U_{\text{bat}}^-(k) = \lim_{t \rightarrow kT^-} U_{\text{bat}}(t) = \text{OCV}(k) - V_{c1}(k) - V_{c2}(k) - R_0 I_{\text{bat}}(k). \quad (4.17)$$

The objective of the control algorithm is maximizing SOC at the end of the prediction horizon and can be rewritten as:

$$\max_{\mathbf{I}_{\text{bat}}} \text{SOC}(N) = \text{SOC}(0) + \mathbf{C}_m \mathbf{I}_{\text{bat}}, \quad \mathbf{C}_m = [-T_{bs}/C_{\text{bat}}, \dots, -T_{bs}/C_{\text{bat}}], \quad (4.18)$$

where  $T_{bs}$  is the sample time of the BSS and  $C_{\text{bat}}$  is the battery capacity. Matrices  $H$  and  $F$  from the energy equality constraint (4.12) are obtained from (4.10) by substituting the battery voltage as follows [60]:

$$\dot{x} = \begin{bmatrix} \text{OCV} \\ v_{c1} \\ v_{c2} \end{bmatrix} = \underbrace{\begin{bmatrix} 0 & 0 & 0 \\ 0 & -\frac{1}{R_1 C_1} & 0 \\ 0 & 0 & -\frac{1}{R_2 C_2} \end{bmatrix}}_{\mathbf{A}} \begin{bmatrix} \text{OCV} \\ v_{c1} \\ v_{c2} \end{bmatrix} + \underbrace{\begin{bmatrix} -\frac{k_1}{C_{\text{bat}}} \\ \frac{1}{C_1} \\ \frac{1}{C_2} \end{bmatrix}}_{\mathbf{B}} i_{\text{bat}}, \quad (4.19)$$

$$y = u_{\text{bat}} = \underbrace{\begin{bmatrix} 1 & -1 & -1 \end{bmatrix}}_{\mathbf{C}} \begin{bmatrix} \text{OCV} \\ v_{c1} \\ v_{c2} \end{bmatrix} - \underbrace{R_0}_{\mathbf{D}} i_{\text{bat}}. \quad (4.20)$$

$$x(t) = x(iT_{bs})e^{A(t-iT_{bs})} + \int_{iT_{bs}}^t B e^{A(t-\tau)} i_{\text{bat}}(\tau) d\tau, \quad (4.21)$$

$$\begin{aligned} E_{\text{bat}} &= \int_0^{NT_{bs}} u_{\text{bat}}(t) i_{\text{bat}}(t) dt = \sum_{i=0}^{N-1} \int_{iT_{bs}}^{(i+1)T_{bs}} u_{\text{bat}}(t) i_{\text{bat}}(t) dt = \\ &= \sum_{i=0}^{N-1} \int_{iT_{bs}}^{(i+1)T_{bs}} (Cx(t) + Di_{\text{bat}}(t)) i_{\text{bat}}(t) dt. \end{aligned} \quad (4.22)$$

Then,  $x(t)$  is substituted with (4.21) and we obtain:

$$E_{\text{bat}} = \sum_{i=0}^{N-1} \left( \int_{iT_{bs}}^{(i+1)T_{bs}} Cx(iT_{bs}) e^{A(t-iT_{bs})} i_{\text{bat}}^2(t) dt + \right. \quad (4.23)$$

$$+ \int_{iT_{bs}}^{(i+1)T_{bs}} C \left( \int_{iT_{bs}}^t B e^{A(t-\tau)} i_{bat}(\tau) d\tau \right) i_{bat}(t) dt + \int_{iT_{bs}}^{(i+1)T_{bs}} D i_{bat}^2(t) dt. \quad (4.24)$$

The battery energy equation can be rewritten so its depends only on the initial states and the battery vector:

$$E_{bat} = \sum_{i=0}^{N-1} f_i x(0) i_{bat}(i) + h_i i_{bat}^2(i) + h_{i,j} i_{bat}(i), \quad (4.25)$$

$$f_i = \int_{iT_{bs}}^{(i+1)T_{bs}} C e^{At} dt, \quad (4.26)$$

$$h_i = \int_{iT_{bs}}^{(i+1)T_{bs}} C \left( \int_{iT_{bs}}^t e^{A(t-\tau)} B d\tau + D \right) dt, \quad (4.27)$$

$$h_{i,j} = \int_{iT_{bs}}^{(i+1)T_{bs}} C \left( \int_{jT_{bs}}^{(j+1)T_{bs}} e^{A(t-\tau)} B i_{bat}(j) d\tau \right) dt, \quad j = 0, \dots, i-1. \quad (4.28)$$

$$H = \begin{bmatrix} h_1 & h_{1,0}/2 & h_{2,0}/2 & \cdots & h_{N_{bs}-1,0}/2 \\ h_{1,0}/2 & h_2 & h_{2,1}/2 & \cdots & h_{N_{bs}-1,1}/2 \\ h_{2,0}/2 & h_{2,1}/2 & h_3 & \cdots & h_{N_{bs}-1,2}/2 \\ \vdots & \vdots & \vdots & \ddots & \vdots \\ h_{N_{bs}-1,0}/2 & h_{N_{bs}-1,1}/2 & h_{N_{bs}-1,2}/2 & \cdots & h_{N_{bs}-1} \end{bmatrix}, \quad F = \begin{bmatrix} f_1 \\ f_2 \\ \vdots \\ f_{N_{bs}-1} \end{bmatrix}. \quad (4.29)$$

The algorithm tests if the initial battery state is inside a constrained set based on battery constraints and Lagrange multipliers. If the initial state is within boundaries of this set, minimal and maximal Lagrange energies are computed and compared with the commanded battery energy. The solution of the Lagrange optimization problem with equality constraint can be explicitly calculated, maximizing the objective function i.e. residual SOC. If the commanded energy is not within this energy interval, minimal and maximal attainable energies are calculated using sequential linear program (SLP) and quadratic program (QP). Then an initial solution is calculated and the objective is maximized by iterative sliding along the ellipsoid of the commanded energy. The detailed procedure and algorithm description is described in [60].

The continuous battery model defined with (4.19) and (4.20) is defined with constant battery parameter values. Since the parameters are SOC dependent, their values change over the charging/discharging horizon. The above mentioned algorithm is modified in order to include a variable battery model over the prediction horizon. First, an initial solution is found with the original algorithm and then using the obtained current vector, the SOC values over the horizon are calculated. Then, a set of continuous SOC-dependent state-space matrices is calculated using the corresponding model parameter values. Since the parameters are constant within SOC intervals, additional constraints are added:

$$\text{SOC}_{lb}(k) \leq \text{SOC}(k) \leq \text{SOC}_{ub}(k), \quad k = 1, \dots, N-1, \quad (4.30)$$

where  $k$  is the time instant and subscripts  $lb$  and  $ub$  denote lower and upper bound of the SOC interval. In order to write the system inequality constraints in vector form, the system is written in the discrete form, which is obtained using zero-order-hold discretization:

$$\mathbf{A}_d(\text{SOC}_k) = \begin{bmatrix} 1 & 0 & 0 \\ 0 & e^{\frac{T_{bs}}{T_1(\text{SOC}_k)}} & 0 \\ 0 & 0 & e^{\frac{T_{bs}}{T_2(\text{SOC}_k)}} \end{bmatrix}, \mathbf{B}_d(\text{SOC}_k) = \begin{bmatrix} -\frac{k_1 T_{bs}}{C_{bat}} \\ R_1(\text{SOC}_k)(1 - e^{\frac{T_{bs}}{T_1(\text{SOC}_k)}}) \\ R_2(\text{SOC}_k)(1 - e^{\frac{T_{bs}}{T_2(\text{SOC}_k)}}) \end{bmatrix}, \quad (4.31)$$

$$\mathbf{C}_d = \mathbf{C}, \quad \mathbf{D}_d(\text{SOC}_k) = \mathbf{D}(\text{SOC}_k).$$

The discrete model is then stacked over the prediction horizon:

$$\mathbf{Y} = \mathbf{C}_s \mathbf{A}_{s0} x(0) + (\mathbf{C}_s \mathbf{B}_{s0} + \mathbf{D}_s) \mathbf{I}_{bat}, \quad \mathbf{Y} = [U_{bat}(0), \dots, U_{bat}(N_{bs} - 1)]^T \quad (4.32)$$

$$\mathbf{Y}^- = \mathbf{C}_s \mathbf{A}_s x(0) + (\mathbf{C}_s \mathbf{B}_s + \mathbf{D}_s) \mathbf{I}_{bat}, \quad \mathbf{Y}^- = [U_{bat}(1), \dots, U_{bat}(N_{bs})]^T, \quad (4.33)$$

$$\mathbf{A}_{s0} = \begin{bmatrix} \mathbf{I} \\ \mathbf{A}_d(\text{SOC}_0) \\ \vdots \\ \mathbf{A}_d(\text{SOC}_0) \mathbf{A}_d(\text{SOC}_1) \cdot \dots \cdot \mathbf{A}_d(\text{SOC}_{N-1}) \end{bmatrix}, \quad (4.34)$$

$$\mathbf{B}_{s0} = \begin{bmatrix} \mathbf{0} & \mathbf{0} & \dots & \mathbf{0} \\ \mathbf{B}_d(\text{SOC}_0) & \mathbf{0} & \dots & \mathbf{0} \\ \vdots & \vdots & \ddots & \vdots \\ \mathbf{A}_d(\text{SOC}_1) \mathbf{A}_d(\text{SOC}_2) \cdot \dots \cdot \mathbf{B}_d(\text{SOC}_0) & \mathbf{A}_d(\text{SOC}_2) \cdot \dots \cdot \mathbf{B}_d(\text{SOC}_1) & \dots & \mathbf{0} \end{bmatrix}, \quad (4.35)$$

$$\mathbf{A}_s = \begin{bmatrix} \mathbf{A}_d(\text{SOC}_0) \\ \vdots \\ \vdots \\ \mathbf{A}_d(\text{SOC}_0) \mathbf{A}_d(\text{SOC}_1) \cdot \dots \cdot \mathbf{A}_d(\text{SOC}_N) \end{bmatrix}, \quad (4.36)$$

$$\mathbf{B}_s = \begin{bmatrix} \mathbf{B}_d(\text{SOC}_0) & \mathbf{0} & \dots & \mathbf{0} \\ \mathbf{A}_d(\text{SOC}_1) \mathbf{B}_d(\text{SOC}_0) & \mathbf{B}_d(\text{SOC}_1) & \ddots & \vdots \\ \vdots & \vdots & \ddots & \vdots \\ \mathbf{A}_d(\text{SOC}_1) \mathbf{A}_d(\text{SOC}_2) \cdot \dots \cdot \mathbf{B}_d(\text{SOC}_0) & \mathbf{A}_d(\text{SOC}_2) \cdot \dots \cdot \mathbf{B}_d(\text{SOC}_1) & \dots & \mathbf{B}_d(\text{SOC}_{N-1}) \end{bmatrix}, \quad (4.37)$$



**Algorithm 1** BSS control algorithm with variable model parameters

---

$x(0), SOC(0), E_{\text{bat}}$   
**Solve** MPC Battery optimization (4.11), with  $\mathbf{A}(SOC(0)), \mathbf{B}(SOC(0)), \mathbf{D}(SOC(0))$   
**while** condition  
**Calculate**  $\mathbf{SOC} = \mathbf{C}_m \mathbf{I}_{\text{bat}}$   
**Determine** SOC interval boundaries  $\forall SOC(k)$  and add to the constraints vector.  
**Calculate**  $\mathbf{A}(SOC(k)), \mathbf{B}(SOC(k)), \mathbf{D}(SOC(k)), k = 0, \dots, N - 1$   
**Calculate** (4.39) - (4.44)  
**Solve** MPC Battery optimization (4.11)  
**if**  
 $i \geq i_{\text{max}}$   
**OR**  
 $SOC_{\text{avg},i} - SOC_{\text{avg},i-1} \leq \varepsilon, \quad SOC_{\text{avg},i} = (SOC_i + SOC_{i-1} + SOC_{i-2})/3$   
**break**  
**end if**  
**end while**

---

$$\mathbf{C}_b = \text{diag}(\mathbf{C}_d), \quad \mathbf{D}_b = \text{diag}(\mathbf{D}_d). \quad (4.38)$$

The constraints (4.13) - (4.16) are then defined:

$$\mathbf{A}_u = \begin{bmatrix} \mathbf{I} \\ -\mathbf{I} \end{bmatrix}, \quad \mathbf{B}_u = \begin{bmatrix} \mathbf{I}_{\text{bat,max}} \\ \mathbf{I}_{\text{bat,max}} \end{bmatrix}, \quad \mathbf{A}_u \mathbf{I}_{\text{bat}} \leq \mathbf{B}_u, \quad (4.39)$$

$$\mathbf{A}_y = \begin{bmatrix} -(\mathbf{C}_s \mathbf{B}_{s0} + \mathbf{D}_s) \\ (\mathbf{C}_s \mathbf{B}_{s0} + \mathbf{D}_s) \end{bmatrix}, \quad \mathbf{B}_y = \begin{bmatrix} -\mathbf{U}_{\text{bat,min}} + \mathbf{C}_s \mathbf{A}_{s0} x(0) \\ \mathbf{U}_{\text{bat,max}} - \mathbf{C}_s \mathbf{A}_{s0} x(0) \end{bmatrix}, \quad \mathbf{A}_y \mathbf{I}_{\text{bat}} \leq \mathbf{B}_y, \quad (4.40)$$

$$\mathbf{A}_y^- = \begin{bmatrix} -(\mathbf{C}_s \mathbf{B}_s + \mathbf{D}_s) \\ (\mathbf{C}_s \mathbf{B}_s + \mathbf{D}_s) \end{bmatrix}, \quad \mathbf{B}_y^- = \begin{bmatrix} -\mathbf{U}_{\text{bat,min}} + \mathbf{C}_s \mathbf{A}_s x(0) \\ \mathbf{U}_{\text{bat,max}} - \mathbf{C}_s \mathbf{A}_s x(0) \end{bmatrix}, \quad \mathbf{A}_y^- \mathbf{I}_{\text{bat}} \leq \mathbf{B}_y^-, \quad (4.41)$$

$$\mathbf{C}_{\text{soc}} = \begin{bmatrix} -T_{\text{bs}}/C_{\text{bat}} & \mathbf{0} & \cdots & \mathbf{0} \\ -T_{\text{bs}}/C_{\text{bat}} & -T_{\text{bs}}/C_{\text{bat}} & \cdots & \mathbf{0} \\ \vdots & \vdots & \ddots & \vdots \\ -T_{\text{bs}}/C_{\text{bat}} & \cdots & \cdots & -T_{\text{bs}}/C_{\text{bat}} \end{bmatrix}, \quad (4.42)$$

$$\mathbf{A}_{\text{soc}} = \begin{bmatrix} -\mathbf{C}_{\text{soc}} \\ \mathbf{C}_{\text{soc}} \end{bmatrix}, \quad \mathbf{B}_{\text{soc}} = \begin{bmatrix} -\mathbf{SOC}_{\text{min}} + \mathbf{SOC}(0) \\ \mathbf{SOC}_{\text{max}} - \mathbf{SOC}(0) \end{bmatrix}, \quad \mathbf{A}_{\text{soc}} \mathbf{I}_{\text{bat}} \leq \mathbf{B}_{\text{soc}}. \quad (4.43)$$

$$\mathbf{B}_{\Delta \text{soc}} = \begin{bmatrix} -\mathbf{SOC}_{\text{lb}} + \mathbf{SOC}(0) \\ \mathbf{SOC}_{\text{ub}} - \mathbf{SOC}(0) \end{bmatrix}, \quad \mathbf{A}_{\text{soc}} \mathbf{I}_{\text{bat}} \leq \mathbf{B}_{\Delta \text{soc}}. \quad (4.44)$$

The pseudocode of the proposed changes to the original control algorithm are described in Algorithm1. The initial state space matrices are calculated using the current SOC. After obtaining the initial solution and calculating the SOC values over the horizon, the problem formulation is repeated using the variable battery model. Then, the optimization

problem is iteratively solved as long as the SOC values over the horizon change intervals and the residual SOC improves. After convergence is detected, the algorithm ends.

### 4.3.1 Open-loop simulation of a variable BSS control

The proposed algorithm is implemented in MATLAB and two scenarios are simulated. The scaled parameters from subsection 3.3.1. are used for the problem formulation. The BSS sampling time is set to 1 min and the horizon length is  $N = 10$ . The battery capacity is, for the algorithm verification, scaled to 50 Ah in order to achieve more SOC interval changes over the horizon. In both scenarios, three cases are observed:

- **Case 1:** Constant model over the horizon, with model parameters around the  $\text{SOC} \approx 0.5$
- **Case 2:** Constant model over the horizon, with model parameters around the  $\text{SOC} \approx \text{SOC}(0)$
- **Case 3:** Variable model over the horizon, using the procedure described in Algorithm1

The SOC interval for the first case is chosen because the parameter curves are mostly flat in the middle SOC ranges, resulting in smaller model errors for a broad range of SOC. In the first scenario, the battery is charged for 10 minutes from 20%. The charging energy  $E_{\text{bat}} = -80$  Wh is chosen to be high, however still from the Lagrange interval. The results of all three simulation cases are shown in Fig.4.6. Comparing the results of the constant parameter models (blue dotted and green dashed lines), the improvement of the residual SOC is evident, showing that just by pairing the model with the initial state, better results are obtained. The variable model and the constant model paired with the initial state show similar SOC at the end of the simulation horizon. Another indicator of the algorithm performance is the actual amount of charging energy. Table4.1 compares the charging energies and the residual SOC for this scenario. Comparing the energies we observe that in the first case the battery is slightly overcharged and in the second case slightly undercharged which is expected since the battery resistances are in the range of  $\text{m}\Omega$ .

**Table 4.1.** Comparison of the achieved energies and residual SOC, in a 10 min charging period with  $\text{SOC}(0) = 0.2$  and  $E_{\text{bat}} = -80$  Wh.

	Case 1	Case 2	Case 3
$\text{SOC}(N)$	0.3441	0.4085	0.4095
$E_{\text{ch}}$ [Wh]	-80.53	-79.8	-80

In the second scenario, a battery is discharged for 10 min, from  $(0) = 0.9$  with  $E_{\text{bat}} = 87$  Wh and the results are shown in Table4.2 and Fig.4.7. Again, an evident improvement

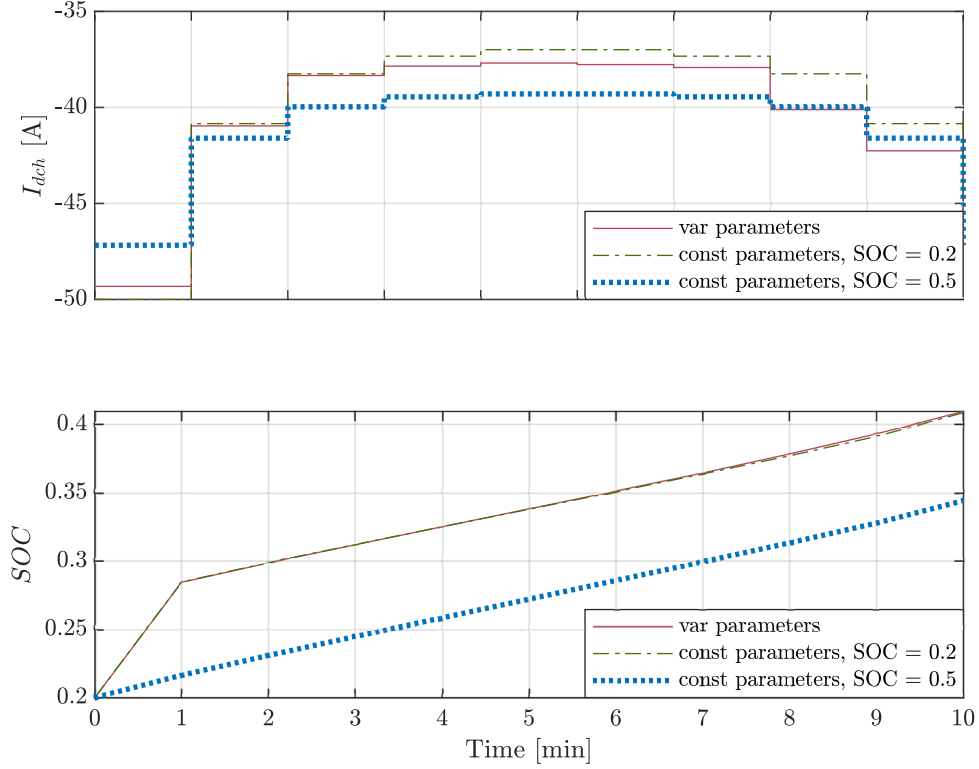


**Figure 4.6.** Simulation of a 10 min charging period with  $SOC(0) = 0.2$  and  $E_{bat} = -80$  Wh.

in results is achieved by pairing the model with the initial SOC. The resulting discharging energies are again higher or lower than the requested energy when a constant model is used. In this scenario, the residual SOC is higher with the model, which is constant around the initial state, than with the variable model. However, the total energy discharged with this solution is lower than the requested energy, thus contributing to the obtained result.

**Table 4.2.** Comparison of the achieved energies and residual SOC, in a 10 min discharging period with  $SOC(0) = 0.9$  and  $E_{bat} = 87$  Wh.

	Case 1	Case 2	Case 3
SOC(N)	0.7185	0.7342	0.7278
$E_{dch}$ [Wh]	90.77	84.21	87

The results of the two scenarios show improvements in the control algorithm by adding the variable battery model to the problem formulation. The improvements are present even with a constant model over the horizon, with parameters corresponding to the initial state.

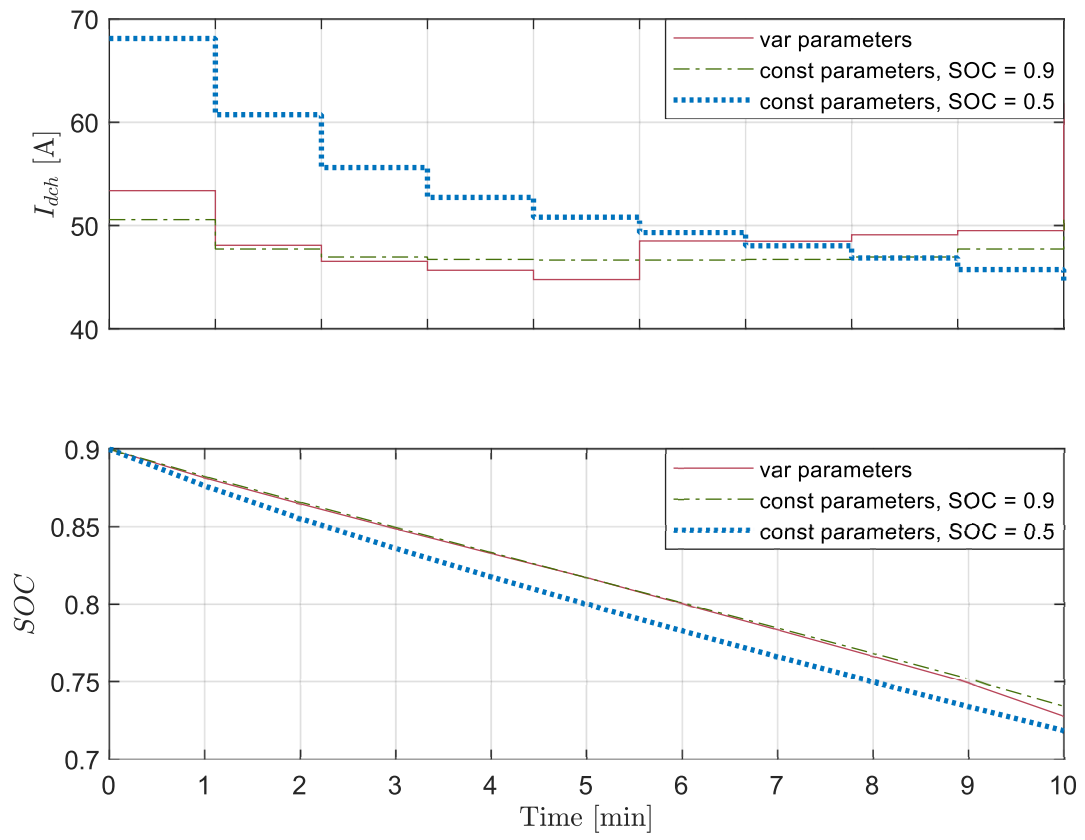


**Figure 4.7.** Simulation of a 10 min charging period with  $\text{SOC}(0) = 0.9$  and  $E_{\text{bat}} = 87$  Wh.



# Model predictive control of a microgrid with heterogeneous battery storage systems

A grid-connected DC microgrid is depicted in Fig.5.1. consisting of renewables production (photovoltaics  $E^{\text{PV}}$  and wind  $E^{\text{WT}}$  energy generation), load  $E^L$  and battery storage is considered, as depicted in Fig.5.1. The grid energy exchange is denoted with  $E^G$  and  $E^{\text{dch}}$  and  $E^{\text{ch}}$  are the battery system discharging and charging energies.

A DC microgrid is connected to the utility grid via a bidirectional AC/DC converter. The grid converter is the master on the microgrid DC bus and maintains the DC bus voltage, and all other devices can freely operate by injecting/drawing power on the microgrid bus. Depending on the type of components and the type of microgrid, various DC/DC and/or AC/DC converters are used to connect the components to the common bus. Power converters represent control points in a microgrid that assure system stability and quality of power supply since the desired flows are ultimately achieved by converter current or voltage control. Therefore, it is important to understand the individual control algorithms for each of the microgrid components in order to enable the coordination of all the components and to implement requested power flows that are calculated from the optimization problem. In this chapter an overview of microgrid components, such as converters and renewables, as well as a control algorithm for the microgrid are described. The battery storage system and the optimal control algorithm are described in the previous chapters.

## 5.1 Photovoltaics and wind turbine control

Controllable microgrid components include renewables: photovoltaics and wind turbine and their corresponding converters. Converters are mostly modeled using the averaged model to omit high-frequency ripple in the current and voltage waveforms. The PV

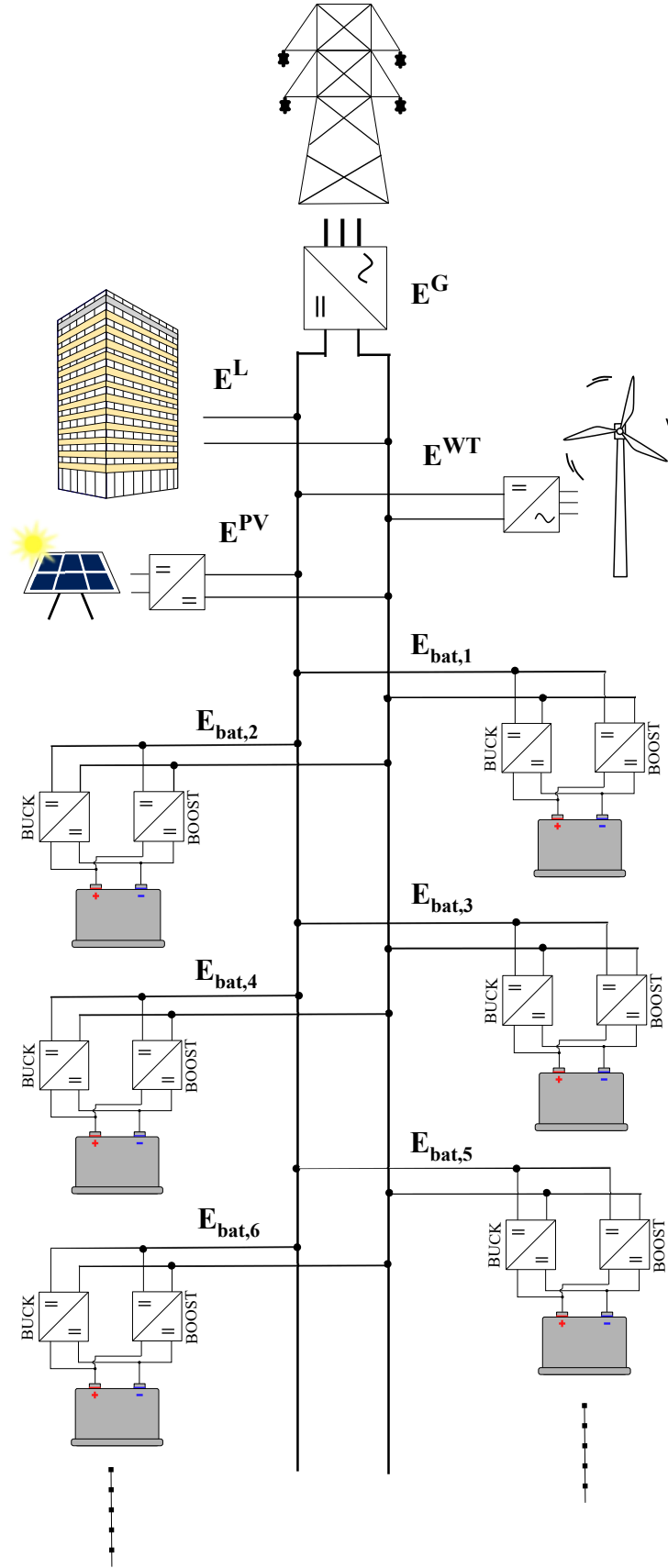


**Figure 5.1.** The considered microgrid topology.

converters are mainly buck or boost converters, depending on the required voltage levels while wind turbines (WTs) demand for more complex converter topologies.

### 5.1.1 Wind turbine model

Wind turbines with horizontal axis have two operating regions. Below rated wind speed all the available wind power is captured and transferred to electricity. Above rated wind speed, power production is saturated at the rated power with passive control or active pitch control. Wind turbine power production model in the below rated speed region is given with [61] [62]:

$$P_{WT}^k = \frac{1}{2} \rho_{\text{air}} R^2 \pi C_P(\lambda, \beta) (v^k)^3, \quad (5.1)$$

where  $\rho_{\text{air}}$  is the air density,  $R$  is the radius of blade disc,  $C_P$  is the power coefficient that reflects the aerodynamical property, dependent of blade aerodynamical property  $\beta$  and of the tip-speed-ratio  $\lambda$ . The speed  $v$  is determined from meteorological data and predictions. In Fig.5.2 the power coefficient curves with respect to the coefficients  $\beta$  and  $\lambda$  are shown. It is evident that all the curves have a maximal value for a specific tip-speed-ratio.

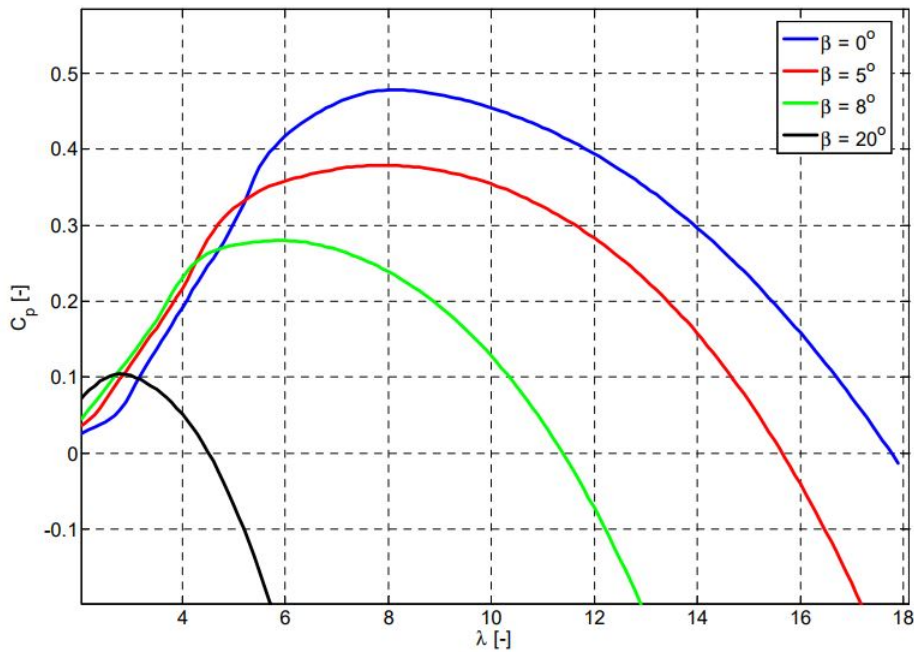


**Figure 5.2.** Power coefficient  $C_P$  curve [62].

Therefore, in order to optimize the power production in this operation region, the control aim is to achieve the optimal value of  $\lambda$  [61]. Tip-speed-ratio is defined as the ratio between the tip speed of a blade and the wind speed:

$$\lambda = \frac{\omega R}{v}, \quad (5.2)$$



where  $\omega$  is the rotor speed in [rad/s]. Originally, wind turbines were fixed speed, where the speed was determined by the utility grid. By introducing a power converter between the wind turbine and the grid, the turbine can operate with variable speed thus enabling optimal power production. The frequency of the generated AC voltage is not constant but can be adjusted to the desired frequency via the power converter.

### 5.1.2 Wind turbine generator converter model

For the generator side converter, only the AC current control loop is needed. The generator side aims to achieve specific generator torque dictated by the aerodynamic torque. Namely, aerodynamic torque is set so that the captured power is at its maximum and the generator torque needs to follow it. The torque reference is given by [63]:

$$T_g^* = K_\lambda \omega_g^2, \quad K_\lambda = \frac{1}{2\lambda_{\text{opt}}^3} \rho_{\text{air}} \pi R^5 C_{P_{\text{max}}}. \quad (5.3)$$

The speed is set to optimal value by a speed controller and executed by pitch control. This torque reference is then achieved with FOC by shaping the stator currents with variable amplitude and frequency to place the generator at the required operating point. The currents are formed, similarly to the currents on the grid side, by proper switching of the power converter transistors. The output of the converter is series of voltage pulses with fundamental harmonic of the required reference voltage. Rotor flux-based FOC is used. The control scheme depends on the generator type, for instance for a squirrel-cage induction machine the model is given by [63]:

$$\frac{di_{sd}}{dt} = \frac{1}{L_l}(u_{sd} - k_s i_{sd} + \Delta u_{sd}), \quad (5.4)$$

$$\frac{di_{sq}}{dt} = \frac{1}{L_l}(u_{sq} - k_s i_{sq} + \Delta u_{sq}), \quad (5.5)$$

$$\frac{di_{mr}}{dt} = \frac{1}{T_r}(i_{sd} - i_{mr}), \quad (5.6)$$

$$\frac{d\rho}{dt} = k_{mr} i_{mr} i_{sq}. \quad (5.7)$$

And the decoupling voltages are:

$$\Delta u_{sd} = \frac{1}{T_r} \frac{L_m^2}{L_r} i_{mr} + L_l \omega_e i_{sq}, \quad (5.8)$$

$$\Delta u_{sq} = -\omega_e \frac{L_m^2}{L_r} i_{mr} - L_l \omega_e i_{sd}. \quad (5.9)$$

Reference current  $i_{sq}$  is calculated from torque reference and reference current  $i_{sd}$  is set to the rated value in normal operation or calculated to maintain constant power in the

above-rated-speed operation [63]:

$$i_{sq} = \frac{T_g^*}{k_m i_{mr}}, \quad (5.10)$$

$$i_{sd} = \frac{\omega_{gn}}{\omega_g}. \quad (5.11)$$

Both current components, magnetizing current and the angle are estimated with unscented Kalman filter (UKF) and then used in control scheme (Fig.5.3). Other machine type models can be found in [64] and [65].

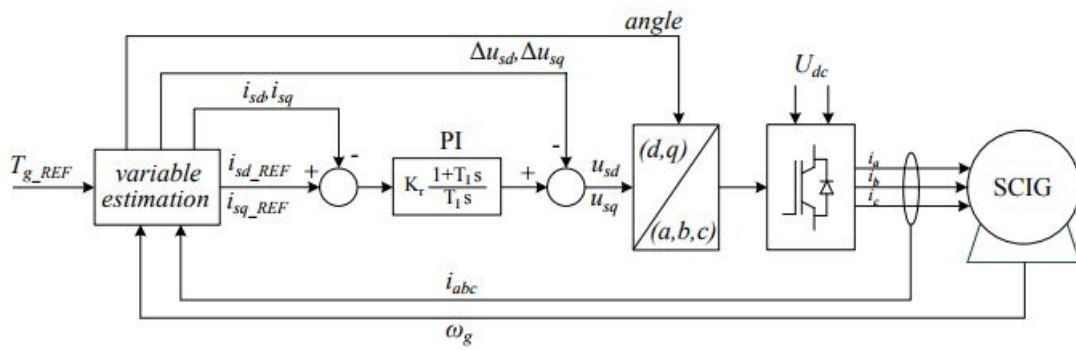


Figure 5.3. Field-oriented control loop [63].

## 5.2 Photovoltaic array

Power production of a photovoltaic system (PV) is given with the expression:

$$P = U_{PV} I_{PV}(\dot{U}_{PV}, E_{c,tot}, T) = f(U_{PV}, E_{c,tot}, T), \quad (5.12)$$

$$\frac{\partial P}{\partial U_{PV}} > 0, \quad \text{for } U_{PV} < U_{PV,max}, \quad (5.13)$$

$$\frac{\partial P}{\partial U_{PV}} < 0, \quad \text{for } U_{PV} > U_{PV,max}, \quad (5.14)$$

where  $\partial$  is the partial derivative,  $E_{c,tot}$  is the total irradiance and  $T$  is the temperature. Photovoltaic systems are described with a power voltage (P-V) characteristic that changes with temperature and irradiance of the system, where every curve has a distinct maximum (Fig.5.4).

The goal is to keep the PV system at the maximum power point. From (5.12), it is evident that, since the current depends on the voltage, in order to control the power, control of the PV output voltage is needed. The conventional MPPT algorithms are Incremental conductance *perturb and observe* ( $P\mathcal{E}O$ ) shown in Algorithm2. It includes

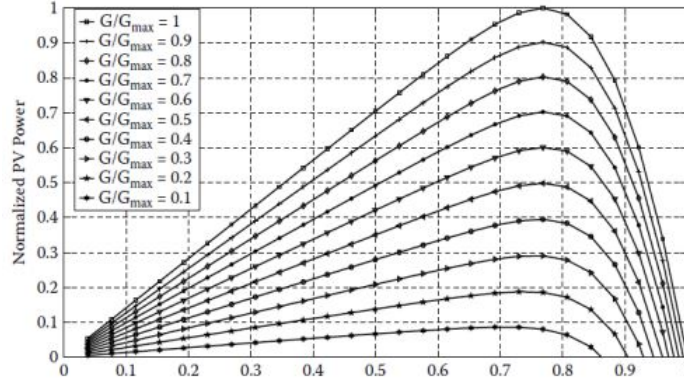


**Figure 5.4.** P-V characteristic of a photovoltaic system, depending on the irradiance [66].

---

**Algorithm 2** P&O algorithm [67]

---

```

 $P_{k-1} = U_{PV,k-1} I_{PV,k-1}$ 
if ( $P_{k-1} < P_{k-2} \ \&\& \ U_{PV,k-1} < U_{PV,k-2}$ ) || ( $P_{k-1} > P_{k-2} \ \&\& \ U_{PV,k-1} > U_{PV,k-2}$ ) then
     $U_{PV,k} = U_{PV,k-1} + \Delta U, \quad \Delta U > 0$ 
else
    if ( $P_{k-1} < P_{k-2} \ \&\& \ U_{PV,k-1} > U_{PV,k-2}$ ) || ( $P_{k-1} > P_{k-2} \ \&\& \ U_{PV,k-1} < U_{PV,k-2}$ )
    then
         $U_{PV,k} = U_{PV,k-1} - \Delta U, \quad \Delta U > 0$ 
    end if
end if

```

---

a perturbation in the voltage causing power variation of the PV array. The PV output is compared with the previous power. If the power increases the same process is repeated otherwise the perturbation is reversed. If a positive perturbation causes an increase in power, the operating point is left of the MPP and vice versa. The P&O algorithm is the most widely used. Other MPPT algorithms are based for example on fuzzy logic controllers, genetic algorithms, particle swarm optimization [68,69].

The MPPT algorithms calculate the reference voltage, which is then forwarded to the converter. Photovoltaics are connected through a DC/DC converter to the DC microgrid. Often, the PV output voltage is several times greater than the DC bus voltage, therefore buck converters are used [70]. The topology of a buck converter is presented in Fig.4.2, denoted with dashed blue lines (microgrid side of the buck-boost converter). For the control circuit, equations (4.1)-(4.8) derived in Section4.1 can be applied. In (4.8) the storage side current  $-d_1 \bar{i}_{L1}$  is replaced with the PV output current  $i_{PV}$ .

### 5.3 Grid converter control

In this section the grid DC/AC converter topology and averaged model are shown. This converter operates as the master and is in charge of maintaining the DC link voltage level. After reviewing the conventional control algorithm implementations of the grid converter

topology, a problem with the DC link stability is observed however, this problem is scarcely investigated in the literature. Since the grid converter is in charge of evacuating/injecting the calculated optimal energy flows, its stable operation is critical to the whole system. In succeeding sections, a stability analysis is performed and a robust controller design procedure is proposed. The proposed controller is robust to parameter inaccuracy which is important due to varying operating conditions in a microgrid.

Conventional converter control relies on proportional integral (PI) or proportional resonant (PR) controllers, for current control. Voltage control is designed using a cascaded structure. Control loops performance is significantly affected by the parameter accuracy, mainly contributed by the grid impedance [71,72], which varies with the load characteristics and overall grid conditions [73,74]. In order to increase the robustness, damping techniques are considered and different control algorithms, specifically designed to achieve robustness against parameter inaccuracy and/or harmonics attenuation, are developed [75,76,77]. All the aforementioned mostly concerns with current control loops while DC link control is less investigated. The PI controllers are the most common choice for DC link voltage control due to simplicity and easy implementation as presented in [78,79]. The nonlinearities present in the DC link, however, deteriorate the performance of the PI controller when it deviates from the operating point. Sophisticated algorithms such as adaptive control [80], feedback linearization [81], neural networks and fuzzy logic [82,83,84], model predictive control (MPC) [85,86] and sliding-mode control (SMC) [87,88] are also found in literature however, deeper and systematic modeling of a DC link and corresponding controller design is scarcely present. Most of the approaches imply a single capacitor in a DC link. In [89], a stability analysis is performed. In [90], similar conclusions are drawn with an added additional DC link filter. In the listed literature, the authors unanimously identify and highlight the need for robust controllers and usually rely on parameter tuning experience.

A systematic approach for DC link voltage control is proposed, further relied on the inner current control loops in order to reduce approximations and neglected components. The unstable pole of the DC link is respected and system is stabilized by using an analytical approach. The controller parameters are defined by the inner control loop and the model function. There is only a single degree of freedom, that adjusts the speed of the closed loop and the overshoot. The method based on Truxal-Guillemain approach [91] introduces proportionate settling times but with a somewhat larger overshoot when compared with conventional approaches, however the approach is:

- robust to operating point changes regardless of only a single one chosen for linearization
- based on the real model of the system
- robust to DC link or grid filter and grid impedance parameter variations.

## 5.4 Current control

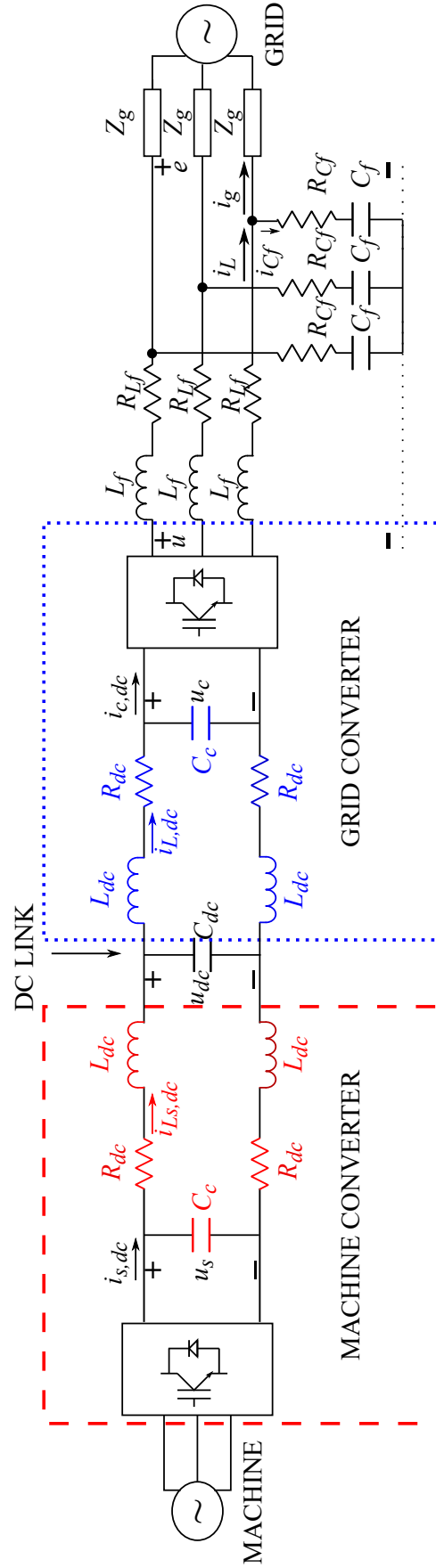


Figure 5.5. Back-to-back converter scheme with considered complex DC link.

In a typical voltage control mode, the current control loop is responsible for setting the converter voltage reference value. The first step in modeling is to obtain the voltage to current transfer function. In Fig.5.5, considered back-to-back configuration scheme is shown. The complex DC link topology is introduced by connecting two motor drives via the common DC link, thus adding additional inductances and capacitances (filter) into the DC link. The grid side of the configuration consists of an inverter and an LC filter. The grid impedance effects are taken into account by adding additional current sensors at the point-of-connection (PCC) and synchronizing the control system to the voltage at the capacitance terminals of the filter. The grid impedance is therefore excluded from the derived model. Variables  $i_L$  and  $i_g$  denote the converter and grid currents. Variable  $u$  denotes the converter phase voltage and  $e$  represents the phase voltage at the connection point to the grid. The current dynamics is separated into a cascade. The inner loop controls the converter current and sets the converter voltage reference while the outer loop controls the grid current as shown in Fig.5.5[92].

### 5.4.1 Converter current control

A step-by-step modelling of the current control loops is presented in [92] in detail. A concise version is given in the sequel for the reader's convenience. The differential equation of the inductive part of the filter  $L_f$ , with its corresponding resistance  $R_{Lf}$ , is for the three phases given by:

$$L_f \frac{di_{Lk}}{dt} + R_{Lf} i_{Lk} = u_k - e_k, \quad k = a, b, c, \quad (5.15)$$

and transferred to  $(d, q)$  coordinate system rotating with frequency  $\omega$  and aligned with the grid voltage vector. The derived L filter transfer functions are:

$$G_{idd} = \frac{I_{Ld}}{\Delta U_d} = \frac{1}{sL_f + R_{Lf}}, \quad G_{iqq} = \frac{I_{Lq}}{\Delta U_q} = G_{idd}. \quad (5.16)$$

Note that the derived model is tied to the voltage difference  $\Delta U_d = U_d - E_d$ ,  $\Delta U_q = U_q - E_q$  rather than the grid voltage, which makes it more independent of the grid impedance.

The control algorithm is implemented in discrete-time domain and the effect of discretization is taken into account together with converter delay. The inner open transfer function is therefore:

$$G_{0,in} = \frac{I_L}{I_L^* - I_L} = K_{R,in} \frac{sT_{I,in} + 1}{sT_{I,in}} G_{idd} \frac{1}{1 + s(T_{ds} + T_{sw}/2)}, \quad (5.17)$$

where  $T_{ds}$  and  $T_{sw}$  are controller sample time and converter switching period [93]. Both transfer functions are first-order lag type with a clear dominant time constant suitable for applying a proportional-integral (PI) controller based on a *magnitude optimum* (MO)

approach [94]. The inner loop controller parameters are chosen:

$$T_{I,in} = \frac{L_f}{R_{L_f}}, \quad K_{R,in} = \frac{1}{2} \frac{L_f}{0.5T_{sw} + T_{ds}}. \quad (5.18)$$

The process transfer functions  $G_{idd}$  and  $G_{iqq}$  are equivalent and therefore (5.17) and (5.18) are applied to both axes.

### 5.4.2 Grid current control

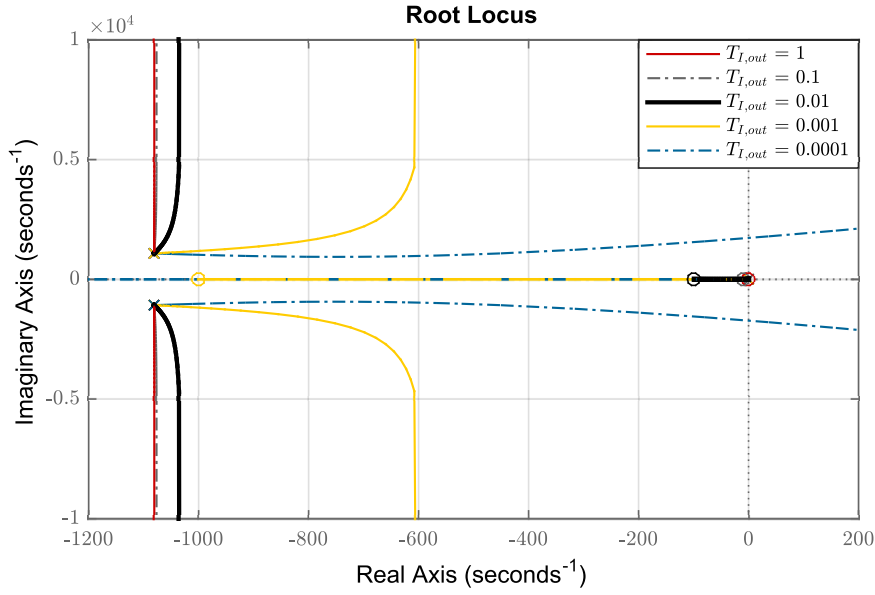


**Figure 5.6.** Root locus curves tuning the grid current (middle) control loop.

For the grid current control loop, the capacitor part of the filter is modeled by following the same procedure as for the inductive part in order to relate  $i_L$  and  $i_g$ , and the following coupled relations are obtained:

$$I_{gd} = I_{Ld} - G_{cdd}E_d + G_{cq d}E_q, \quad \rightarrow \quad \frac{I_{gd}}{I_{Ld}} = 1, \quad (5.19)$$

$$I_{gq} = I_{Lq} - G_{cqq}E_q + G_{cdq}E_d \quad \rightarrow \quad \frac{I_{gq}}{I_{Lq}} = 1. \quad (5.20)$$

The corresponding transfer and decoupling functions are derived in [92]. Open loop transfer function of the outer loop is:

$$G_{0,out} = \frac{I_g}{I_g^* - I_g} = G_{R,out}G_{c,in} = K_{R,out} \frac{s + \frac{1}{T_{I,out}}}{s} G_{c,in}, \quad (5.21)$$

where  $G_{c,in}$  is the closed loop transfer function of the converter current loop,  $G_{c,in} = G_{0,in}/(1 + G_{0,in})$ , and  $G_{0,in}$  is the open loop transfer function obtained in (5.17).

The outer loop controller  $G_{R,out}$  is of the PI type and its parameters are chosen by using a root locus approach [95] in order to achieve at least two times slower dynamics than the converter current loop, which is necessary to respect the cascaded control and avoid the control loops interference. First, the controller integrator gain is varied while keeping the proportional unity gain. The root locus curves for  $T_{I,out} = [1, 0.1, 0.01, 0.001, 0.0001]$  are shown in Fig.5.6. The objective is to place the zero further away from the imaginary axis, which would make its effect on the closed-loop dynamics negligible. However, from the root locus curves, it is concluded that by increasing the zeros, the curves approach the imaginary axis and even cross it for  $T_{I,out} = 0.0001$  (blue dot-dashed line). The integral gains  $T_{I,out} = [0.01, 0.001]$  are chosen as a good trade-off and are used in the gain analysis. Figure 5.7 shows open loop and closed loop Bode plots, and the step response for  $K_{R,out} = [10, 100, 1000]$ . Increase of the gain also increases the bandwidth of the system. The phase characteristic of the system with  $T_{I,out} = 0.001$  is more uniform over a wide range of frequencies with steady phase margin for different gains. The main objective of this controller design is to have a fast and robust response while respecting the inner loop dynamics. Comparing with the inner control loop time constant (approximately 0.0012 s) and looking at the shape of the transient response (Fig.5.7(c)), the light blue line ( $T_{I,out} = 0.001$ ,  $K_{R,out} = 100$ ) is chosen as a starting point for further tuning. Controller parameters are further tuned until a satisfying result is found (green full line):  $K_{R,out} = 371.76$ ,  $T_{I,out} = 0.00035$ . The block scheme of the current control loops is shown in Fig. 5.8, where red denotes measured variables and dashed lines denote coupled variables. The coupling and decoupling transfer functions of the current control loops are defined in [92].



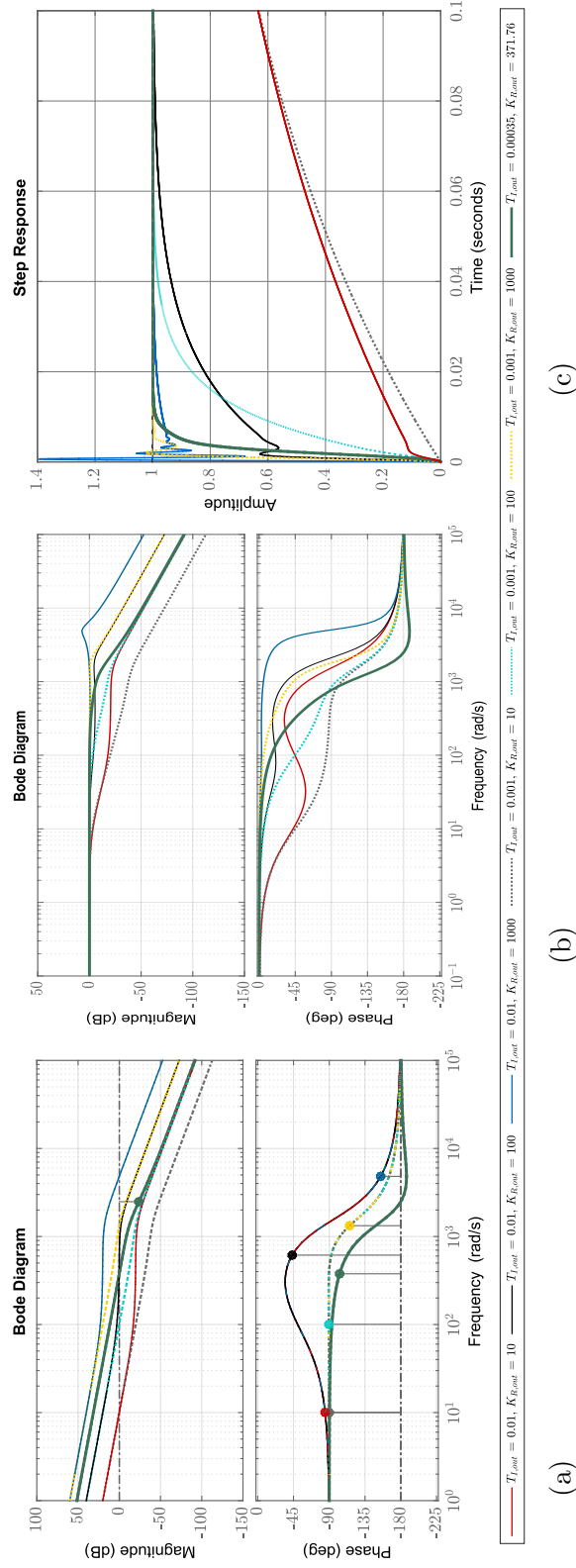


**Figure 5.7.** (a) Bode diagram of the open loop system  $G_{0,out}$  for different controller gains. (b) Bode diagram of the closed loop system  $G_{c,out}$  for different controller gains. (c) Step responses of the closed loop system for different controller gains.

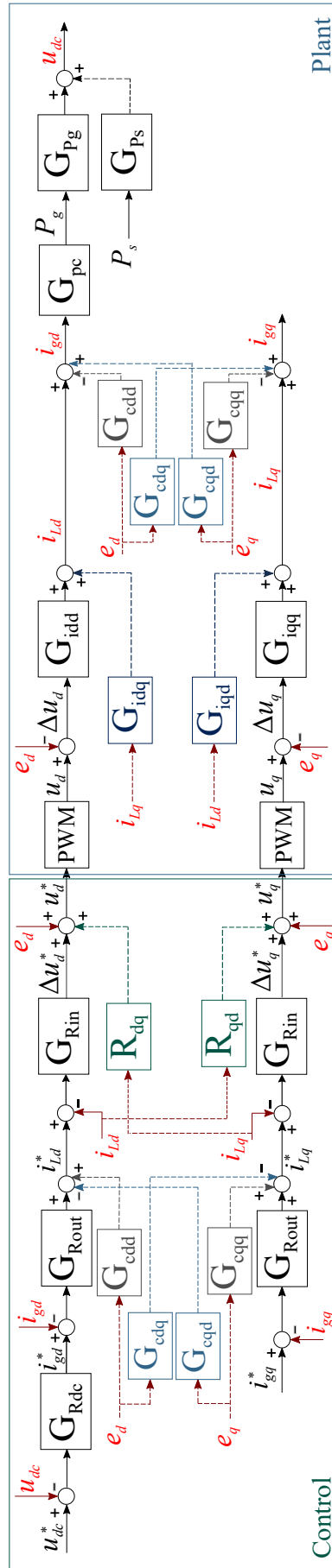


Figure 5.8. Control loop of the grid converter.

## 5.5 Voltage control loop

The DC voltage control loop maintains the balance between the machine power (generated or consumed) and the power delivered to the grid. The DC link topology is shown in Fig. 5.5. In [92], the grid side of the DC link is modelled (blue part) while neglecting the machine part of the DC link (red side). This, however, proved as unjustified decoupling, confirmed also by simulation and experimental results, as will be described later.

Following the same procedure as in [92], the full state space model of the DC link is given by:

$$\dot{\mathbf{x}} = \begin{bmatrix} -\frac{R_{dc}}{L_{dc}} & 0 & \frac{1}{2L_{dc}} & -\frac{1}{2L_{dc}} & 0 \\ 0 & -\frac{R_{dc}}{L_{dc}} & 0 & \frac{1}{2L_{dc}} & -\frac{1}{2L_{dc}} \\ -\frac{1}{C_c} & 0 & 0 & 0 & 0 \\ \frac{1}{C_{dc}} & -\frac{1}{C_{dc}} & 0 & 0 & 0 \\ 0 & \frac{1}{C_c} & 0 & 0 & 0 \end{bmatrix} \mathbf{x} + \begin{bmatrix} 0 & 0 \\ 0 & 0 \\ 0 & \frac{1}{C_c} \\ 0 & 0 \\ -\frac{1}{C_c} & 0 \end{bmatrix} \mathbf{u}, \quad (5.22)$$

where  $\mathbf{x} = [i_{Ls,dc} \ i_{L,dc} \ u_s \ u_{dc} \ u_c]^\top$  and  $\mathbf{u} = [i_{c,dc} \ i_{s,dc}]^\top$ . Two additional states in the form of inductance current  $i_{Ls,dc}$  and capacitor voltage  $u_c$  on the machine-side are added. The DC converter current from (5.22) is substituted by grid power  $P_g$  in order to relate the model with the AC side of the converter model. The source side current  $i_{s,dc}$  is substituted by source AC power thus describing the model using two comparable variables:

$$i_{c,dc}u_c = \frac{P_g}{\eta_g}, \quad i_{s,dc}u_s = \eta_s P_s, \quad (5.23)$$

where  $\eta$  is the converter efficiency. After the substitution, the model from (5.22) becomes nonlinear and the linearization is performed:

$$\begin{aligned} \Delta i_{c,dc} &= \frac{1}{\eta_g u_{c0}} \Delta P_g - \frac{i_{c,dc0}}{u_{c0}} \Delta u_c, \\ \Delta i_{s,dc} &= \frac{\eta_s}{u_{s0}} \Delta P_s - \frac{i_{s,dc0}}{u_{s0}} \Delta u_s. \end{aligned} \quad (5.24)$$

The dependence between the DC link voltage and the inputs is obtained by solving the set of linear equations from (5.22) and (5.24), and is given by:

$$\Delta U_{dc} = G_{P_g} \Delta P_g + G_{P_s} \Delta P_s, \quad (5.25)$$

$$G_{P_g} = -\frac{n_{2pg}s^2 + n_{1pg}s + n_{0pg}}{s^5 + d_4s^4 + d_3s^3 + d_2s^2 + d_1s + d_0} \Delta P_g, \quad (5.26)$$

$$G_{P_s} = \frac{n_{2ps}s^2 + n_{1ps}s + n_{0ps}}{s^5 + d_4s^4 + d_3s^3 + d_2s^2 + d_1s + d_0} \Delta P_s. \quad (5.27)$$

where  $n_{0pg} - n_{2pg}$ ,  $n_{0ps} - n_{2ps}$  and  $d_0 - d_4$  are the transfer function coefficients. The AC power  $P_s$  is considered as a disturbance and only the transfer function  $G_{P_g}$  is used in the DC voltage control loop, shown in Fig.5.8:

$$G_{0,dc} = \frac{U_{dc}}{U_{dc}^* - U_{dc}} = G_{R,dc} \frac{U_{dc}}{I_{gd}^*} = G_{R,dc} \frac{I_{gd}}{I_{gd}^*} \frac{P_g}{I_{gd}} \frac{U_{dc}}{P_g} = G_{R,dc} G_{c,out} G_{pc} G_{P_g}. \quad (5.28)$$

A power to current conversion is added:  $P_g = G_{pc} I_{gd}$  and  $G_{pc} = \frac{3}{2} E_{d,0}$  is introduced to relate DC link voltage transfer functions with the current controllers. It is assumed that PLL forces  $E_q$  to 0.

The open loop transfer function from (5.28) results with an unstable pole. For the design of a DC link controller, Truxal-Guillemine (TG) approach is chosen[91]. The method is well established, systematic model-based approach, also known to be highly sensitive to model parameters variation, which is here avoided by introducing  $\Delta U$  dependency in (5.16), rather than  $E$ . The model discrepancy that arises from variations in resistances, capacitances, and inductances, but mostly deviation from chosen linearization operating point (5.24), is compensated by robust PI controllers of the inner loops, which is also examined in the experimental results. The current closed loop from (5.21) has three poles: two complex and one real pole, and is simplified to a first order lag system. The time constant is calculated by minimizing the mean squared error between the real and the approximated function [92]. In the TG approach, first the desired closed loop transfer function is modelled. The pole excess of the model function is chosen equal or greater to the pole excess of the process function. The pole excess of the open loop process function is 4. The denominator is chosen to be a n-order polynomial with fixed coefficients while coefficients of the numerator are adjustable. This finally enables pole stabilization. The desired model function is written in form of:

$$G_m(s) = \frac{\alpha(s)}{\beta(s)} = \frac{G_{R,dc} G_{c,out} G_{pc} G_p}{1 + G_{R,dc} G_{c,out} G_{pc} G_p}. \quad (5.29)$$

Following from (5.29), the controller is defined as:

$$G_{R,dc} = \frac{1}{G_{c,out} G_{pc} G_p} \frac{\alpha}{\beta - \alpha}. \quad (5.30)$$

The expression  $\beta - \alpha$  contains the unstable pole since the objective of this approach is to relocate it and not to cancel it with the controller zero. This condition is mathematically written as:  $\beta - \alpha = (s - s_p)P(s)$ , where  $P(s)$  is an auxiliary polynomial and  $s_p$  is the unstable pole. Since the order of  $\alpha(s)$  and  $\beta(s)$  is not specified (only the ratio is), the

following possibility is considered as a starting point:

$$\beta_4 s^4 + \beta_3 s^3 + \beta_2 s^2 + \beta_1 s + \beta_0 - \alpha_0 = (s - s_p)(P_3 s^3 + P_2 s^2 + P_1 s + P_0). \quad (5.31)$$

Following from (5.31), a set of equations is obtained, where the  $\beta_i$  coefficients are defined by the choice of the numerator polynomial type and  $\alpha_0 = \beta_0$  is chosen in order to ensure a unity gain. Since the system from (5.31) has no real roots, the numerator and denominator order is increased by one and the approach is repeated until a solution is found. The final model function for the considered DC link is:

$$G_m(s) = \frac{\alpha_1 s + \omega_n^5}{(s + \omega_n)^5}, \quad (5.32)$$

$$\alpha_1 = (5\omega_n^4 + 10s_p\omega_n^3 + 10s_p^2\omega_n^2 + 5s_p^3\omega_n + s_p^4),$$

where the parameter  $\omega_n$  determines the closed loop dynamics. The controller is obtained by putting (5.32) into (5.30):

$$G_{R,dc} = -\frac{a_6 s^6 + a_5 s^5 + a_4 s^4 + a_3 s^3 + a_2 s^2 + a_1 s + a_0}{s^6 + b_5 s^5 + b_4 s^4 + b_3 s^3 + b_2 s^2 + b_1 s + b_0}. \quad (5.33)$$

The root locus of the open loop with the controller from 5.33 is shown in Fig. 5.9.

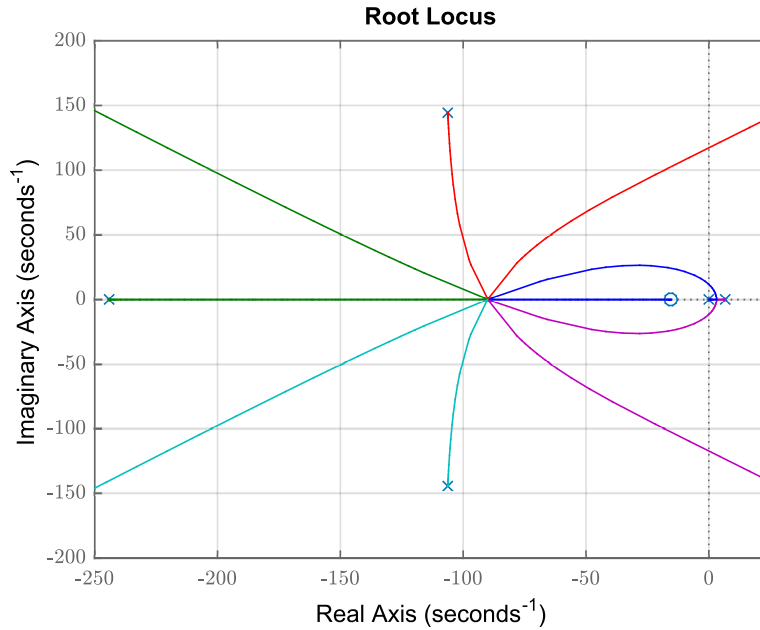


**Figure 5.9.** Root locus curves for the DC link voltage open loop transfer function.

## 5.6 Robustness analysis

The robustness of the proposed controllers is studied in this section. Figure 5.10 shows the change of the Bode plot of the open-loop system when grid filter, grid impedance and DC link filter parameters change. In Fig. 5.10(a), Bode plot for the grid current open loop from (5.21) is shown for LC grid filter parameter changes of  $\pm 25\%$  and  $\pm 50\%$ . The phase and gain margins (PM and GM) of the original system are 23.7 dB and  $74.4^\circ$ . The gain margin barely changes with parameter variations. The phase margin varies between  $85.8^\circ$  for  $-50\%$  (red line) and  $65.1^\circ$  for  $50\%$  (green line), while providing a safe distance from the edge of stability for all cases and thus the high robustness of the approach. Figure 5.10(b) shows the Bode plot for grid impedance changes from a stiff grid ( $Z_g = 0.003 \Omega$ ) to a weak grid without and with the reactive component. For all the cases the current loop remains stable with phase margin between  $77^\circ$  and  $82^\circ$ . In Fig. 5.10(c), Bode plot of the DC voltage open loop from (5.28) for DC link filter parameter changes of  $\pm 10\%$  and  $\pm 20\%$  is shown. The GM and PM of the original system are 8.19 dB and  $33.8^\circ$ . The GM changes from 9.84 dB for  $+20\%$  (green line) to 6.14 dB for  $-20\%$  (red line). The PM changes between  $36^\circ$  (green line) and  $29.2^\circ$  (red line). The system remains stable, with similar stability margins despite the significant changes of the parameters.

The robustness to the operating point variation (linearization) is shown in Fig. 5.11. The Bode plots are given for the DC link voltage open loop from (5.28). Figure 5.11(a) shows  $\pm 2.5\%$ ,  $\pm 5\%$  changes from  $U_{dc,0}$ . The stability margins change approximately  $\pm 5.5\%$  for GM and  $\pm 2.5\%$  for PM. In Figure 5.11, deviations of the disturbance current  $i_{s,dc}$  from the operating point are shown. The gain margin stays in the same span as in the former example. The phase margin changes  $\pm 22\%$  from the original system. The last example shows converter efficiency variations (Fig. 5.11(c)). The changes have little or no impact on the phase margin while the gain margin changes in the range  $\pm 3\%$ . According to the analysis, the designed control algorithm is able to operate in a broad range of operating points without becoming unstable. The proposed algorithm is also compared with conventional control methods. The outer loop controller is substituted by a PI controller with parameters of the outer loop controller chosen according to the *symmetric optimum* approach [94] and uses a simplification of the DC link process function (the additional components are neglected):  $G_{U_{dc}} = -\frac{1}{sC_\Sigma U_{dc0}}$ ,  $C_\Sigma = C_c + C_{dc} + C_c$ . For the inner loop, three control structures are observed: *i*) the cascaded current control loop proposed in this paper, *ii*) current control loop consisting only of the L filter function while neglecting the capacitance (common method [90,96]) with a PI controller, *iii*) current control loop from previous example with the PR controller. The PR controller is designed using the gains of the inner loop PI controller described in the paper and choosing  $\omega_c = 1$  rad/s in order to avoid the infinite gain problems with the ideal PR controller [97,98]. In Fig. 5.12a, Bode plots of the DC link voltage open loop for all three examples are shown. The GM is approximately 25.8 dB for all examples and the PM changes between  $67.7^\circ$  and  $75.5^\circ$ . In Fig. 5.12(b), Bode plots for different values

of the parameter  $a$  are shown for the PI+PI topology. The parameter  $a$  (parameter of symmetric optimum design) determines the speed of the system. However, simulations show problems with the DC-link PI controller when deviating from the operating point while the control loop becomes unstable. By increasing  $a$ , the phase margin also increases. The tuning process is repeated several times in order to achieve an acceptable response (Fig.5.12(c)). The same problem occurs with the PI+PI+PI topology. As a conclusion, conventional controllers show larger robustness (higher margins) for a particular linearized model and selected grid impedance but are more sensitive when system deviates from the initial assumptions, which is expected to occur regularly in normal operation.

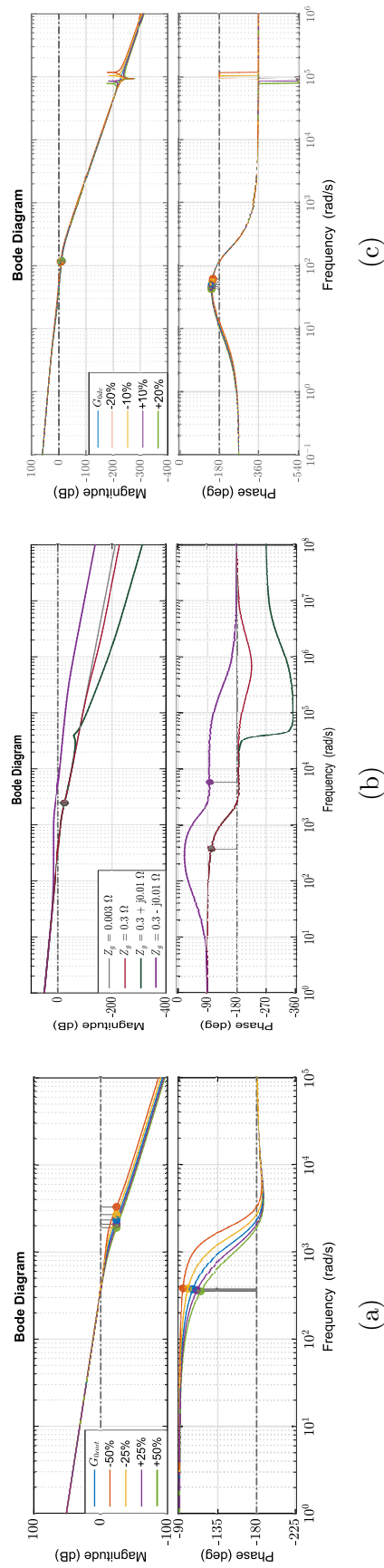


**Figure 5.10.** (a) Grid current open loop Bode plot for grid filter parameter changes  $\pm 50\%$ . (b) Grid current open loop Bode plot for grid impedance variations (c) DC link voltage open loop Bode plot for DC link filter parameter changes  $\pm 20\%$ .



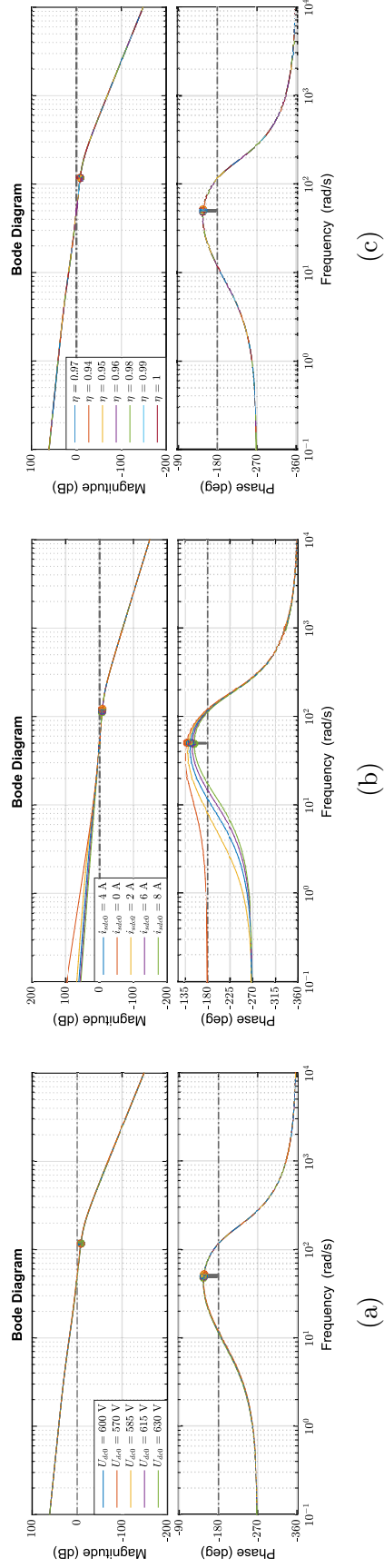


**Figure 5.11.** DC link voltage open loop Bode plots for selected operating points: (a)  $\pm 5\% U_{dc0}$ , (b)  $\pm 100\% i_{s,dc0}$ , (c)  $\pm 3\% \eta$ .

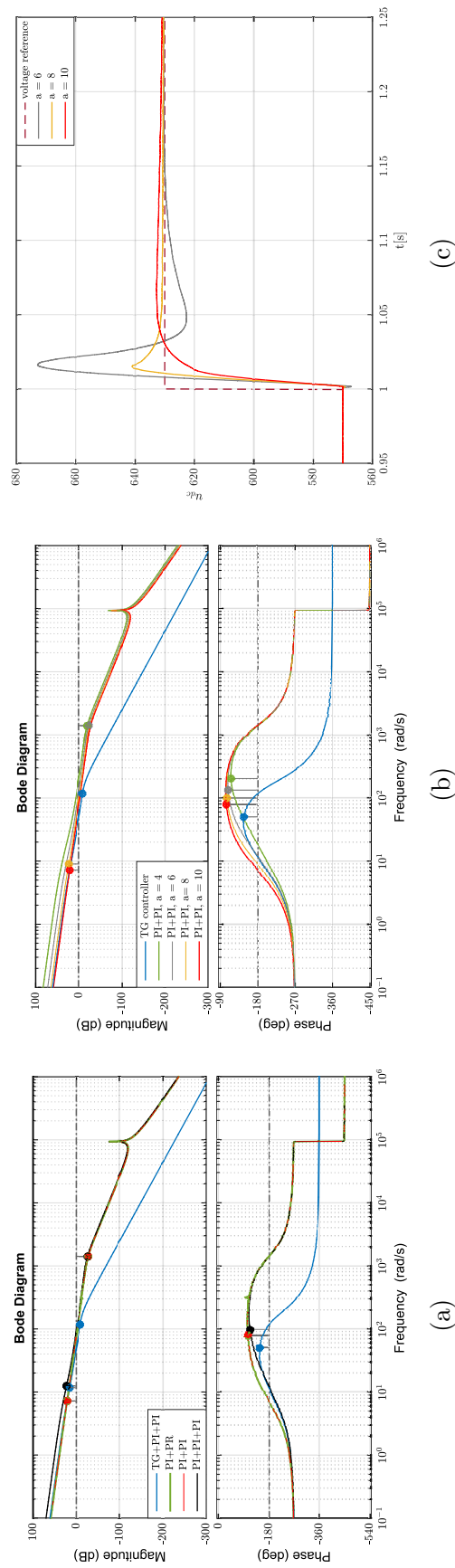


**Figure 5.12.** DC link voltage open loop Bode plots for conventional control methods: (a) outer loop PI controller and inner loop PI or PR controller and outer loop PI controller with the cascaded inner loop, (b) PI+PI, with different values for symmetric optimum coefficient  $a$ , (c) Step responses for the PI+PI control structure, for different values of  $a$ .

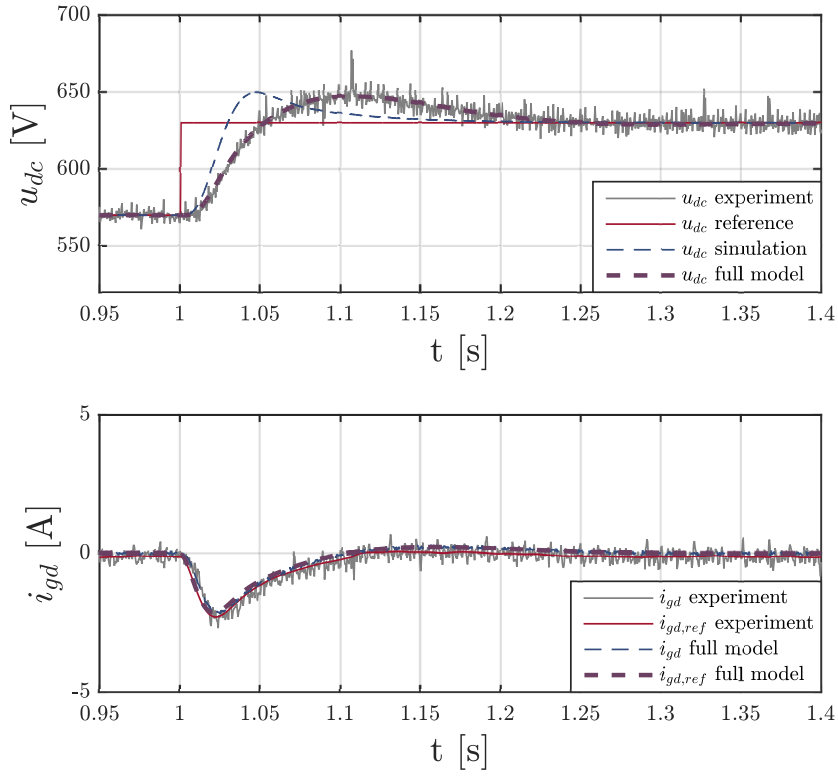
## 5.7 Experimental results

The experimental setup consists of an induction machine and a permanent magnet synchronous machine with coupled shafts, where one acts as a wind turbine emulator and the other is used as a generator with corresponding generator and grid side converters, i.e. back-to-back converter. Both converters on the generator side are Danfoss FC302 motor drives of rated power and current of 7.5 kW and 16 A, respectively, connected to the common DC-link bus to form a back-to-back converter topology with complex DC link (Fig.5.5). The rated DC link voltage is 600 V. Control boards are replaced by custom-designed boards for achieving controllable IGBTs. The developed control algorithm is implemented on a real-time dSPACE 1103 controller. The switching frequency of the converters used in experiments is  $f_{sw} = 8$  kHz with sample time of  $T_{ds} = 0.4$  ms.

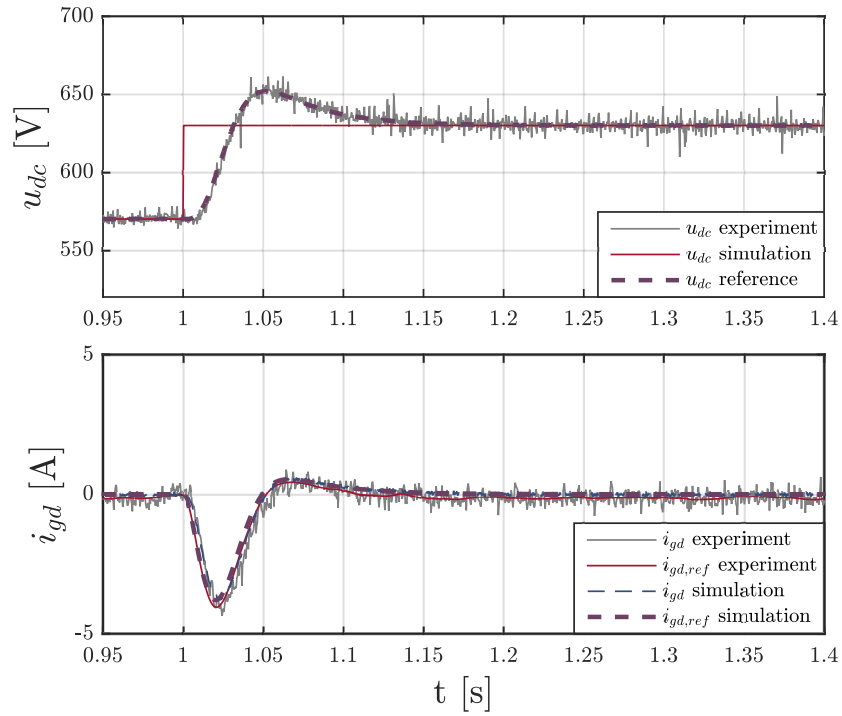
The setup is installed in the laboratory with a large share of renewables where voltage conditions are highly dependable on the loads of the rest of the building. The experiments are performed during high and low load conditions: "low grid impedance scenario" and "high grid impedance scenario". The grid impedance is determined by the method described in [99], and presented in Table5.1 as well as grid converter parameters and controller parameters for all three controllers. The DC controller coefficients are obtained for  $\omega_n = 90$  rad/s. Simulation results are obtained by using the co-simulation of MATLAB/Simulink and PLECS. Figure5.13 shows a comparison of simulation and experimental results for a step increase in DC link voltage from 570 V to 630 V. For the case of controllers design, while taking into account partial DC link model (as in [92]), there is a clear discrepancy between simulation and experimental results as shown in Fig. 5.13. Response "full model" depicts the results with the full DC link model (5.22) and the controller from (5.30). Since PI controllers are robust, the system is still stable but underperformed and the decoupling is therefore not justified. Results obtained with the controller from (5.30) show matching simulation and experimental results in terms of rise time, overshoot and settling times, as shown in Fig.5.14.

Figure5.15 shows DC link voltage and  $d, q$  grid currents responses for a DC link voltage reference step change of 60 V in high and low grid impedance scenarios. The disturbance is compensated after 0.14 s transient for the chosen  $\omega_n = 90$  rad/s in (5.30). The figure also shows coinciding results for the case of high and low grid impedance, which confirms the robustness of the proposed control structure. Introduction of additional pre-filter would eliminate the overshoot but would also introduce significant delay in the response, which is not favorable in the current application.

The experiment is also performed for a step increase in generator power from 3.15 kW to 3.75 kW. The experiments are conducted for high and low grid impedance scenarios, which is shown in Fig.5.16 as a barely noticeable difference in responses. Increased current in the DC link causes a temporary increase of the DC link voltage, which is compensated by larger current injected to the grid. The proposed control structure compensates the disturbance with 1% DC link voltage deviation.



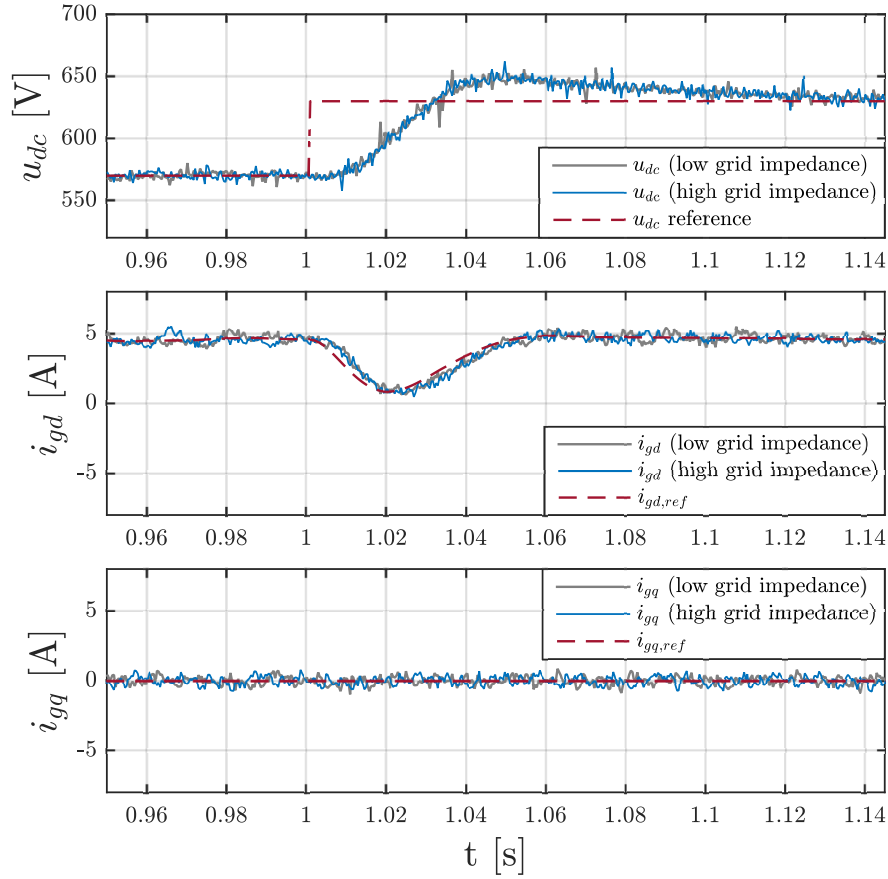
**Figure 5.13.** Comparison between experimental and simulation results with the controller from [92].



**Figure 5.14.** Comparison between experimental and simulation results with the controller from (5.30).

**Table 5.1.** Parameters used for results

Parameter	Value	Parameter	Value
High $Z_g$	$0.059-j1.366 \Omega$	$a_0$	$6.175 \cdot 10^{12}$
Low $Z_g$	$0.345-j0.92 \Omega$	$a_1$	$4.159 \cdot 10^{11}$
$L_f$	53.1 mH	$a_2$	$1.162 \cdot 10^9$
$R_{Lf}$	$0.32 \Omega$	$a_3$	$6.278 \cdot 10^5$
$C_f$	10 $\mu\text{F}$	$a_4$	1246.0
$C_{dc}$	100 nF	$a_5$	$8.993 \cdot 10^{-5}$
$C_c$	500 $\mu\text{F}$	$a_6$	$1.413 \cdot 10^{-7}$
$L_{dc}$	1.135 mH	$b_0$	0
$R_{dc}$	$0.15 \Omega$	$b_1$	$6.918 \cdot 10^{12}$
$K_{R,in}$	57.4054	$b_2$	$7.509 \cdot 10^{10}$
$T_{I,in}$	0.1713 s	$b_3$	$4.213 \cdot 10^8$
$K_{R,out}$	0.1301	$b_4$	$1.025 \cdot 10^6$
$T_{I,out}$	0.00035 s	$b_5$	588.8

**Figure 5.15.** Experimental results with respect to  $u_{dc,ref}$  step change from 570 V to 630 V.

The three-phase grid current is shown in Fig.5.17. Total harmonic distortion (THD) of the currents in case of low grid impedance is approximately 6.01%, while for high grid impedance THD is 6.41%. The THD is further significantly reduced by the utility grid transformer (55.1 mH, 10/0.4 kV, 8 MVA) resulting in satisfying the grid codes and keeping the THD below 5%. The THD increase for approximately 40% higher grid

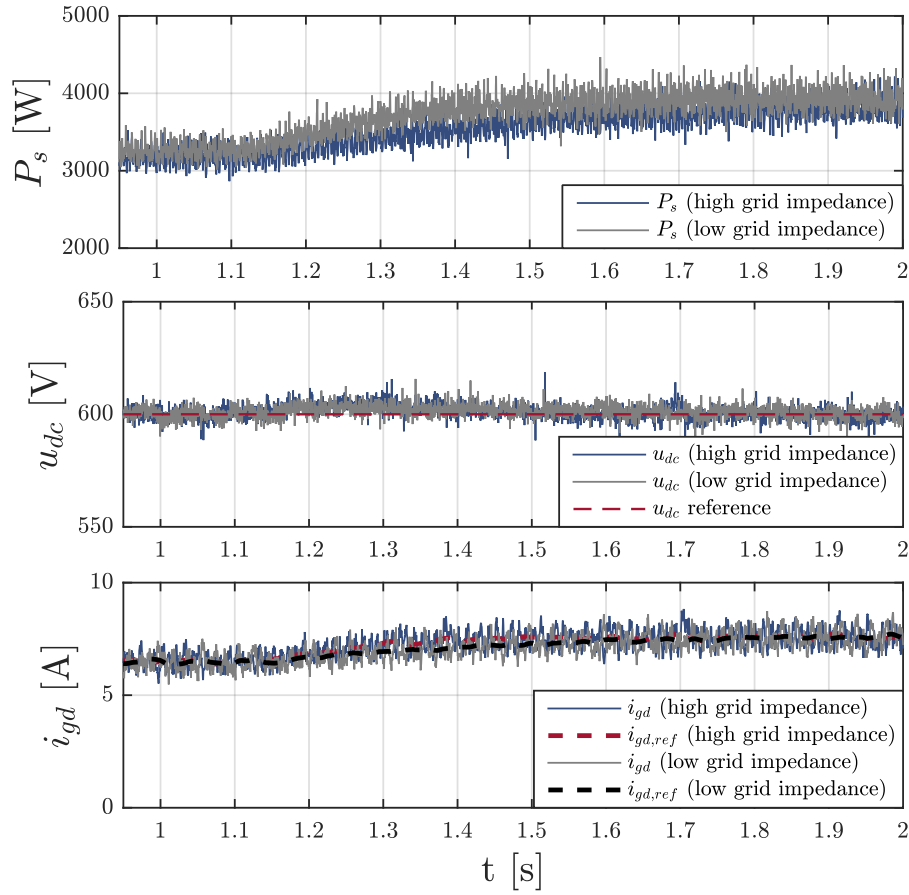


**Figure 5.16.** Experimental results with respect to  $P_s$  change from 3.15 kW to 3.75 kW.

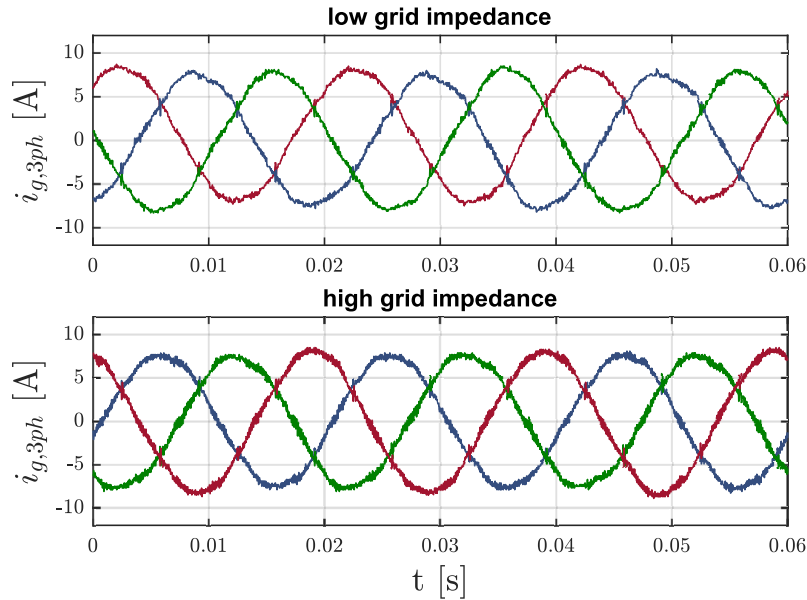


**Figure 5.17.** Three phase grid current.

impedance is very low, and mainly due to basic phase-locked loop (PLL) used [100]. Basic PLL topology is designed to capture a single voltage harmonic, which is enough for stiff grid conditions. In the current example of different grid impedances and highly expressed third harmonic, the basic PLL topology is not able to respect this for transformation of

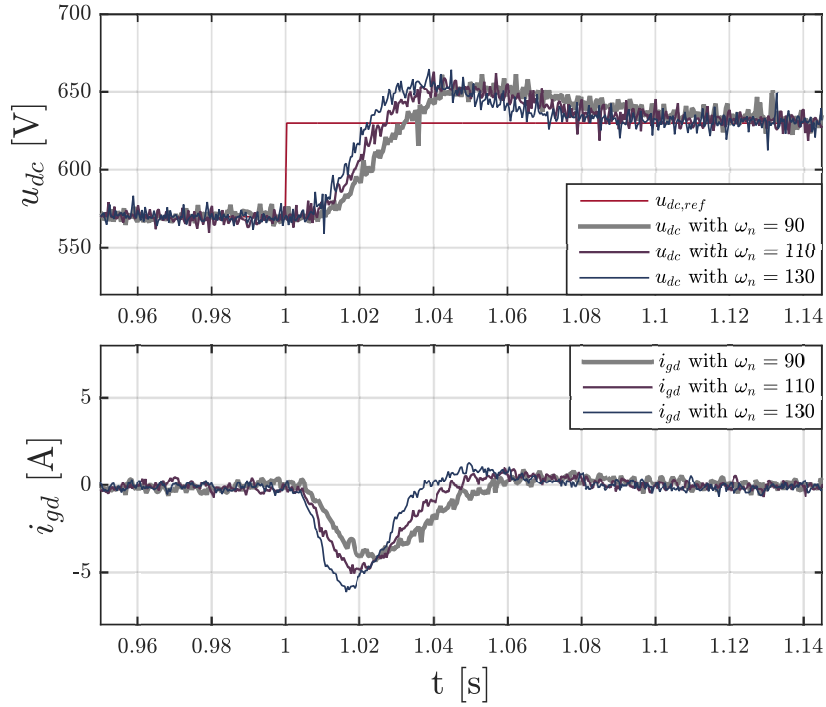


**Figure 5.18.** DC link response with respect to  $\omega_n$  changes.

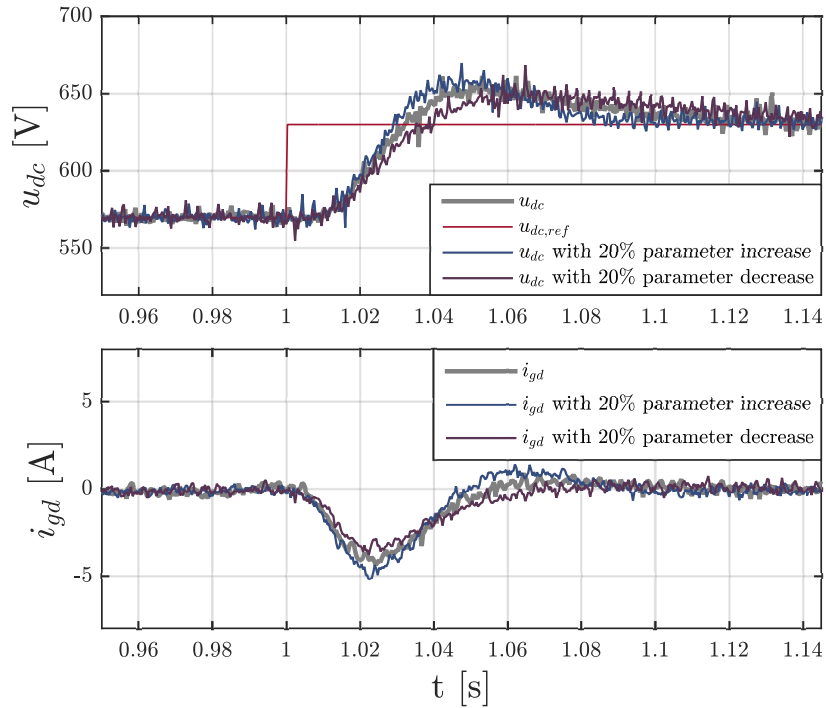


**Figure 5.19.** DC link response with respect to parameters changes.

$(a,b,c)$  to  $(d,q)$  coordinate system. Deteriorated PLL performance therefore also causes errors in the feedback  $(d,q)$  components, and as a consequence this is finally reflected as a higher THD. Application of a more elaborated PLL structure is expected to further improve the overall control performance, as discussed in [101,102].

Figure 5.18 shows the DC link step responses for various cases of chosen  $\omega_n$  that

determine the controller dynamic. The increase of  $\omega_n$  also increases system dynamics at the cost of larger overshoot/undershoot.

The robustness of the controller is also tested with respect to DC link parameters variation. This is performed by designing the controller based on the "wrong" DC link model parameters. Although the parameters are significantly changed, the system performance remains similar as shown in Fig.5.19.

The results show high robustness to grid conditions and  $\pm 20\%$  parameter inaccuracy for the proposed cascaded control with total harmonic distortion increase of only 0.4% at the grid connection point for 40% increase of the grid impedance.

## 5.8 Control of a battery system with variable efficiency

In the previous sections, microgrid components and their control algorithms are described. The goal of each component control is to achieve stable and efficient operation. In this section a control algorithm for microgrid optimal power flow problem is proposed, with emphasis on a variable battery storage system (BSS) efficiency.

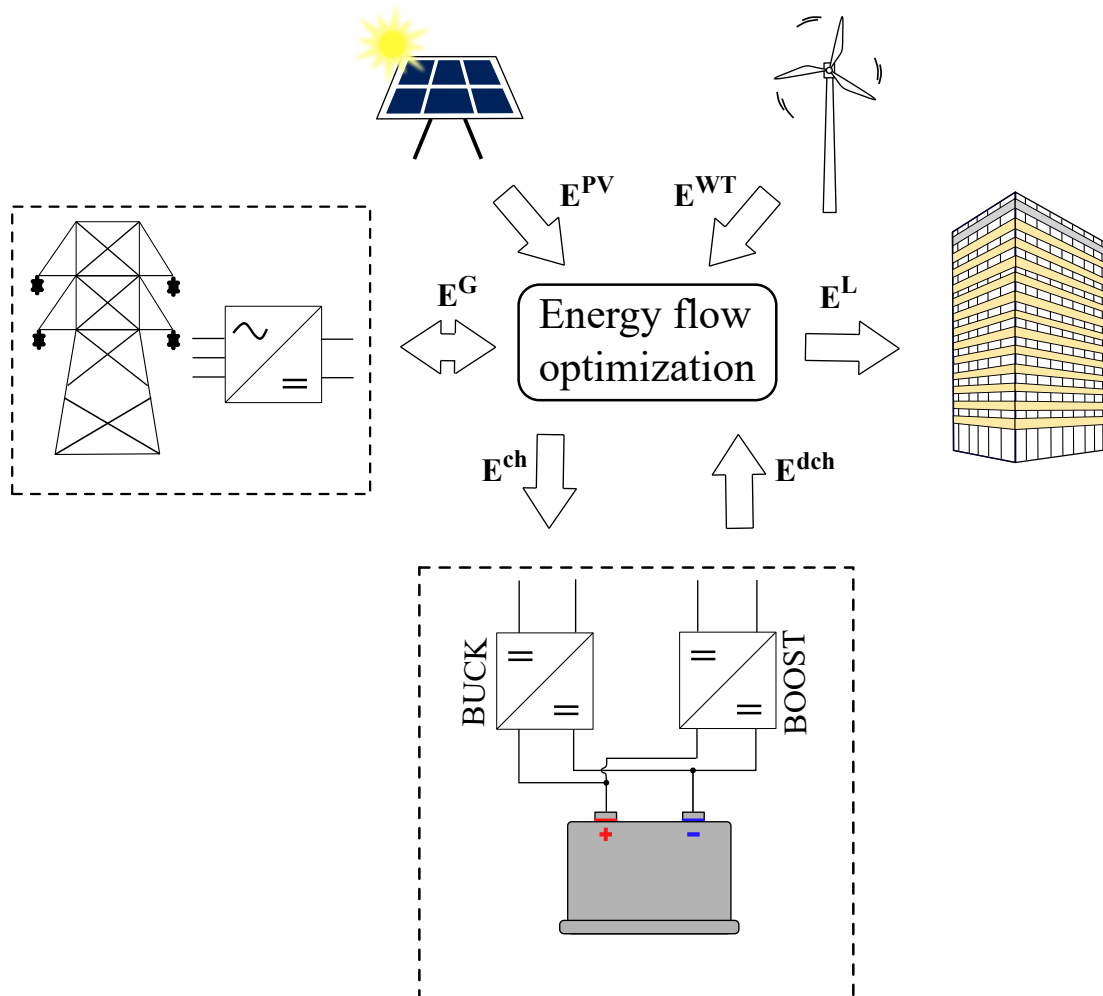


**Figure 5.20.** Microgrid topology with heterogeneous battery storage systems.



Most of developed advanced control approaches use models with constant battery efficiency and neglect energy losses of power conversions. However, converter efficiency is affected by conducting and switching losses of the electronic switches but also of normal operation requirements such as motherboard power consumption or cooling system with fans. Therefore, the converters efficiency curve is usually characterized with a distinct maximum [103]. In [104], constant converter efficiency is included in the optimization model. Power losses are estimated within a control loop with proportional-integral controller in [105], comparing reference power and the total power from renewable energy sources and storage units from the previous time step. In [14], the variable converter efficiency is averaged and respected by control as such. The variable converter efficiency is modelled in [106], and a genetic algorithm is used. However, the authors omit a more detailed description of the algorithm. The authors in [107] present a mixed-integer linear program (MILP) problem formulation for optimal power flow, which includes the variable converter efficiency. At each time step, the converter efficiency is updated by using the current measurements and is considered constant over the prediction horizon.

The microgrid power flow is depicted in Fig.5.20. In the microgrid model, production and load powers are used as known measured disturbances and the energy exchanged with the utility grid is determined by MPC. Battery storage system includes the battery and its corresponding power converter, and its dynamics is modelled via the state-of-energy (SOE), denoted with  $x$ . Variable efficiencies  $\eta$  of the storage system are included in order to achieve a more accurate model:

$$x(t) = x(t_0) - \frac{1}{C} \int_{t_0}^t \frac{1}{\eta_{\text{dch}}(P^{\text{dch}})} P^{\text{dch}}(\tau) d\tau - \frac{1}{C} \int_{t_0}^t \eta_{\text{ch}}(P^{\text{ch}}) P^{\text{ch}}(\tau) d\tau, \quad (5.34)$$

where  $C$  denotes the storage capacity in [Wh] and  $P$  denotes battery converter power at the microgrid side as shown in Fig.5.20. Powers and efficiencies are split into discharging and charging components, denoted respectively with 'dch' and 'ch' subscripts, since the observed system has separate discharging and charging converters. However, the same formulation applies for a bi-directional converter, thus avoiding the integer formulation of the problem [108]. Charging powers have a negative sign and discharging powers have a positive sign.

### 5.8.1 Linearization

The discrete-time model is obtained by describing the state of the continuous-time system at time instances  $t_k$ ,  $k \in \mathbb{Z}^+$ , where  $t_{k+1} = t_k + T_s$  and  $T_s$  is the sampling time. After the substitutions  $t_0 = t_k$  and  $t = t_{k+1}$  in (5.34) the discrete-time model of the battery storage system is formed:

$$x(t_{k+1}) = x(t_k) - \frac{1}{C} \int_{t_k}^{t_{k+1}} \frac{1}{\eta_{\text{dch}}(P^{\text{dch}})} P^{\text{dch}}(\tau) d\tau - \frac{1}{C} \int_{t_k}^{t_{k+1}} \eta_{\text{ch}}(P^{\text{ch}}) P^{\text{ch}}(\tau) d\tau. \quad (5.35)$$

This model is further simplified by assuming mean powers during the sampling interval  $P_k = P(t_k) = P(t), \forall t \in [t_k, t_{k+1})$  and the notations  $x_{k+1} = x(t_{k+1})$ ,  $x_k = x(t_k)$  are introduced:

$$x_{k+1} = x_k - \frac{1}{C} \frac{1}{\eta_{\text{dch}}(P_k^{\text{dch}})} P_k^{\text{dch}} T_s - \frac{1}{C} \eta_{\text{ch}}(P_k^{\text{ch}}) P_k^{\text{ch}} T_s. \quad (5.36)$$

The converter efficiency ( $\eta_{\text{conv}}$ ) curve is imported in the form of a look-up-table (LUT) from the chosen converter datasheet (depicted with orange and green circles in Fig. 5.21). Two converters, a XP Power QSB40024S48 boost converter and a Delta Electronics Q48SC12042NRDH buck converter (Table 5.2), are used in order to achieve a bidirectional energy flow. The battery efficiency is defined as power loss over the battery internal resistance for the nominal range of converter currents (first subfigure in Fig. 5.21) and combined with the converter efficiency data. The considered battery model with internal resistance value of  $R_{\text{int}} = 10 \text{ m}\Omega$  is taken from [37].

**Table 5.2.** Converter parameters.

Converter type	$V_{\text{in}}$	$V_{\text{out}}$	$P_{\text{out}}$
XP Power QSB40024S48	9-36 V	48 V	400 W
Delta Electronics Q48SC12042NRDH	36-75 V	8-13 V	500 W

Both curves are adjusted for the normalized input power range. The resulting data has a distinct maximum, and is fitted to an exponential curve (Fig. 5.21) which has proved to be more accurate than the higher order polynomials, and less complex than spline functions:

$$\begin{aligned} \eta(P_{\text{norm}}) &= a_{\text{pn}} e^{b_{\text{pn}} P_{\text{norm}}} + c_{\text{pn}} e^{d_{\text{pn}} P_{\text{norm}}}, \\ \frac{\partial \eta}{\partial P_{\text{norm}}} &= a_{\text{pn}} b_{\text{pn}} e^{b_{\text{pn}} P_{\text{norm}}} + c_{\text{pn}} d_{\text{pn}} e^{d_{\text{pn}} P_{\text{norm}}}. \end{aligned} \quad (5.37)$$

In the lower power ranges the switching losses are more prominent and greatly affect the efficiency. Therefore, for the power range below maximal efficiency, the mean power (given by the SLP control algorithm) is further modulated within the sampling period. The battery is charged/discharged with the maximal efficiency power during a shorter period, achieving maximal efficiency and the converter switches are inactive for the rest of the period. This is reflected in the implemented efficiency curve by holding maximal efficiency in the lower power range. The final curve is depicted with blue line in the lower two subfigures (Fig. 5.21) and it corresponds to the battery storage system overall efficiency in charging and discharging  $\eta_{\text{ch,BSS}}$  and  $\eta_{\text{dch,BSS}}$ , with taken into account the possibility of modulation of power converter operation within the sampling interval.

In both cases, the maximum of the approximated curve is between 40 % and 50 % of the nominal power, which corresponds to power ranges 160 W - 200 W for the boost converter and to power range 200 W - 250 W for the buck converter.

The model from (5.34) is rewritten with the substitution  $E_K^{\text{dch}} = P_k^{\text{dch}} T_s$ ,  $E_k^{\text{ch}} = P_k^{\text{ch}} T_s$  and then linearized around the point  $E_k^{\text{dch},0}$ ,  $E_k^{\text{ch},0}$ .

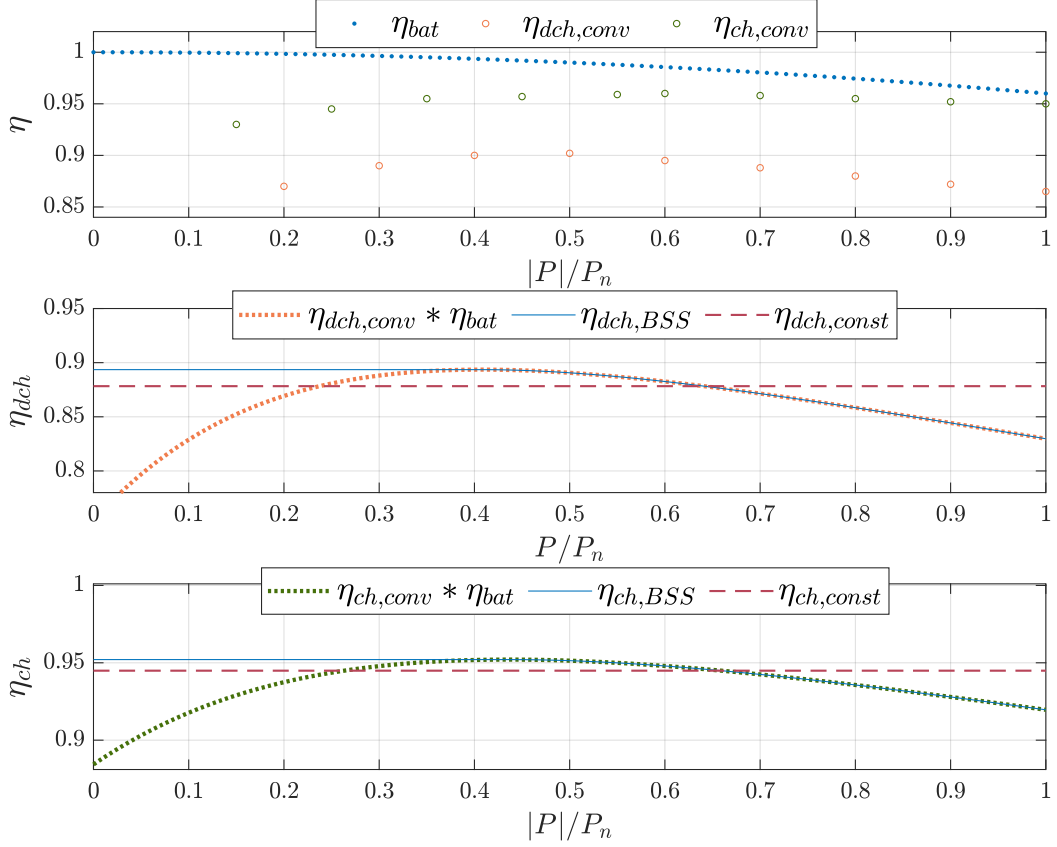


**Figure 5.21.** Battery storage system efficiency curves. The dashed lines represent instantaneous power and the full lines represent the mean power with the possibility of time modulation.

$$\left. \frac{\partial x_{k+1}}{\partial E_k^{\text{dch}}} \right|_{E_k^{\text{dch},0}} = -\frac{1}{C} \frac{1}{\eta(E_k^{\text{dch},0})} + \frac{1}{C} \frac{E_k^{\text{dch},0}}{\eta(E_k^{\text{dch},0})^2} \dot{\eta}(E_k^{\text{dch},0}), \quad (5.38)$$

$$\left. \frac{\partial x_{k+1}}{\partial E_k^{\text{ch}}} \right|_{E_k^{\text{ch},0}} = -\frac{1}{C} \left( \eta(E_k^{\text{ch},0}) + E_k^{\text{ch},0} \dot{\eta}(E_k^{\text{ch},0}) \right), \quad (5.39)$$

$$\Delta x_{k+1} = \Delta x_k + \left( \left. \frac{\partial x}{\partial E_k^{\text{dch}}} \right|_{E_k^{\text{dch},0}} \Delta E_k^{\text{dch}} + \left. \frac{\partial x}{\partial E_k^{\text{ch}}} \right|_{E_k^{\text{ch},0}} \Delta E_k^{\text{ch}} \right), \quad k = 0, \dots, N-1, \quad (5.40)$$

where  $E_k^{\text{dch}}$ ,  $E_k^{\text{ch}}$  are the mean discharging and charging energies within the sampling time and  $k$  is the time step. Using (5.40), and by introducing the vector  $\Delta u_k = [\Delta E_k^{\text{dch}} \ \Delta E_k^{\text{ch}}]^\top$  and notation with the operator  $\nabla_{u_k} := [\frac{\partial}{\partial E_k^{\text{dch}}} \ \frac{\partial}{\partial E_k^{\text{ch}}}]$  the linearized model around the point  $u_k^0 = [E_k^{\text{dch},0}, E_k^{\text{ch},0}]$  is defined:

$$\Delta x_{k+1} = \Delta x_k + \nabla_{u_k} x|_{u_k^0} \Delta u_k, \quad \Delta u_k = u_k - u_k^0,$$

$$\Delta x_{k+1} = x_{k+1} - x_{k+1}^0 \rightarrow x_{k+1} = x_{k+1}^0 + \Delta x_{k+1}. \quad (5.41)$$

The vector  $x_{k+1}^0$  is the SoE achieved by implementing the control input  $u_k^0$ .

### 5.8.2 Problem formulation

The objective of the considered microgrid operation is to achieve maximum economic gain:

$$J = \min_{u_k} \sum_{k=0}^{N-1} c_k E_k^G = \min_{\mathbf{u}} \mathbf{c} \mathbf{E}^G, \quad (5.42)$$

s.t.

$$E_k^{\text{dch}} \geq 0, \quad E_k^{\text{ch}} \leq 0, \quad (5.43)$$

$$E_k^G = E_k^L - E_k^{\text{res}} - 1_u u_k, \quad (5.44)$$

$$x_{\min} \leq x_k \leq x_{\max}, \quad (5.45)$$

$$u_{\min} \leq u_k \leq u_{\max}, \quad (5.46)$$

$$P_{\min}^G T_s \leq E_k^G \leq P_{\max}^G T_s, \quad (5.47)$$

where  $c_k$  is the energy price at each sampling interval, the maximum grid converter power is denoted with  $P_{\max}^G$  and  $P_{\min}^G$  and  $u_{\max}$  and  $u_{\min}$  represent the maximum battery converter energy. The maximum and minimum SoE of the battery are represented with  $x_{\max}$  and  $x_{\min}$ . For MPC implementation, the constraints are written in a matrix form over the horizon  $N$ . The linearized model (5.41) over the horizon  $N$  thus becomes:

$$\Delta \mathbf{x} = \mathbf{A}_d \Delta \mathbf{x}_0 + \mathbf{B}_d \Delta \mathbf{u}, \quad (5.48)$$

$$\mathbf{x} = \begin{bmatrix} \Delta x_1 \\ \Delta x_2 \\ \vdots \\ \Delta x_N \end{bmatrix}, \quad \Delta \mathbf{u} = \begin{bmatrix} \Delta u_0 \\ \Delta u_1 \\ \vdots \\ \Delta u_{N-1} \end{bmatrix},$$

$$\mathbf{A}_d = \begin{bmatrix} 1 \\ \vdots \\ 1 \end{bmatrix},$$

$$\mathbf{B_d} = \begin{bmatrix} \nabla_{u_0} x|_{u_0^0} & \mathbf{0} & \cdots & \mathbf{0} \\ \nabla_{u_0} x|_{u_0^0} & \nabla_{u_1} x|_{u_1^0} & \cdots & \mathbf{0} \\ \vdots & \ddots & \ddots & \vdots \\ \nabla_{u_0} x|_{u_0^0} & \cdots & \cdots & \nabla_{u_{N-1}} x|_{u_{N-1}^0} \end{bmatrix},$$

where  $\mathbf{x}$  and  $\mathbf{u}$  are the state and input vectors stacked over the prediction horizon.

The constraints from (5.43), rewritten in matrix form become:

$$\mathbf{I_e u} \leq \mathbf{B_e}, \quad (5.49)$$

$$\mathbf{i_e} = \begin{bmatrix} -1 & 0 \\ 0 & 1 \end{bmatrix}, \quad \mathbf{I_e} = \begin{bmatrix} \mathbf{i_e} & \mathbf{0} & \cdots & \mathbf{0} \\ \mathbf{0} & \mathbf{i_e} & \cdots & \mathbf{0} \\ \vdots & \ddots & \ddots & \vdots \\ \mathbf{0} & \cdots & \cdots & \mathbf{i_e} \end{bmatrix}, \quad (5.50)$$

$$\mathbf{b_e} = \begin{bmatrix} 0 \\ 0 \end{bmatrix}, \quad \mathbf{B_e} = \begin{bmatrix} \mathbf{b_e} \\ \vdots \\ \mathbf{b_e} \end{bmatrix}. \quad (5.51)$$

The energy balance equation from (5.44) is rewritten as:

$$-\mathbf{I E^G} + \mathbf{A_g u} \leq \mathbf{B_g} \quad (5.52)$$

$$\mathbf{A_g} = -\mathbf{I_u}, \quad \mathbf{B_g} = (\mathbf{E^{res}} - \mathbf{E^L}), \quad (5.53)$$

$$\mathbf{i_u} = \begin{bmatrix} 1 & 1 \end{bmatrix}, \quad \mathbf{I_u} = \begin{bmatrix} \mathbf{i_u} & \mathbf{0} & \cdots & \mathbf{0} \\ \mathbf{0} & \mathbf{i_u} & \cdots & \mathbf{0} \\ \vdots & \ddots & \ddots & \vdots \\ \mathbf{0} & \cdots & \cdots & \mathbf{i_u} \end{bmatrix}, \quad (5.54)$$

where  $\mathbf{E^{res}}$  and  $\mathbf{E^L}$  are the renewables production and load stacked vectors. The SoE constraint from (5.45) becomes:

$$\mathbf{A_x u} \leq \mathbf{B_x}, \quad (5.55)$$

$$\mathbf{A_x} = \begin{bmatrix} \mathbf{B_d} \\ -\mathbf{B_d} \end{bmatrix}, \quad \mathbf{B_x} = \begin{bmatrix} \mathbf{x_{max}} - \mathbf{x}^0 + \mathbf{B_d u}^0 \\ -\mathbf{x_{min}} + \mathbf{x}^0 - \mathbf{B_d u}^0 \end{bmatrix}, \quad (5.56)$$

where  $\mathbf{u}^0$  is the initial input vector and  $\mathbf{x}^0$  is the vector of SoE, achieved by implementing  $\mathbf{u}^0$ . The grid and battery converter constraints from (5.46) and (5.47) are rewritten as follows:

$$\mathbf{A}_u \mathbf{u} \leq \mathbf{B}_u, \quad (5.57)$$

$$\mathbf{A}_u = \begin{bmatrix} \mathbf{I} \\ -\mathbf{I} \end{bmatrix}, \quad \mathbf{B}_u = \begin{bmatrix} \mathbf{u}_{\max} \\ -\mathbf{u}_{\min} \end{bmatrix}, \quad (5.58)$$

$$\mathbf{A}_p \mathbf{u} \leq \mathbf{B}_p, \quad (5.59)$$

$$\mathbf{A}_p = \begin{bmatrix} -\mathbf{I}_u \\ \mathbf{I}_u \end{bmatrix}, \quad \mathbf{B}_p = \begin{bmatrix} \mathbf{P}_{\max}^G T_s - \mathbf{E}^L + \mathbf{E}^{\text{res}} \\ -\mathbf{P}_{\max}^G T_s + \mathbf{E}^L - \mathbf{E}^{\text{res}} \end{bmatrix}, \quad (5.60)$$

where  $\mathbf{P}_{\max}^G$ ,  $\mathbf{u}_{\max}$  and  $\mathbf{u}_{\min}$  denote the maximum grid converter power and the maximum battery converter current over the prediction horizon. An additional constraint is added to ensure that the SLP algorithm stays in the neighbourhood of the initial point in every iteration:

$$-\Delta \leq \mathbf{u} - \mathbf{u}^0 \leq \Delta \Rightarrow \mathbf{A}_\Delta \mathbf{u} \leq \mathbf{B}_\Delta, \quad (5.61)$$

$$\mathbf{A}_\Delta = \begin{bmatrix} \mathbf{I} & \mathbf{0} \\ \mathbf{0} & -\mathbf{I} \end{bmatrix}, \quad \mathbf{B}_\Delta = \begin{bmatrix} \mathbf{u}^0 + \Delta \\ -\mathbf{u}^0 + \Delta \end{bmatrix}, \quad (5.62)$$

where  $\Delta$  determines the maximum deviation of the solution vector from the initial point at each iteration.

The SLP algorithm is shown in Fig.5.22. At each time step, a control vector  $u_1^0$  is chosen as an initial point and the problem is linearized. The algorithm solves the problem from (5.42) and then replaces, at each iteration, the control vector  $u_1^0$  with the current problem solution  $u_i^*$  and linearizes around it, until the exit condition is reached. For this implementation, the comparison of average cost function values is chosen as the exit condition. The algorithm calculates the average value of the cost function in the last three iterations and compares it to the average calculated in the previous iteration in order to determine if the exit condition  $J_{\text{avg},i} - J_{\text{avg},i-1} < \varepsilon$  is reached, where  $\varepsilon$  is the chosen convergence tolerance.

### 5.8.3 Simulation results

The control algorithm is implemented in MATLAB and several 7-day period simulations are performed. The battery system model, depicted in Fig.5.1, is a combination of two converters: XP POWER DC/DC boost converter and Delta Electronics buck converter

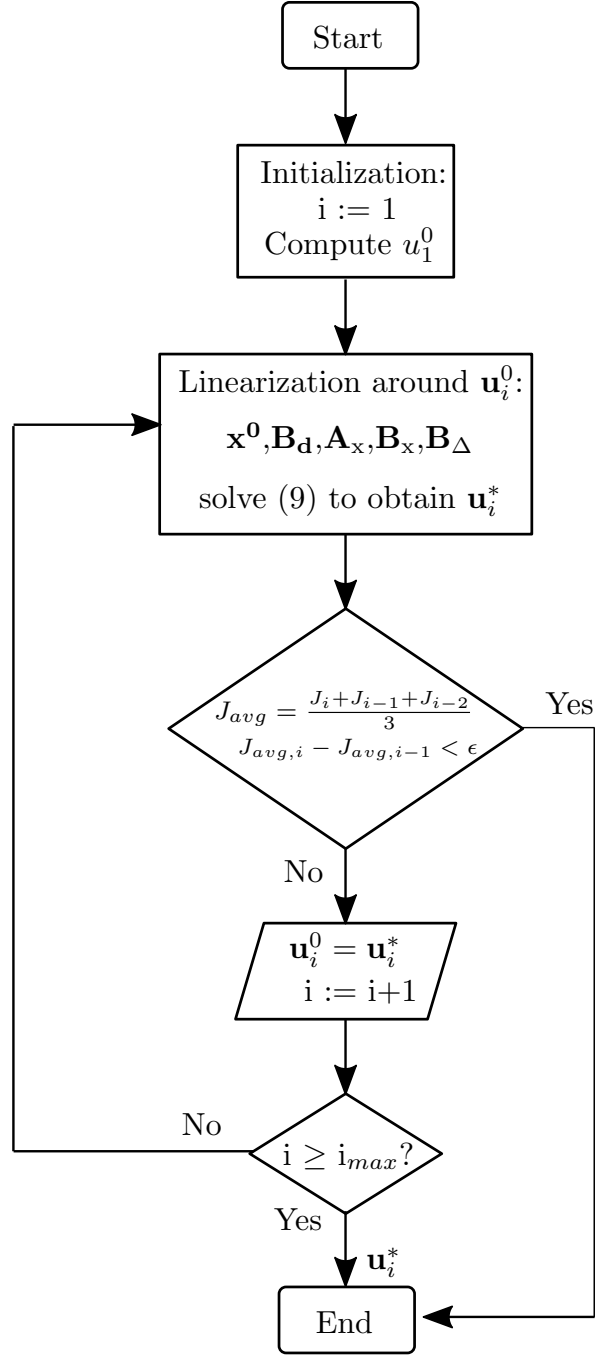


**Figure 5.22.** Derived SLP algorithm.

(Table 5.2) in order to achieve a bidirectional energy storage topology. The efficiency curves include battery and converter variable efficiency as shown in Fig. 5.21.

The proposed model is compared to a common approach with constant charging and discharging efficiencies, i.e.  $\eta(P^{\text{dch}}) = \eta_{\text{dch}}$ ,  $\eta(P^{\text{ch}}) = \eta_{\text{ch}}$ . The efficiency curves from Fig. 5.21 are approximated with a constant and the best approximation (using least-square-error) is chosen:  $\eta_{\text{dch}} = 87.83\%$ ,  $\eta_{\text{ch}} = 94.49\%$  (dashed red lines in Fig. 5.21). Therefore, charging equation (5.34) takes the linear form.

The discretization time is  $T_s = 10$  min which corresponds to the production and load

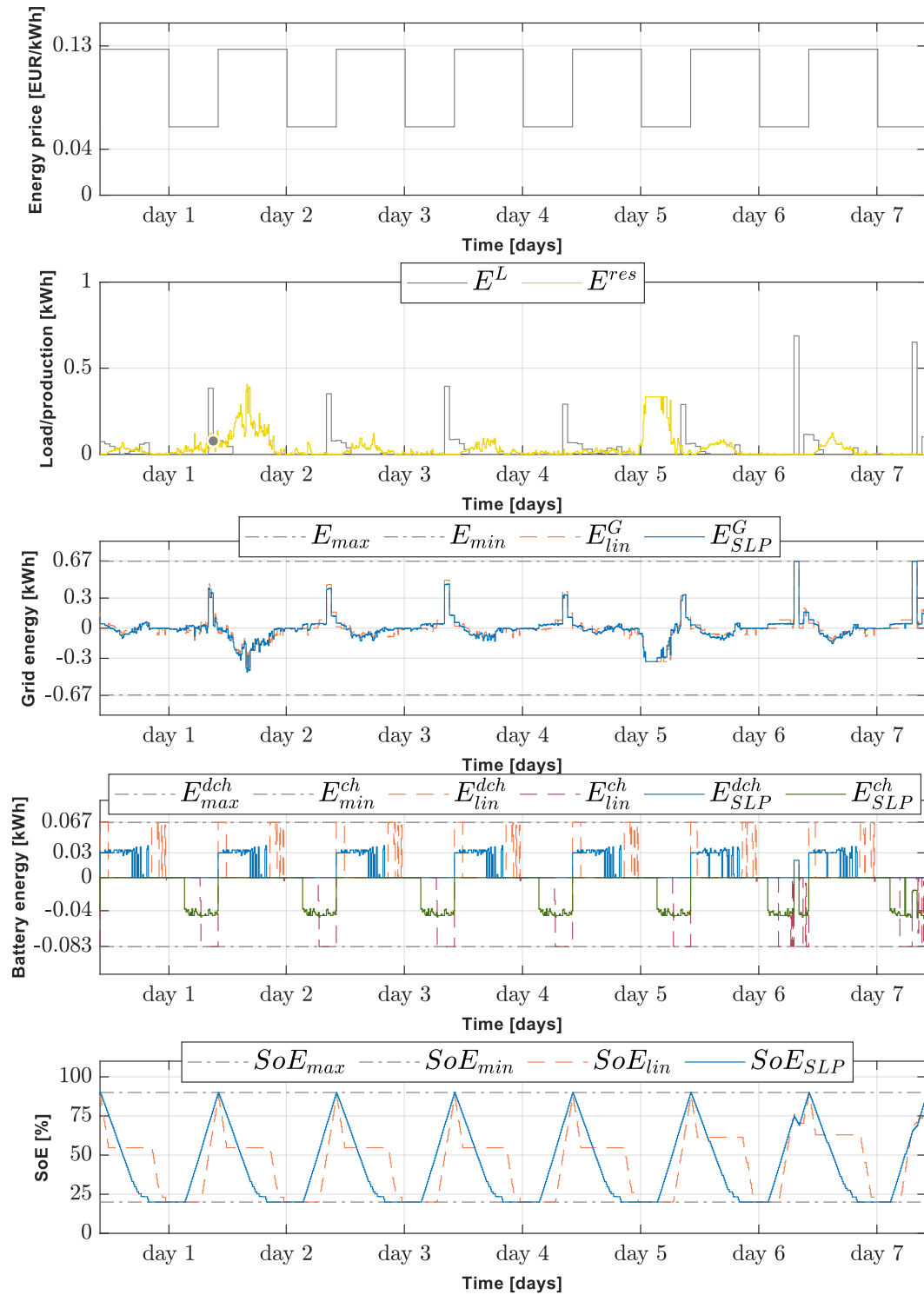


**Figure 5.23.** Comparison of MPCs 7-day operation with constant (linear) and variable efficiencies (SLP).

energy data acquisition period. The prediction horizon for both models is  $N = 144$  in order to capture both tariffs of the considered two-tariff energy pricing model. In simulations, receding horizon control (RHC) is implemented, where the optimization problem from (5.42) is solved every 10 min and only the first control input is applied to the nonlinear storage system model. In Fig.5.23, grid energy exchange, battery charging/discharging



energies and the battery SoE are shown over a 7-day period. The orange dashed line denotes the responses obtained by MPC that uses a linear model and the blue line represents the responses obtained with MPC that uses the introduced model with variable efficiency. The control inputs obtained with the latter control strategy clearly follow the efficiency curve since all the charging/discharging energies are lower than the nominal. Moreover, the charging and discharging mean powers are mostly kept between  $0.4 - 0.5P_n$ , which is around the maximum of the approximated curve. All the simulations were done with the full nonlinear model and the results are summarized in Table 5.3. The table compares the total cost and the total charging/discharging battery energies over the 7-day period. The initial condition  $x_0$  is the same for both models. At the end of the observed simulation time, both models charge the batteries to maximum allowed percentage (90%). In all three categories, the SLP algorithm shows better results with higher profit, less energy used for charging, and more energy discharged and injected into the grid. The savings achieved with the variable efficiency are approximately 7% over a 7-day period, however these savings come with higher computational cost since the average computation time of a time step  $k$  is 0.03 s for the linear model and 0.78 s for the SLP model on a 3.40 GHz machine with 8 GB RAM. The savings would increase more in such conditions where the storage system is frequently charged/discharged, especially if higher/nominal powers are thereby demanded. Systems with older batteries (higher internal resistance) would also benefit from the SLP algorithm because of a higher efficiency drop with higher currents (powers) as is shown in Fig. 5.24. The internal resistance is increased to  $R_{\text{int}} = 20 \text{ m}\Omega$  and the same simulation scenario is repeated. The SLP algorithm again follows the maximum of the approximated curve (Fig. 5.25) which results in approximately 11% savings over the 7-day period. The results of this model are summarized in Table 5.4.

**Table 5.3.** Charging and discharging energies and profit.

MPC algorithm	$\sum E_{\text{ch}}$ [kWh]	$\sum E_{\text{dch}}$ [kWh]	$\sum \text{cost}$ [€]
Linear, 7 days	-12.71	9.72	-1.56
SLP, 7 days	-12.53	10.63	-1.69

**Table 5.4.** Charging and discharging energies and profit for storage system with battery internal resistance  $R_{\text{int}} = 20 \text{ m}\Omega$ .

MPC algorithm	$\sum E_{\text{ch}}$ [kWh]	$\sum E_{\text{dch}}$ [kWh]	$\sum \text{cost}$ [€]
Linear, 7 days	-12.96	9.17	-1.47
SLP, 7 days	-12.64	10.55	-1.67

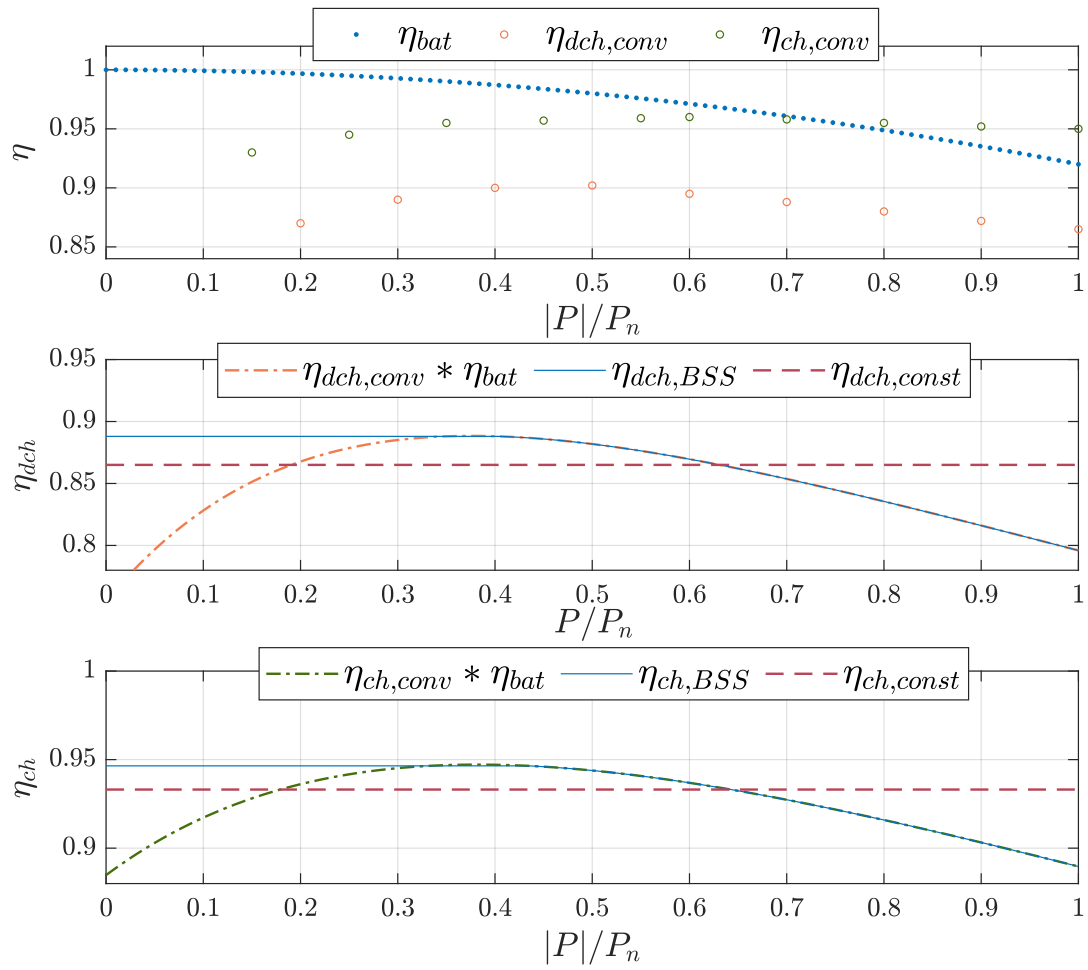


**Figure 5.24.** Battery storage system efficiency curves with internal resistance  $R_{\text{int}} = 20 \text{ m}\Omega$ .

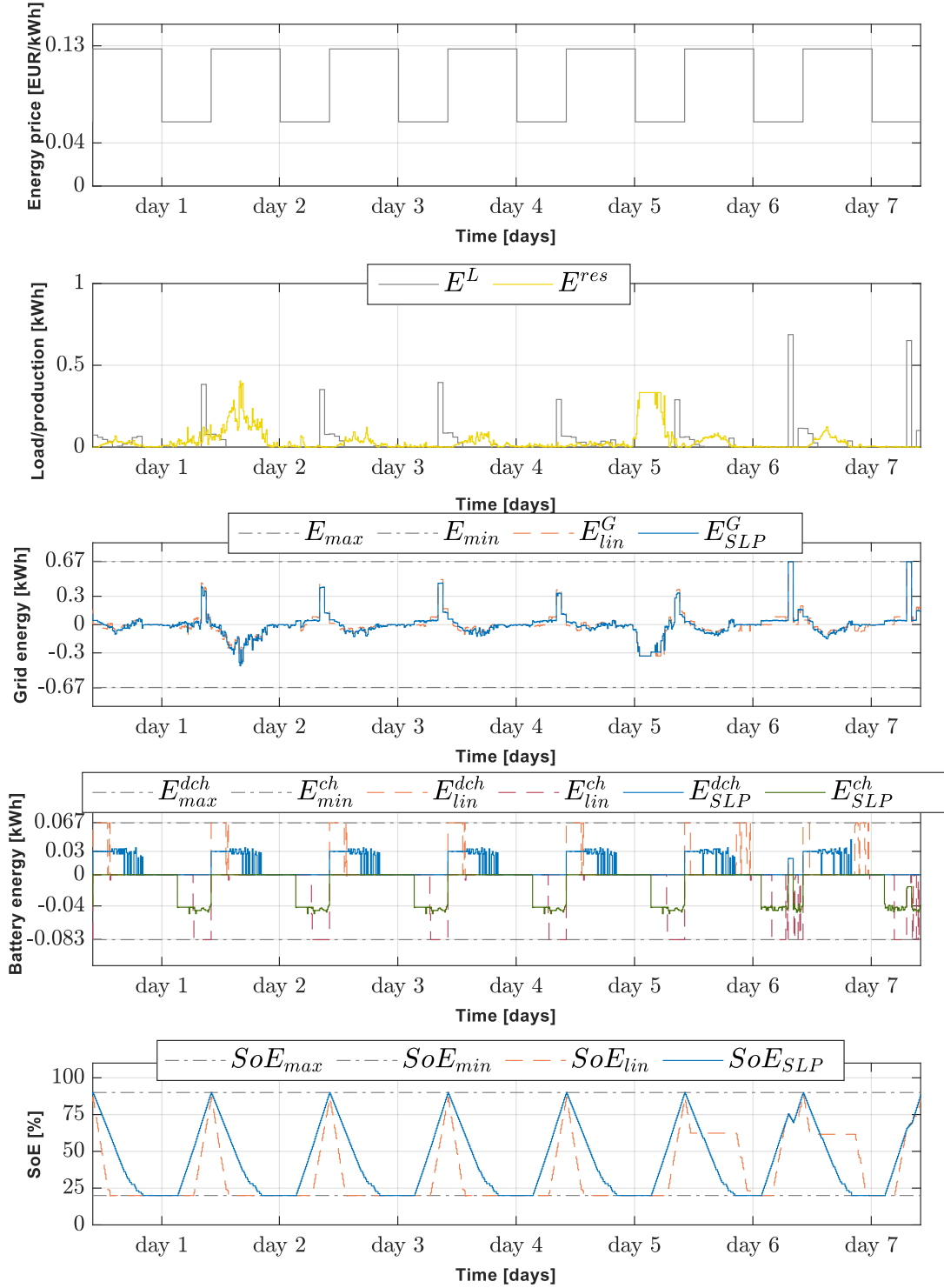


**Figure 5.25.** Comparison of MPCs 7-day operation with constant (linear) and variable efficiencies (SLP), with battery internal resistance  $R_{int} = 20 \text{ m}\Omega$ .

## 5.9 MPC of a microgrid with $n$ battery storage systems

In this section, the microgrid power flow optimization algorithm is modified in order to include more than one battery storage system (Fig.5.26). The cost function and the constraints are defined as in (5.47):

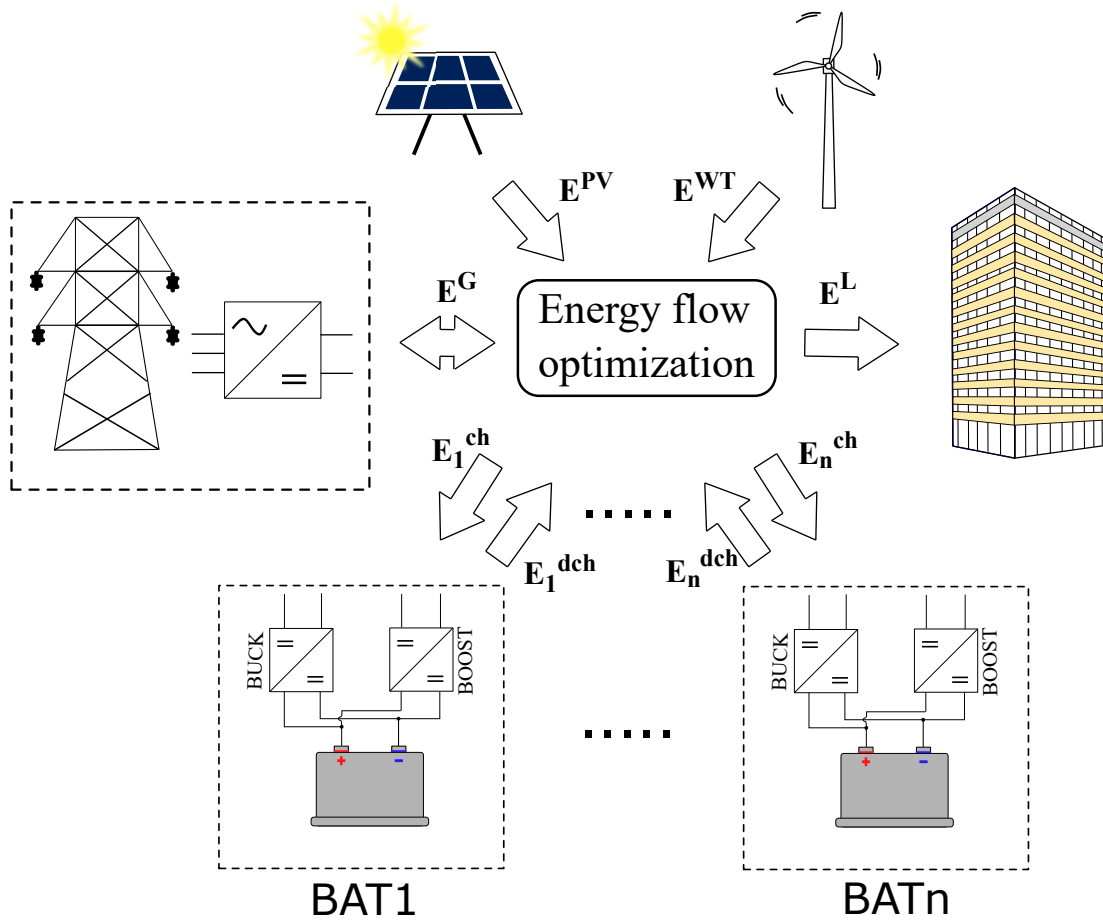


**Figure 5.26.** Microgrid topology with heterogeneous battery storage systems.

$$J = \min_{u_k^a} \sum_{k=0}^{N-1} c_k E_k^G = \min_{\mathbf{u}^a} \mathbf{c} \mathbf{E}^G, \quad (5.63)$$

s.t.

$$E_{j,k}^{\text{dch}} \geq 0, \quad E_{j,k}^{\text{ch}} \leq 0, \quad j = 1, \dots, n_b, \quad (5.64)$$

$$E_k^G = E_k^L - E_k^{\text{res}} - 1_u u_k^a, \quad (5.65)$$

$$x_{\min} \leq x_k^a \leq x_{\max}, \quad (5.66)$$

$$u_{\min} \leq u_k^a \leq u_{\max}, \quad (5.67)$$

$$-\Delta \leq u_k^a \leq \Delta, \quad (5.68)$$

$$P_{\min}^G T_s \leq E_k^G \leq P_{\max}^G T_s, \quad (5.69)$$

where  $x_k^a = [x_{1,k}, \dots, x_{n_b,k}]^\top$  and  $u_k^a = [u_{1,k}, \dots, u_{n_b,k}]^\top$  are augmented state and control vectors and  $n_b$  is the number of battery storage systems in the observed microgrid. The  $j$ -th control vector contains the discharging and the charging energies  $u_{j,k} = [E_{j,k}^{\text{dch}} \ E_{j,k}^{\text{ch}}]^\top$  as defined in section 5.9. The storage systems energy model from The constraints from (5.48) and the constraints from (5.49) are rewritten as:

$$\mathbf{A}_d^a = \begin{bmatrix} \mathbf{A}_{d1} & \cdots & \mathbf{0} \\ \vdots & \ddots & \vdots \\ \mathbf{0} & \cdots & \mathbf{A}_{dn} \end{bmatrix}, \quad \mathbf{B}_d^a = \begin{bmatrix} \mathbf{B}_{d1} & \cdots & \mathbf{0} \\ \vdots & \ddots & \vdots \\ \mathbf{0} & \cdots & \mathbf{B}_{dn} \end{bmatrix}. \quad (5.70)$$

$$\mathbf{I}_e^a = \begin{bmatrix} \mathbf{I}_e & \cdots & \mathbf{0} \\ \vdots & \ddots & \vdots \\ \mathbf{0} & \cdots & \mathbf{I}_e \end{bmatrix}, \quad \mathbf{B}_e^a = \begin{bmatrix} \mathbf{B}_e \\ \vdots \\ \mathbf{B}_e \end{bmatrix}, \quad (5.71)$$

In the energy balance constraint (Eq. (5.53)), only the matrix  $A_g$  is augmented:

$$\mathbf{A}_g^a = [\mathbf{A}_g \quad \cdots \quad \mathbf{A}_g], \quad (5.72)$$

The SOE and battery and grid converter constraints from Eqs. (5.55) - (5.59) are also augmented:

$$\mathbf{A}_x^a = \begin{bmatrix} \mathbf{A}_{x1} & \cdots & \mathbf{0} \\ \vdots & \ddots & \vdots \\ \mathbf{0} & \cdots & \mathbf{A}_{xn} \end{bmatrix}, \quad \mathbf{B}_x^a = \begin{bmatrix} \mathbf{B}_{x1} \\ \vdots \\ \mathbf{B}_{xn} \end{bmatrix}, \quad (5.73)$$

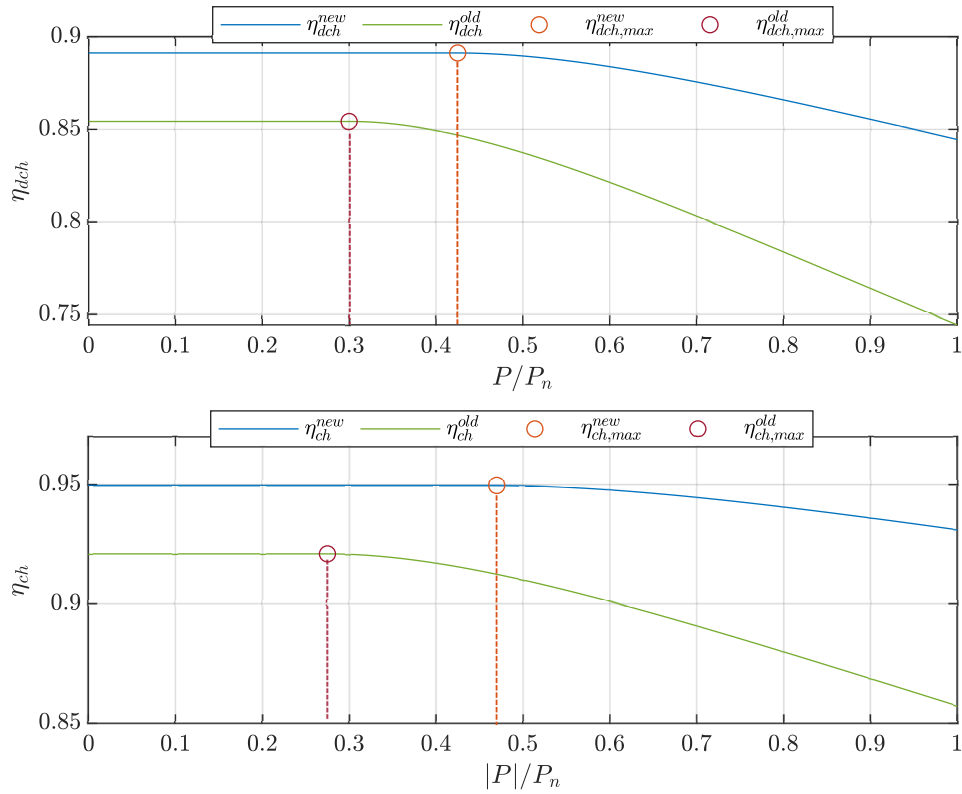
$$\mathbf{A}_u^a = \begin{bmatrix} \mathbf{A}_u & \cdots & \mathbf{0} \\ \vdots & \ddots & \vdots \\ \mathbf{0} & \cdots & \mathbf{A}_u \end{bmatrix}, \quad \mathbf{B}_u^a = \begin{bmatrix} \mathbf{B}_{u1} \\ \vdots \\ \mathbf{B}_{un} \end{bmatrix}, \quad (5.74)$$

$$\mathbf{A}_p^a = [\mathbf{A}_p \quad \cdots \quad \mathbf{A}_p], \quad \mathbf{B}_p^a = \begin{bmatrix} \mathbf{B}_{p1} \\ \vdots \\ \mathbf{B}_{pn} \end{bmatrix}, \quad (5.75)$$

The constraint on the control input change (5.62) for the SLP algorithm is rewritten as:

$$\mathbf{A}_\Delta^a = \begin{bmatrix} \mathbf{A}_\Delta & \cdots & \mathbf{0} \\ \vdots & \ddots & \vdots \\ \mathbf{0} & \cdots & \mathbf{A}_\Delta \end{bmatrix}, \quad \mathbf{B}_\Delta^a = \begin{bmatrix} \mathbf{B}_{\Delta 1} \\ \vdots \\ \mathbf{B}_{\Delta n} \end{bmatrix}. \quad (5.76)$$

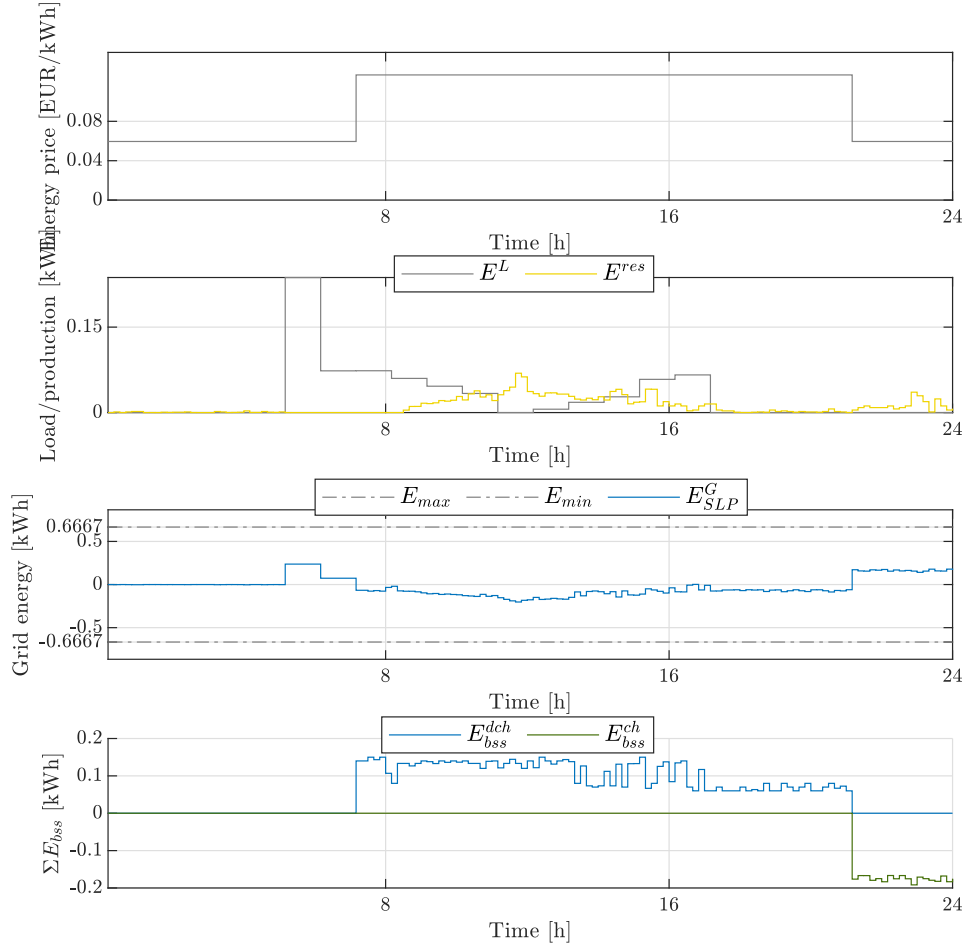
The algorithm was tested on the same microgrid topology from Section 5.8. with additional battery systems. In the simulation scenario, the microgrid consists of six BSSs - three storage systems with a "new" battery and three with an "old" battery. The new



**Figure 5.27.** Heterogeneous battery storage system efficiency curves, variable battery model.

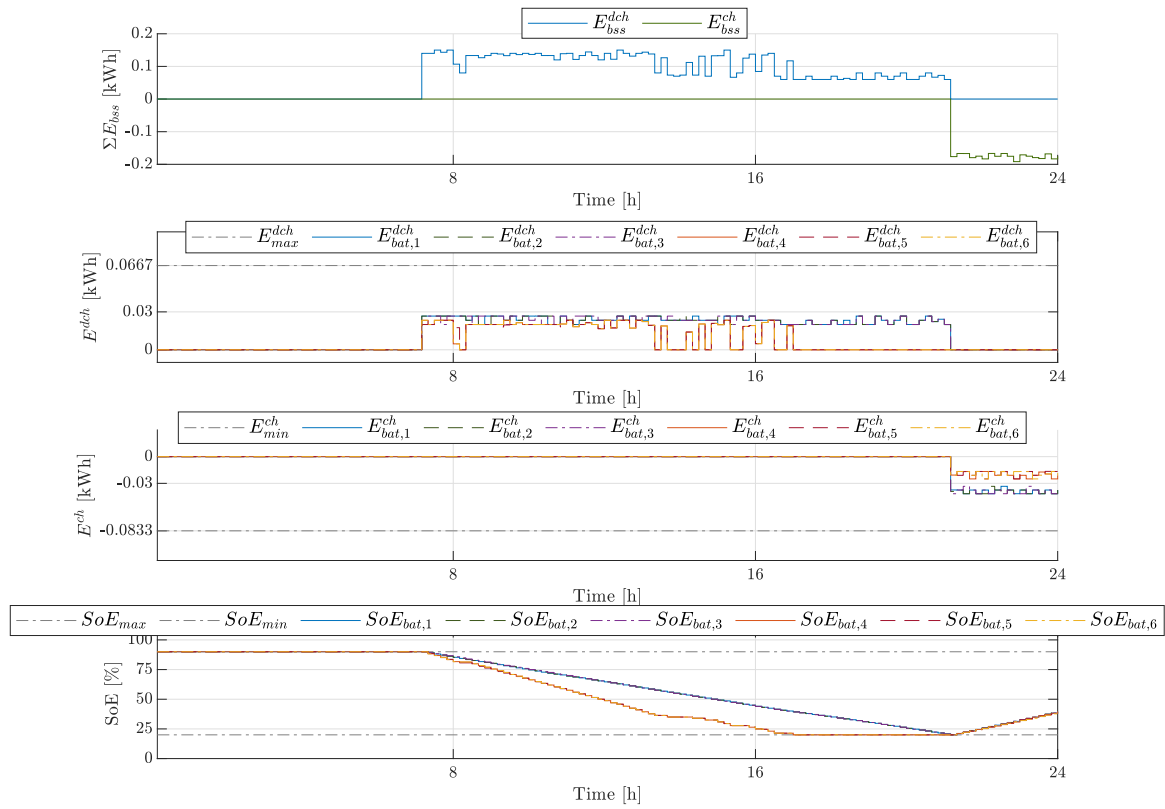
battery efficiency curve is obtained from the model identified in Chapter 3. For simplicity reasons, at this point, the efficiency curve is considered constant with respect to SOC and the curve for SOC = 100% is used in this simulation scenario. Battery ageing is reflected in the capacity fade and internal resistance rise, therefore the old BSS is modelled with 50 % less capacity and 10 times higher internal resistance. The drastic difference in ohmic resistances is chosen in order to achieve a noticeable difference in efficiency curves, which would simplify the evaluation of the optimization results. The charging and discharging efficiencies are depicted in Fig.5.27. The maximum of the discharging curve for the new BSS is achieved at around  $0.425P_n$  and for the old BSS at  $0.354P_n$ . The difference between charging curves is even bigger, decreasing from  $0.47P_n$  to  $0.34P_n$ . A 1-day operation of a microgrid with heterogeneous BSSs is shown in Figs.5.28 and 5.29. At the beginning of simulation, all batteries are at 90% SOE which is the upper constraint. From the cumulative BSS energy exchange subfigure and the charging energy subfigure (Subfigures 1 and 3 on Fig.5.29) we observe that all the BSSs are charging at the same time while the energy price is low and discharging during high energy price period. The control algorithm charges the batteries for a longer time with lower energies, as expected. In this scenario, with heterogeneous battery systems, we observe that the charging and discharging energies of the old battery systems (BSS4-BSS6) are lower corresponding with their efficiency curves. Also, they are charged/discharged more quickly than the new BSSs, as depicted in the SoE subfigure of Fig.5.29). These results show that the algorithm successfully tracks

the maximum efficiency of each BSS. The profit of the 1-day heterogeneous BSS microgrid operation is approximately 0.9 €, and the average time step execution time is 12.17 s.

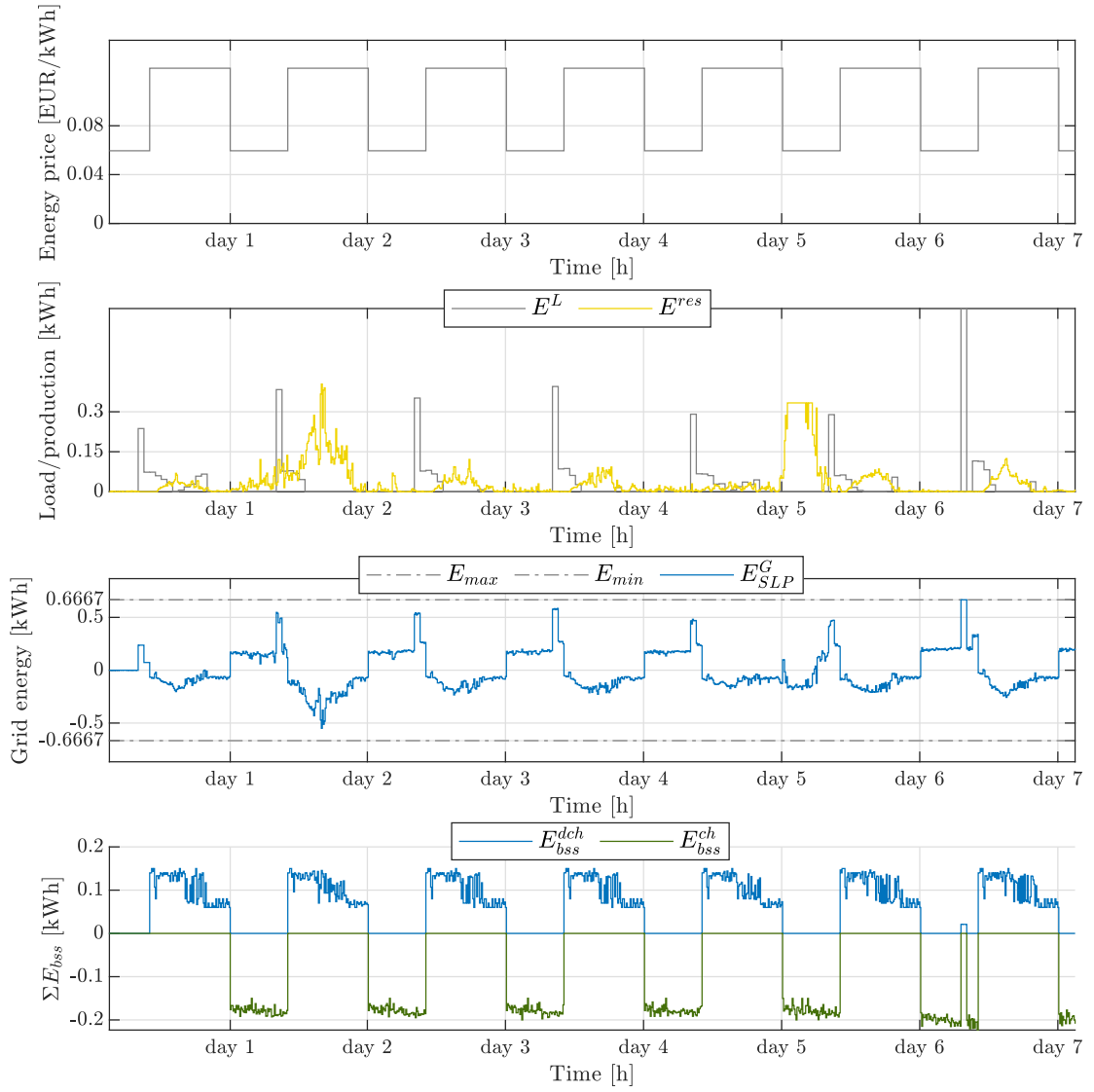


**Figure 5.28.** Microgrid 1-day operation with 6 BSS, part 1.

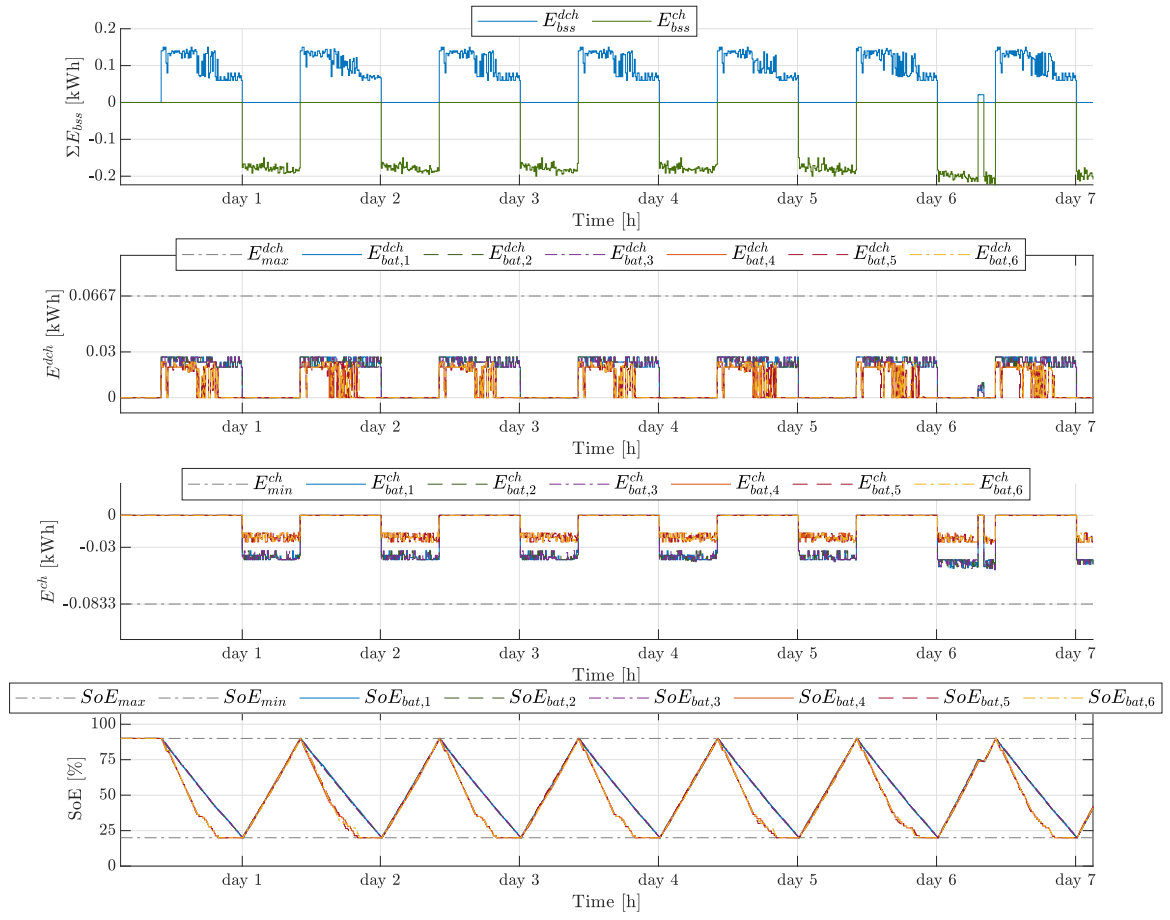
The same system is simulated over a 7-day period achieving the profit of 5.1 €. The average execution time of the algorithm at each time step is 12.53 s, which is slightly longer than the execution time in the 1-day scenario, it is still significantly smaller than 10 minutes which is the sample time of the system. The system behavior is consistent throughout the whole simulation.

**Figure 5.29.** Microgrid 1-day operation with 6 BSS, part 2.





**Figure 5.30.** Microgrid 7-day operation with 6 BSS, part 1.

**Figure 5.31.** Microgrid 7-day operation with 6 BSS, part 2.



---

## Conclusion

In this thesis, a control algorithm of a microgrid battery storage system (BSS) is proposed. The control algorithm is separated into two levels, microgrid and BSS, with the mutual goal of efficient system operation. Microgrid components and their optimal control strategies are described offering insight into how each component contributes to the operation of the whole system. A stability problem with the grid converter, the key component in charge of the stability of the whole microgrid, was detected. The conventional and modern DC link controllers may become unstable due to varying grid conditions. Also, the varying operating point of the converter may also be the cause of instability. Therefore, effort was invested into designing a controller robust to varying operating conditions. A thorough robustness analysis as well as experimental verification proved the efficacy of the proposed controller design method. Further research of the microgrid components showed continuous neglecting of the battery and converter variable efficiencies in control algorithms. At the BSS level, a variable parameter battery model was introduced in order to achieve efficient battery charging or discharging. The model in the form of state of charge (SOC) interval dependent look-up-tables (LUTs) was obtained using least-square parameter identification. This representation was chosen because it offers enough information for the control algorithm without adding complexity. Three variations of the least-square method were used during the identification process, each having their advantages and disadvantages. On both levels, the inclusion of the variable battery model resulted in improved system operation. The results of the BSS control algorithm with the variable model compared with the constant model algorithm show improvement in model accuracy and residual SOC. At the microgrid level, the power flow optimization problem is solved. The BSS model combines power dependent converter efficiency and the battery efficiency obtained from the variable model. This model is included in the microgrid optimization flow and compared to the conventional constant efficiency control. In order to achieve the maximum profit, the algorithm tracks the BSS maximal power point which results in more efficient system operation and decreased stress on the components. Future work will be focused on accurate SOC and SOE estimation,

as a prerequisite for closed loop BSS control. At the microgrid level, with the SOC and SOE information, the whole SOC-dependent efficiency model could be included leading to even more profitable microgrid operation.

The following scientific contributions are the result of the thesis:

- Method for model identification of lithium-ion battery storage systems with variable converter and battery efficiencies, suitable for application in model predictive control.
- Model predictive control of battery charging and discharging current considering the identified nonlinear mathematical model of a battery storage system for achieving its maximum efficiency.
- Model predictive control of a microgrid with heterogeneous battery storage systems for achieving its cost-optimal operation.



- [8]Li Wang, Yujie Wang, Chang Liu, Duo Yang, and Zonghai Chen. A power distribution strategy for hybrid energy storage system using adaptive model predictive control. *IEEE Transactions on Power Electronics*, pages 5897–5906, 2020.
- [9]Guodong Liu, Yan Xu, and Kevin Tomsovic. Bidding strategy for microgrid in day-ahead market based on hybrid stochastic/robust optimization. *IEEE Transactions on Smart Grid*, pages 227–237, 2016.
- [10]Jianqiang Liu, Xiaoguang Huang, and Zuyi Li. Multi-time scale optimal power flow strategy for medium-voltage dc power grid considering different operation modes. *Journal of Modern Power Systems and Clean Energy*, pages 46–54, 2020.
- [11]Cuo Zhang, Yan Xu, Zhao Yang Dong, and Jin Ma. Robust operation of microgrids via two-stage coordinated energy storage and direct load control. *IEEE Transactions on Power Systems*, pages 2858–2868, 2017.
- [12]Matthew T. Lawder, Bharatkumar Suthar, Paul W. C. Northrop, Sumitava De, C. Michael Hoff, Olivia Leitermann, Mariesa L. Crow, Shriram Santhanagopalan, and Venkat R. Subramanian. Battery energy storage system (BESS) and battery management system (BMS) for grid-scale applications. *Proceedings of the IEEE*, pages 1014–1030, 2014.
- [13]Philipp Fortenbacher, Johanna L. Mathieu, and G öran Andersson. Modeling, identification, and optimal control of batteries for power system applications. In *2014 Power Systems Computation Conference*, pages 1–7, 2014.
- [14]Philipp Fortenbacher, Johanna L. Mathieu, and G öran Andersson. Modeling and optimal operation of distributed battery storage in low voltage grids. *IEEE Transactions on Power Systems*, pages 4340–4350, 2017.
- [15]Valentin A. Boicea. Energy storage technologies: The past and the present. *Proceedings of the IEEE*, 102(11):1777–1794, 2014.
- [16]Subrat Sahoo and Pascal Timmann. Energy storage technologies for modern power systems: A detailed analysis of functionalities, potentials, and impacts. *IEEE Access*, 11:49689–49729, 2023.
- [17]Tatiane S. Costa, Maria de Fátima Rosolem, João Lucas de S. Silva, and Marcelo G. Villalva. An overview of electrochemical batteries for ESS applied to PV systems connected to the grid. In *2021 14th IEEE International Conference on Industry Applications (INDUSCON)*, pages 1392–1399, 2021.
- [18]Wenchao Tian, Mengjuan Li, Jiahao Niu, Wenhua Li, and Jing Shi. The research progress and comparisons between lithium-ion battery and sodium ion battery. In

- 2019 *IEEE 19th International Conference on Nanotechnology (IEEE-NANO)*, pages 313–318, 2019.
- [19] J. Mitali, S. Dhinakaran, and A.A. Mohamad. Energy storage systems: a review. *Energy Storage and Saving*, 1(3):166–216, 2022.
- [20] M. Urbain, S. Rael, B. Davat, and P. Desprez. Energetical modelling of lithium-ion battery discharge and relaxation. In *2008 IEEE Power Electronics Specialists Conference*, pages 3628–3634, 2008.
- [21] Liu Xiubin, Li Yue, Wang Nantian, Zhuo Qingqi, and Li Tingpeng. The diffusion polarization model of lithium-ion battery relaxation effect. In *2015 12th IEEE International Conference on Electronic Measurement & Instruments (ICEMI)*, volume 01, pages 131–135, 2015.
- [22] R. Rao, S. Vrudhula, and D.N. Rakhmatov. Battery modeling for energy aware system design. *Computer*, 36(12):77–87, 2003.
- [23] Kaiyuan Li and King Jet Tseng. An equivalent circuit model for state of energy estimation of lithium-ion battery. In *2016 IEEE Applied Power Electronics Conference and Exposition (APEC)*, pages 3422–3430, 2016.
- [24] Shuai Ma, Modi Jiang, Peng Tao, Chengyi Song, Jianbo Wu, Jun Wang, Tao Deng, and Wen Shang. Temperature effect and thermal impact in lithium-ion batteries: A review. *Progress in Natural Science: Materials International*, 28(6):653–666, 2018.
- [25] Zhuo Yang, Devendra Patil, and Babak Fahimi. Electrothermal behavior of lithium-ion batteries with different levels of power fade. In *2017 IEEE Transportation Electrification Conference and Expo (ITEC)*, pages 317–322, 2017.
- [26] Pradeep Lall, Ved Soni, Guneet Sethi, and Kok Yiang. SOH modelling of Li-ion coin cells subjected to varying C-rates, depths of charge, operating temperatures and custom charge profiles. In *2021 20th IEEE Intersociety Conference on Thermal and Thermomechanical Phenomena in Electronic Systems (iTherm)*, pages 634–643, 2021.
- [27] Bharat Balagopal, Cong Sheng Huang, and Mo-Yuen Chow. Effect of calendar ageing on sei growth and its impact on electrical circuit model parameters in lithium ion batteries. In *2018 IEEE International Conference on Industrial Electronics for Sustainable Energy Systems (IESES)*, pages 32–37, 2018.
- [28] Vinko Lešić, Anita Martinčević, and Mario Vašak. Modular energy cost optimization for buildings with integrated microgrid. *Applied Energy*, 197:14 – 28, 2017.



- [29] S. Ioannou, K. Dalamagkidis, E. K. Stefanakos, K. P. Valavanis, and P. H. Wiley. Runtime, capacity and discharge current relationship for lead acid and lithium batteries. In *2016 24th Mediterranean Conference on Control and Automation (MED)*, pages 46–53, 2016.
- [30] J. Manwell and J. Mcgowan. Extension of the kinetic battery model for wind/hybrid power system. In *Proc. 5th. Eur. Wind Energy Assoc. Conf.*, pages 1182–1187, 1994.
- [31] Yizhao Gao, Xi Zhang, Bangjun Guo, Chong Zhu, Jochen Wiedemann, Lin Wang, and Jianhua Cao. Health-aware multiobjective optimal charging strategy with coupled electrochemical-thermal-aging model for lithium-ion battery. *IEEE Transactions on Industrial Informatics*, 16(5):3417–3429, 2020.
- [32] Min Chen and G.A. Rincon-Mora. Accurate electrical battery model capable of predicting runtime and I-V performance. *IEEE Transactions on Energy Conversion*, 21(2):504–511, 2006.
- [33] V.H. Johnson. Battery performance models in advisor. *Journal of Power Sources*, 110(2):321–329, 2002.
- [34] Guangming Zhao and Yifan Wang. An online model identification for state of charge estimation of lithium-ion batteries using extended kalman filter. In *2020 IEEE 3rd International Conference on Renewable Energy and Power Engineering (REPE)*, pages 34–38, 2020.
- [35] Qian Zheng, Junjie Yang, Qinyang Luo, and Kexin Shi. Estimation of state of charge of lithium battery based on BCRLS-UKF algorithm. In *2021 IEEE International Conference on Computer Science, Electronic Information Engineering and Intelligent Control Technology (CEI)*, pages 22–26, 2021.
- [36] Prashant Shrivastava, Tey Kok Soon, Mohd Yamani Idna Bin Idris, Saad Mekhilef, and Syed Bahari Ramadan Syed Adnan. Combined state of charge and state of energy estimation of lithium-ion battery using dual forgetting factor-based adaptive extended kalman filter for electric vehicle applications. *IEEE Transactions on Vehicular Technology*, 70(2):1200–1215, 2021.
- [37] Kaiyuan Li, Feng Wei, King Jet Tseng, and Boon-Hee Soong. A practical lithium-ion battery model for state of energy and voltage responses prediction incorporating temperature and ageing effects. *IEEE Transactions on Industrial Electronics*, pages 6696–6708, 2018.
- [38] Ran Zhang and Zhengqiang Pan. Model identification of lithium-ion batteries considering current-rate effects on battery impedance. In *2019 4th International Conference on Power and Renewable Energy (ICPRE)*, pages 305–309, 2019.

- [39]Radoslav Cipin, Marek Toman, Petr Prochazka, and Ivo Pazdera. Identification of Li-ion battery model parameters. In *2019 International Conference on Electrical Drives & Power Electronics (EDPE)*, pages 225–229, 2019.
- [40]Imen Jarraya, Jihen Loukil, Ferdaous Masmoudi, Mohamed Hedi Chabchoub, and Hamedh Trabelsi. Modeling and parameters estimation for lithium-ion cells in electric drive vehicle. In *2018 15th International Multi-Conference on Systems, Signals & Devices (SSD)*, pages 1128–1132, 2018.
- [41]Zhaohui Cen, Pierre Kubiak, and Ilias Belharouak. Online parameter estimation/tracking for lithium-ion battery rc model. In *2016 International Renewable and Sustainable Energy Conference (IRSEC)*, pages 936–940, 2016.
- [42]Fereshteh Poloei, Amirhosein Akbari, and Yan-Fei Liu. A moving window least mean square approach to state of charge estimation for lithium ion batteries. In *2019 1st Global Power, Energy and Communication Conference (GPECOM)*, pages 398–402, 2019.
- [43]Rui Li, Zican Wang, Jialing Yu, Yu Lei, Yingchao Zhang, and Junqiang He. Dynamic parameter identification of mathematical model of lithium-ion battery based on least square method. In *2018 IEEE International Power Electronics and Application Conference and Exposition (PEAC)*, pages 1–5, 2018.
- [44]Farshid Naseri, Erik Schaltz, Daniel-Ioan Stroe, Alejandro Gismoro, and Ebrahim Farjah. An enhanced equivalent circuit model with real-time parameter identification for battery state-of-charge estimation. *IEEE Transactions on Industrial Electronics*, 69(4):3743–3751, 2022.
- [45]Danko Marušić and Mario Vašak. Efficient method of identifying a Li-ion battery model for an electric vehicle. In *2022 IEEE 20th International Power Electronics and Motion Control Conference (PEMC)*, pages 421–426, 2022.
- [46]Asadullah Khalid, Alexander Stevenson, and Arif I. Sarwat. Overview of technical specifications for grid-connected microgrid battery energy storage systems. *IEEE Access*, 9:163554–163593, 2021.
- [47]T. Pavlović, T. Bjažić, and Ž. Ban. Simplified averaged models of DC-DC power converters suitable for controller design and microgrid simulation. *IEEE Transactions on Power Electronics*, 28(7):3266–3275, 2013.
- [48]D. Maksimovic, A. M. Stankovic, V. J. Thottuvelil, and G. C. Verghese. Modeling and simulation of power electronic converters. *Proceedings of the IEEE*, 89(6):898–912, 2001.

- [49] R.W. Erickson and D. Maksimović. *Fundamentals of Power Electronics*. Kluwer Academic Publishers, 2 edition, 2003.
- [50] L. Dixon. *Average Current-Mode Control of Switching Power Supplies — Unitrode Application Note*. Texas Instruments, Inc., 1997.
- [51] P. R. K. Chetty. Cieca: Application to current programmed switching DC-DC converters. *IEEE Transactions on Aerospace and Electronic Systems*, AES-18(5):538–544, 1982.
- [52] J. Li and F. C. Lee. New modeling approach and equivalent circuit representation for current-mode control. *IEEE Transactions on Power Electronics*, 25(5):1218–1230, 2010.
- [53] M. Gulin, M. Vašak, and M. Baotić. Analysis of microgrid power flow optimization with consideration of residual storages state. *2015 European Control Conference (ECC)*, pages 3126–3131, 2015.
- [54] M. Gulin, M. Vašak, and T. Pavlović. Dynamical behaviour analysis of a DC microgrid in distributed and centralized voltage control configurations. *2014 IEEE 23rd International Symposium on Industrial Electronics (ISIE)*, pages 2365–2370, 2014.
- [55] M. Car, M. Vašak, and V. Lešić. Control of a buck-boost DC-DC power converter for microgrid energy storage. *2017 19th International Conference on Electrical Drives and Power Electronics (EDPE)*, pages 122–127, 2017.
- [56] Changfu Zou, Chris Manzie, and Dragan Nešić. Model predictive control for lithium-ion battery optimal charging. *IEEE/ASME Transactions on Mechatronics*, 23(2):947–957, 2018.
- [57] Yizhao Gao, Xi Zhang, Qiyu Cheng, Bangjun Guo, and Jun Yang. Classification and review of the charging strategies for commercial lithium-ion batteries. *IEEE Access*, 7:43511–43524, 2019.
- [58] Quan Ouyang, Jian Chen, Jian Zheng, and Huazhen Fang. Optimal multiobjective charging for lithium-ion battery packs: A hierarchical control approach. *IEEE Transactions on Industrial Informatics*, 14(9):4243–4253, 2018.
- [59] Ning Tian, Huazhen Fang, and Yebin Wang. Real-time optimal lithium-ion battery charging based on explicit model predictive control. *IEEE Transactions on Industrial Informatics*, 17(2):1318–1330, 2021.
- [60] Mario Vašak and Goran Kujundžić. A battery management system for efficient adherence to energy exchange commands under longevity constraints. *IEEE Transactions on Industry Applications*, 54(4):3019–3033, 2018.

- [61] M. Jelavić, V. Petrović, and N. Perić. Individual pitch control of wind turbine based on loads estimation. *2008 34th Annual Conference of IEEE Industrial Electronics*, pages 228–234, 2008.
- [62] Mate Jelavić. *Wind turbine control for structural dynamic loads reduction*. PhD thesis, University of Zagreb, Faculty of Electrical Engineering and Computing, 2009.
- [63] V. Lešić, M. Vašak, N. Perić, G. Joksimović, and T. Wolbank. Fault-tolerant control of a wind turbine with a squirrel-cage induction generator and stator inter-turn faults. *Proceedings of the 12th International Workshop on Advanced Motion Control*, 2012.
- [64] V. Lešić, M. Vašak, G. Stojčić, and T. Wolbank. Fault-tolerant control of wound rotor synchronous generator in wind turbines. *International Conference on Electrical Machines, ICEM, Berlin, Germany*, pages 1752–1758, 2014.
- [65] T. Lončarek, V. Lešić, and M. Vašak. Increasing accuracy of kalman filter-based sensorless control of wind turbine PM synchronous generator. *IEEE International Conference on Industrial Technology, ICIT 2015 Sevilla*, pages 745–750, 2015.
- [66] B. K. Dey, I. Khan, N. Mandal, and A. Bhattacharjee. Mathematical modelling and characteristic analysis of solar PV cell. *2016 IEEE 7th Annual Information Technology, Electronics and Mobile Communication Conference (IEMCON)*, pages 1–5, 2016.
- [67] M. Alqarni and M. K. Darwish. Maximum power point tracking for photovoltaic system: Modified perturb and observe algorithm. *2012 47th International Universities Power Engineering Conference (UPEC)*, pages 1–4, 2012.
- [68] Radhia Garraoui, Mouna Ben Hamed, and Lassaad Sbita. Comparison of MPPT algorithms for DC-DC boost converters based PV systems using robust control technique and artificial intelligence algorithm. In *2015 IEEE 12th International Multi-Conference on Systems, Signals & Devices (SSD15)*, pages 1–6, 2015.
- [69] Mouna Ben Smida and Anis Sakly. Genetic based algorithm for maximum power point tracking (MPPT) for grid connected PV systems operating under partial shaded conditions. In *2015 7th International Conference on Modelling, Identification and Control (ICMIC)*, pages 1–6, 2015.
- [70] M. Gulin, M. Vašak, and T. Pavlović. Model identification of a photovoltaic system for a DC microgrid simulation. In *2014 16th International Power Electronics and Motion Control Conference and Exposition*, pages 413–418, 2014.
- [71] J. R. Massing, M. Stefanello, H. A. Grundling, and H. Pinheiro. Adaptive current control for grid-connected converters with LCL filter. *IEEE Transactions on Industrial Electronics*, pages 4681–4693, 2012.

- [72]B. Arif, L. Tarisciotti, P. Zanchetta, J. C. Clare, and M. Degano. Grid parameter estimation using model predictive direct power control. *IEEE Transactions on Industry Applications*, pages 4614–4622, 2015.
- [73]L. Jessen and F. W. Fuchs. Modeling of inverter output impedance for stability analysis in combination with measured grid impedances. *2015 IEEE 6th International Symposium on Power Electronics for Distributed Generation Systems (PEDG)*, pages 1–7, 2015.
- [74]M. Liserre, R. Teodorescu, and F. Blaabjerg. Stability of photovoltaic and wind turbine grid-connected inverters for a large set of grid impedance values. *IEEE Transactions on Power Electronics*, pages 263–272, 2006.
- [75]D. Pérez-Estévez, J. Doval-Gandoy, A. G. Yepes, Ó. López, and F. Baneira. Enhanced resonant current controller for grid-connected converters with LCL filter. *IEEE Transactions on Power Electronics*, pages 3765–3778, 2018.
- [76]S. Bosch, J. Staiger, and H. Steinhart. Predictive current control for an active power filter with LCL-filter. *IEEE Transactions on Industrial Electronics*, pages 4943–4952, 2018.
- [77]D. Pan, X. Ruan, C. Bao, W. Li, and X. Wang. Optimized controller design for LCL-type grid-connected inverter to achieve high robustness against grid-impedance variation. *IEEE Transactions on Industrial Electronics*, pages 1537–1547, 2015.
- [78]D. Choi and K. Lee. Dynamic performance improvement of AC/DC converter using model predictive direct power control with finite control set. *IEEE Transactions on Industrial Electronics*, 62(2):757–767, Feb 2015.
- [79]J. A. Rohten, J. R. Espinoza, J. A. Muñoz, M. A. Pérez, P. E. Melin, J. J. Silva, E. E. Espinosa, and M. E. Rivera. Model predictive control for power converters in a distorted three-phase power supply. *IEEE Transactions on Industrial Electronics*, 63(9):5838–5848, Sep. 2016.
- [80]M. Merai, M. W. Naouar, and I. Slama-Belkhodja. An improved DC-link voltage control strategy for grid connected converters. *IEEE Transactions on Power Electronics*, pages 3575–3582, 2018.
- [81]Dong-Choon Lee, G-Myoung Lee, and Ki-Do Lee. DC-bus voltage control of three-phase AC/DC PWM converters using feedback linearization. *IEEE Transactions on Industry Applications*, pages 826–833, 2000.
- [82]M. Jamma, M. Akherraz, and M. Barar. Anfis based DC-link voltage control of PWM rectifier-inverter system with enhanced dynamic performance. In *IECON*

- 2018 - 44th Annual Conference of the IEEE Industrial Electronics Society, pages 2219–2224, Oct 2018.
- [83] Y. Saidi, A. Mezouar, Y. Miloud, and M. A. Benmahdjoub. A robust control strategy for three phase voltage source PWM rectifier connected to a PMSG wind energy conversion system. In *2018 International Conference on Electrical Sciences and Technologies in Maghreb (CISTEM)*, pages 1–6, Oct 2018.
- [84] J. Lamterkati, M. Khaffalah, L. Ouboubker, and A. El afia. Fuzzy logic based improved direct power control of three-phase PWM rectifier. In *2016 International Conference on Electrical and Information Technologies (ICEIT)*, pages 125–130, May 2016.
- [85] S. Vazquez, J. I. Leon, L. G. Franquelo, J. Rodriguez, H. A. Young, A. Marquez, and P. Zanchetta. Model predictive control: A review of its applications in power electronics. *IEEE Industrial Electronics Magazine*, 8(1):16–31, March 2014.
- [86] L. Tarisciotti, G. Lo Calzo, A. Gaeta, P. Zanchetta, F. Valencia, and D. Sáez. A distributed model predictive control strategy for back-to-back converters. *IEEE Transactions on Industrial Electronics*, pages 5867–5878, 2016.
- [87] J. Liu, S. Vazquez, L. Wu, A. Marquez, H. Gao, and L. G. Franquelo. Extended state observer-based sliding-mode control for three-phase power converters. *IEEE Transactions on Industrial Electronics*, 64(1):22–31, Jan 2017.
- [88] W. Luo, T. Zhao, X. Li, Z. Wang, and L. Wu. Adaptive super-twisting sliding mode control of three-phase power rectifiers in active front end applications. *IET Control Theory Applications*, 13(10):1483–1490, 2019.
- [89] Y. Huang, X. Yuan, J. Hu, and P. Zhou. Modeling of VSC connected to weak grid for stability analysis of DC-link voltage control. *IEEE Journal of Emerging and Selected Topics in Power Electronics*, pages 1193–1204, 2015.
- [90] M. Davari and Y. A. I. Mohamed. Dynamics and robust control of a grid-connected VSC in multiterminal DC grids considering the instantaneous power of DC- and AC-side filters and DC grid uncertainty. *IEEE Transactions on Power Electronics*, pages 1942–1958, 2016.
- [91] J.G.Truxal. *Automatic Feedback Control System Synthesis*. McGraw Hill, 1955.
- [92] M. Car, V. Lešić, and M. Vašak. DC link voltage control of back-to-back converter robust to grid conditions. In *2017 19th International Conference on Electrical Drives and Power Electronics (EDPE)*, pages 147–152, 2017.

- [93] D. G. Holmes, T. A. Lipo, B. P. McGrath, and W. Y. Kong. Optimized design of stationary frame three phase AC current regulators. *IEEE Transactions on Power Electronics*, pages 2417–2426, 2009.
- [94] J. W. Umland and M. Safiuddin. Magnitude and symmetric optimum criterion for the design of linear control systems: what is it and how does it compare with the others? *IEEE Transactions on Industry Applications*, 26(3):489–497, 1990.
- [95] W. R. Evans. Control system synthesis by root locus method. *Transactions of the American Institute of Electrical Engineers*, 69(1):66–69, 1950.
- [96] R. Teodorescu, M. Liserre, and P. Rodriguez. *Grid Converters for Photovoltaic and Wind Power Systems*. John Wiley & Sons, Ltd., 2011.
- [97] F. Liu, Y. Zhou, S. Duan, J. Yin, B. Liu, and F. Liu. Parameter design of a two-current-loop controller used in a grid-connected inverter system with LCL filter. *IEEE Transactions on Industrial Electronics*, pages 4483–4491, 2009.
- [98] T. Midtsund, J. A. Suul, and T. Undeland. Evaluation of current controller performance and stability for voltage source converters connected to a weak grid. In *The 2nd International Symposium on Power Electronics for Distributed Generation Systems*, pages 382–388, June 2010.
- [99] Trung Do Thanh, S. Schostan, K. D. Dettmann, and D. Schulz. Nonsinusoidal power caused by measurements of grid impedances at unbalanced grid voltages. *2008 International School on Nonsinusoidal Currents and Compensation*, pages 1–7, 2008.
- [100] V. Kaura and V. Blasko. Operation of a phase locked loop system under distorted utility conditions. *IEEE Transactions on Industry Applications*, pages 58–63, 1997.
- [101] M. Ramezani, S. Golestan, S. Li, and J. M. Guerrero. A simple approach to enhance the performance of complex-coefficient filter-based PLL in grid-connected applications. *IEEE Transactions on Industrial Electronics*, pages 5081–5085, 2018.
- [102] S. Golestan, J. M. Guerrero, and J. C. Vasquez. Three-phase PLLs: A review of recent advances. *IEEE Transactions on Power Electronics*, pages 1894–1907, 2017.
- [103] Praful V. Nandankar, Prashant P. Bedekar, and Prashantkumar V. Dhawas. Efficient DC-DC converter using variable switching frequency digital controller. In *2020 5th IEEE International Conference on Recent Advances and Innovations in Engineering (ICRAIE)*, pages 1–6, 2020.
- [104] Ke Jia, Bohan Liu, Mineze Iyogun, and Tianshu Bi. Smart control for battery energy storage system in a community grid. In *2014 International Conference on Power System Technology*, pages 3243–3248, 2014.

- 
- [105] Gusti Arif Hanifah Pawitan and Jung-Su Kim. MPC-based power management of renewable generation using multi-ESS guaranteeing SoC constraints and balancing. *IEEE Access*, pages 12897–12906, 2020.
- [106] Shuang Zhao, Xingchen Zhao, Chris Farnell, H. Alan Mantooth, Janvier Umuhzoza, and Yuzhi Zhang. A daily optimization method for a PV-battery microgrid considering the battery lifetime and time-of-use pricing. In *2019 IEEE Applied Power Electronics Conference and Exposition (APEC)*, pages 3243–3250, 2019.
- [107] Rama K. Bonthu, Ricardo P. Aguilera, Ha Pham, Manh Duong Phung, and Quang P. Ha. Energy cost optimization in microgrids using model predictive control and mixed integer linear programming. In *2019 IEEE International Conference on Industrial Technology (ICIT)*, pages 1113–1118, 2019.
- [108] Marko Gulin, Mario Vašak, and Mato Baotić. Analysis of microgrid power flow optimization with consideration of residual storages state. In *2015 European Control Conference (ECC)*, pages 3126–3131, 2015.





## CURRICULUM VITAE

---

**Mateja Car** was born in Zagreb in 1992. She graduated from University of Zagreb Faculty of Electrical Engineering and Computing (UNIZG-FER) in 2016. in the field of electrical engineering, Electrical Power Engineering branch, as 10% of most successful students in generation ("Cum Laude" title). She was awarded the excellence scholarship from the University of Zagreb in academic years 2014/2015 and 2015/2016. During her studies she combines fields of two branches: Electrical Power Engineering and Control Engineering and Automation and focuses on control of renewable energy sources. During bachelor's studies she deals mainly with wind energy and wind turbine control while during her masters studies she focuses on power converters control. She is employed in the Department of Control and Computer Engineering, working as a member of the Laboratory for Renewable Energy Systems (LARES). During her work at FER she has participated in 2 projects: "POC-DAWN – *Proof of Concept for Damping Generator Vibrations and Large Wind Turbine Noise by Advanced Power Converter Control*" focused on application of estimation methods from control theory field on power converters in order to reduce torque oscillations and vibrations in wind turbine generators and on a project in cooperation with a foreign company United Technologies Research Centre Ireland Ltd. From January 2021 she is working on the project "*Distribuirano upravljanje za dinamičko gospodarenje energijom u složenim sustavima* - DECIDE" Her research interests include estimation methods and model predictive control with applications in renewable energy systems, and power converters within microgrids with aim to increase energy efficiency of all elements and achieve smart battery management and she is author of one journal paper and 4 research articles published on an international conference.



## LIST OF PUBLICATIONS

---

### Journal papers

- 1.Car, Mateja; Lešić, Vinko; Vašak, Mario. Cascaded control of back-to-back converter DC link voltage robust to grid parameters variation. *IEEE transactions on industrial electronics*, 2021, doi:10.1109/TIE.2020.2972467

### Conference papers

- 1.Hajihosseini, Mojtaba; Car, Mateja; Zeeshan, Aleem; Lešić, Vinko. Charging control of a Vanadium redox flow battery integrated with solar PV plant. *ISIE 2023 - 32nd International Symposium on Industrial Electronics*, 2023
- 2.Car, Mateja; Vašak, Mario; Hajihosseini, Mojtaba; Lešić, Vinko. Nonlinear model predictive control of a microgrid with a variable efficiency battery storage system. *IECON 2022 – 48th Annual Conference of the IEEE Industrial Electronics Society*, 2022
- 3.Car, Mateja; Lešić, Vinko; Vašak, Mario. DC link voltage control of back-to-back converter robust to grid conditions. *Proceedings of the 19th International Conference on Electrical Drives and Power Electronics, EDPE 2017*, 2017
- 4.Car, Mateja; Vašak, Mario; Lešić, Vinko. Control of a buck-boost DC-DC power converter for microgrid energy storage. *Proceedings of the 19th International Conference on Electrical Drives and Power Electronics, EDPE 2017*, 2017



**Mateja Car** rođena je u Zagrebu 1992. godine. Završila je diplomski studij na Sveučilištu u Zagrebu Fakultetu elektrotehnike i računarstva (UNIZG-FER) 2016. godine u polju elektrotehnike, modul Elektroenergetika, među 10% najuspješnijih studenata u generaciji (Cum Laude). Dobitnica je stipendije za izvrsnost Sveučilišta u Zagrebu za akademske godine 2014/2015 i 2015/2016. Tijekom studija kombinira teme dvaju modula: Elektroenergetika i Automatika te se usmjerava na upravljanje obnovljivim izvorima energije. Tijekom preddiplomskog studija uže se bavi energijom vjetra i upravljanjem vjetroagregatima dok se na diplomskom studiju fokusira na upravljanje učinkim pretvaračima u mikromreži za povezivanje obnovljivih izvora energije s elektroenergetskom mrežom. Nakon završenog studija, zapošljava se na Zavodu za automatiku i računalno inženjerstvo UNIZG-FER-a u sklopu Laboratorija za sustave obnovljivih izvora energije (LARES). Tijekom rada na FER-u sudjelovala je na projektu "POC-DAWN – *Proof of Concept for Damping Generator Vibrations and Large Wind Turbine Noise by Advanced Power Converter Control*" koji se fokusira na primjenu estimacijskih metoda iz područja teorije upravljanja s ciljem smanjenja vibracija u generatoru te na gospodarskom projektu s inozemnim ulagačem United Technologies Research Centre Ireland Ltd. Od siječnja 2021. radi na projektu "*Distribuirano upravljanje za dinamičko gospodarenje energijom u složenim sustavima* - DECIDE". Istraživački interesi usmjereni su na estimacijske metode te modelsko prediktivno upravljanje s primjenom u obnovljivim izvorima i frekvencijskim pretvaračima unutar mikromreže s ciljem poboljšanja njihovog rada te naprednog gospodarenja baterijama te je autor je jednog časopisnog i 4 konferencijska rada iz navedenih područja.